

ABSTRACT

WANG, YIFAN. Snapshot Retinal Imaging Mueller Matrix Polarimeter. (Under the direction of Michael. W. Kudenov).

The polarization properties of materials, such as retardance, diattenuation and depolarization, are important indicators of physical and chemical characteristics. These properties can be decomposed from corresponding Mueller matrix (MM). In clinical practice of ophthalmometry, imaging polarimetry helps to identify retinal diseases such as glaucoma and age related macular degeneration (AMD) in early stages by acquiring and investigating the 2D retinal MM. Currently, the prevailing technique for retinal MM acquisition is scanning laser polarimetry (SLP), in which a laser beam with pre-defined polarization states scans through a certain region of interest (ROI) on retina, the back-scattered light after interaction with retina is collected and analyzed to generate the MM for every point in the scanning area. SLP has major advantages such as high-quality image output, comfortable patient experience with no pupil dilation needed, *etc.* The temporal scanning nature of the technique, however, limits its temporal resolution and system robustness, increases the complexity of post-processing.

The aim of this research is to develop an imaging polarimeter that can obtain full MM information from a 2D area on human retina with a single snapshot. With two pairs of polarization gratings (along with other polarizing elements), the system modulates polarization information of the 2D scene onto different spatial frequency channels and reconstructs 2D MM from the demodulated polarization information with linear algebra operations. Optical design and opto-mechanical design for the device were carried out, and the prototype was assembled in lab, a control program with graphical user interface (GUI) was also created. Lab tests with a model eye have shown that, as a full imaging MM polarimeter, the device's performance is satisfactory with an average error about 0.05 in the measurements of 2D MM from several different polarizing

element samples. Preliminary clinical tests were also conducted with two subjects in the medical campus of the University of Southern California (USC). The results show great potential for 2D MM reconstruction from real retina with the device.

© Copyright 2018 by Yifan Wang

All Rights Reserved

Snapshot Retinal Imaging Mueller Matrix Polarimeter

by
Yifan Wang

A dissertation submitted to the Graduate Faculty of
North Carolina State University
in partial fulfillment of the
requirements for the degree of
Doctor of Philosophy

Electrical Engineering

Raleigh, North Carolina

2018

APPROVED BY:

Dr. Michael Kudenov
Chair of Advisory Committee

Dr. John Muth

Dr. Michael Escuti

Dr. Kara Peters

DEDICATION

I dedicate this work to my parents and my wife, for their constant support throughout my academic journey.

BIOGRAPHY

Yifan Wang was born in Shijiazhuang, China on Jan 27th, 1989. He went to the Precision Instrument and Optoelectronics Engineering department of Tianjin University in 2007 and received a Bachelor of Engineering degree in July 2011. He came to the US to enter the Electrical Engineering Master's program in North Carolina State University, under the direction of Dr. John F. Muth. After the completion of his master's program in August 2014, he was accepted into Electrical Engineering Ph.D. program and started his research about retinal imaging polarimetry under the direction of Dr. Michael W. Kudenov. After finishing his Ph.D. studies, Yifan Wang plans to apply the knowledge and skills he has learned from academia in the optical engineering industry.

ACKNOWLEDGMENTS

I would like to express my gratitude to my advisor, Dr. Kudenov, for his guidance and help throughout the whole project. I would also like to thank Dr. Muth, Dr. Escuti, Dr. Peters and Dr. Pankow for serving as advisory committee members. I appreciate the help from Dr. Kashani and Kyle Green during the clinical tests of the device in the University of Southern California.

During my past 4 years in the optical sensing lab, I had the luck to work together with many brilliant people who were also pursuing their academic degrees, including Ali Altaqui, Brandon Ballance, Brett Pantalone, Bryan Maione, David Luo, Ethan Woodard, Eddie Youngs, Grant Scarboro, Hoang Nguyen, Kun Cao, Mariano Lowenstern, Nathan Sanders, Ruonan Yang, Subharup Gupta Roy and Zhejun Wu. The talks and discussions with them brought me much inspiration for my research. I would like to express my gratitude to them and hope them the best of luck in their future works.

I would like to thank my families and friends, without their financial and mental support it would be impossible for me to complete my graduate study.

TABLE OF CONTENTS

LIST OF TABLES.....	vii
LIST OF FIGURES.....	viii
Chapter 1 Introduction.....	1
References.....	4
Chapter 2 Snapshot Channeled Polarimeter.....	6
2.1 Polarization of light and its representation.....	6
2.1.1 Jones vector and Jones matrix.....	7
2.1.2 Stokes vector and Mueller matrix.....	7
2.2 Snapshot channeled Stokes polarimeter.....	9
2.2.1 Snapshot channeled Stokes polarimeters with spectral modulation.....	10
2.2.2 Snapshot channeled Stokes polarimeters with spatial modulation.....	12
2.3 Snapshot channeled Mueller matrix polarimeters.....	14
2.3.1 Snapshot channeled Mueller matrix polarimeters with spec-spec modulation.....	15
2.3.2 Snapshot channeled Mueller matrix polarimeters with spat-spat modulation.....	17
2.3.3 Snapshot channeled Mueller matrix polarimeters with spec-spat modulation.....	19
2.4 Polarimeters based on polarization gratings.....	20
2.5 Snapshot retinal imaging Mueller matrix polarimeter.....	21
2.6 Generalized channeled polarimetry.....	24
References.....	25
Chapter 3 System Design and Assembly.....	29
3.1 Optical designs.....	29
3.1.1 Optical design of SRIMMP.....	29
3.1.2 Optical design of model eye.....	40
3.2 Opto-mechanical designs.....	41
3.2.1 Opto-mechanical design of SRIMMP.....	41
3.2.2 Opto-mechanical design of model eye.....	45
3.3 Choice of illumination source.....	46
3.4 Choice of polarization gratings.....	48
3.5 Assembly of the SRIMMP device.....	53
References.....	56
Chapter 4 System Calibration and Mueller Matrix Reconstruction.....	57
4.1 System calibration.....	57
4.2 2D Mueller matrix reconstruction.....	64
4.2.1 2D input Stokes parameters from the “empty polarimeter” frame.....	66
4.2.2 2D input Stokes parameters from the Stokes parameter fitting program.....	67
4.3 Simulation model of system calibration and 2D Mueller matrix reconstruction.....	71
References.....	76

Chapter 5 Experimental Results.....	77
References.....	86
Chapter 6 Preliminary Clinical Tests.....	87
6.1 The control program of SRIMMP.....	87
6.2 The first clinical test.....	90
6.3 The second clinical test.....	96
References.....	102
Chapter 7 Conclusion and Future Works.....	104
7.1 Conclusion.....	104
7.2 Suggestions for future works.....	105
APPENDICES.....	106
Appendix A – Derivation of Stokes parameters.....	107
Appendix B – Matlab simulation model of calibration and Mueller matrix reconstruction...	109
Appendix C – Matlab code used to generate correction matrices from calibration data.....	120

LIST OF TABLES

Table 2-1	Fourier domain channel contents of the snapshot Mueller matrix spectropolarimeter proposed by Hagen <i>et al.</i>	16
Table 2-2	Comparison of system characteristics among typical Mueller matrix polarimeters...	22
Table 3-1	Parts list of the optics and opto-mechanical components used in the SRIMMP design, including the part number (PN), the part name as well as their associated model provided by the vendor, and the required quantities.....	44
Table 3-2	Parts list of the optics and opto-mechanical components used in the model eye design, including the part number (PN), the part name as well as their associated model provided by the vendor, and the required quantities.....	46

LIST OF FIGURES

Figure 2-1	Schematic of the spectroscopic polarimeter as reported by Oka and Kato.....	10
Figure 2-2	Improved FTSP system model used to investigate the influence of dichroism on the reconstruction results, developed by Kudenov <i>et al.</i>	12
Figure 2-3	Schematic of the polarimetric analyzer with spatial channel modulation as described by Oka and Kaneko.....	13
Figure 2-4	Power spectrum of the intensity pattern captured in Oka and Kaneko's channeled spatial polarimeter experiment.....	14
Figure 2-5	Layout of the snapshot Mueller matrix spectropolarimeter proposed by Hagen <i>et al.</i>	15
Figure 2-6	Layout of the snapshot imaging Mueller matrix spectropolarimeter (SIMMP) proposed by Kudenov <i>et al.</i>	17
Figure 2-7	Fourier domain of intensity fringes recorded by the SIMMP.....	18
Figure 2-8	Sketch of the hyperspectroscopic channeled Mueller matrix polarimeter.....	19
Figure 2-9	Schematic of the snapshot imaging Mueller matrix polarimeter using pupil-plane interferometers. Each pupil-plane interferometer consists of two PGs in series. As described by Kudenov <i>et al.</i>	21
Figure 2-10	Schematic of the snapshot imaging Mueller matrix polarimeter using image-plane Interferometers by Kudenov <i>et al.</i>	23
Figure 3-1	Sketches of fundus camera designs with a) external and b) internal illumination...	30
Figure 3-2	Paraxial illumination pathway model with internal illumination in Zemax.....	31
Figure 3-3	Light pattern on a) cornea and b) the first surface of objective lens in the paraxial internal illumination design verification model.....	32
Figure 3-4	Light pattern on retina with internal illumination, central blockage observed.....	32
Figure 3-5	Simplified model with external illumination in Zemax used to verify the viability of SRIMMP optical design.....	33
Figure 3-6	Light pattern on a) cornea and b) eye fundus in the paraxial external illumination verification model. As can be seen, the annulus image projects onto the cornea and the aperture pattern defined on the PSG plane is imaged onto the retina.....	33
Figure 3-7	Schematic of the SRIMMP optical design with external illumination. BS is a cubicle beamsplitter, FPA stands for focal plane array used to capture retinal images.....	34
Figure 3-8	a) Layout of the imaging pathway in Zemax sequential mode; b) lens prescription of the imaging pathway.....	35
Figure 3-9	MTF curves of the imaging pathway with 4 mm pupil size.....	36
Figure 3-10	a) Layout of illumination pathway design from the PSG to the eye fundus, all the optical components are off-the-shelf, b) Zemax lens prescription of the illumination pathway design from the PSG plane to the eye fundus.....	37

Figure 3-11 MTF curves of the illumination pathway from the PSG plane to the eye fundus....	38
Figure 3-12 Layout of the SRIMMP optical design in non-sequential mode of Zemax.....	39
Figure 3-13 Light distribution on the detectors at a) FPA; b) fundus; and c) cornea resulted from the ray-tracing simulation.....	39
Figure 3-14 a) Layout of the model eye design in Zemax sequential mode; b) the corresponding lens prescription.....	40
Figure 3-15 FFT MTF curves of the Model eye design in Zemax.....	41
Figure 3-16 Opto-mechanical CAD design of the beamsplitter case as part of the 60-mm cage system.....	42
Figure 3-17 Left: 3D printed prototype of the beamsplitter case; right: the aluminum beamsplitter case.....	43
Figure 3-18 Position of the slotted lens tube containing the PSG in the SRIMPP opto-mechanical design.....	43
Figure 3-19 The opto-mechanical CAD design model of the SRIMMP system. The details of the labeled parts are shown in Table 4-1.....	45
Figure 3-20 The 3D model of the model eye assembly in Autodesk Inventor.....	45
Figure 3-21 The initial SRIMMP experimental setup on an optical table for radiometry tests. The model eye would be replaced by a photodetector during the tests.....	48
Figure 3-22 All the ideal channels in the Fourier domain of a channeled image obtained from the SRIMM with x/y/x/y arrangement. The ratio between the PG periods of the PSG and the PSA is 4:1. f_x and f_y axes in Fourier domain correspond to x and y axes in spatial domain.....	49
Figure 3-23 The initial system setup of SRIMMP on the translational stage cannibalized from an old Kowa FX50R fundus camera. The illumination pathway is labeled by the yellow curly bracket.....	53
Figure 3-24 The system setup of SRIMMP after illumination pathway modification. Note that the PSG is out of the lens tube.....	54
Figure 3-25 The updated fundus camera hardware with the motor-driven rotational wheel and corresponding motor, sensor, and circuits incorporated.....	55
Figure 4-1 Ideal channel distribution of the PSA in Fourier domain, ϵ and η are Fourier domain coordinates correspond to the spatial coordinates x and y, only non-conjugated channels are shown in the graph.....	59
Figure 4-2 The Fourier domain of the PSA when the two PGs and the QWP each has 10° retardance error. Channels circled are additional channeled due to the errors.....	61
Figure 4-3 The SRIMMP calibration with calibration samples used to generate known polarization states.....	61
Figure 4-4 The calibration setup for the SRIMMP.....	62

Figure 4-5	Fourier domain spatial frequency channel distribution of PSA with incident polarization states from the PSG. The relationship between channels and Stokes coefficient are as labeled.....	64
Figure 4-6	Schematic of how to form the S_{in} matrix and the S_{out} matrix from Stokes parameters obtained using reference beam technique. N is the number of pixels within the square filter window.....	65
Figure 4-7	A PSG intensity modulated frame from with an empty model eye.....	68
Figure 4-8	The 3D CAD design for the rotational plate in Solidworks.....	69
Figure 4-9	The intensity fringes on simulated reference beam images with a) linear polarization at 0° , and b) right circular polarization.....	72
Figure 4-10	The intensity fringes on simulated reference beam images with a) linear polarization at 0° , and b) right circular polarization.....	72
Figure 4-11	The demodulated 2D Stokes parameters a) S_1 , b) S_2 , and c) S_3 from the “empty polarimeter” frame generated by the simulation model.....	73
Figure 4-12	An illustration of the test sample in the simulation model. The pixels on the central cross-shaped region have Mueller matrices that are different from those of the other pixels.....	73
Figure 4-13	The reconstructed 2D Mueller matrix from the Matlab simulation model.....	74
Figure 5-1	a) Data frame from an empty polarimeter. b) The reconstructed Mueller matrix of (a).....	79
Figure 5-2	a) Data frame from a half wave plate with fast axis oriented at 155° . b) The reconstructed Mueller matrix of (a), each Mueller matrix coefficient is normalized by transmittance.	80
Figure 5-3	a) Data frame from a linear polarizer with transmission axis 100° to the horizontal direction. b) The reconstructed Mueller matrix for (a), each Mueller matrix coefficient is normalized by light transmittance.....	81
Figure 5-4	The distribution of scattered light from the center of the FOV to the periphery along a) horizontal and b) vertical directions in the SRIMMP device.....	82
Figure 5-5	The normalized 2D distribution of scattered light in the SRIMMP device.....	83
Figure 5-6	The reconstructed 2D Mueller matrix from a half wave plate sample with its fast axis oriented at 155° . Output correction matrices were applied to the measured output Stoke parameters to increase reconstruction accuracy.....	85
Figure 6-1	Sub-sections of the control system’s LabVIEW block diagram. a) Video stream separation & dark frame subtraction. b) Dark frame acquisition. c) Data frame acquisition.....	89
Figure 6-2	The graphical user interface (GUI) of the control program of SRIMMP.....	90
Figure 6-3	a) Polarization modulation frame and b) intensity modulation frame taken from the retina of subject’s left eye.....	91
Figure 6-4	The reconstructed 2D Mueller matrix of the macular region in Figure. 7-3.....	92

Figure 6-5	The reconstructed Mueller matrix of macular region in Figure. 7-3. with lower resolution and better signal-to-noise (SNR) ratio.....	92
Figure 6-6	The Fourier domain of a retinal data frame a) before and b) after the background subtraction. It can be seen from the pictures that the influence of the central burst decreases after applying our background subtraction technique.....	95
Figure 6-7	The reconstructed 2D Muller matrix of the macular region from a retinal data frame after applying our background subtraction technique. More features appeared on the Mueller matrix elements, but no bow-tie pattern was observed.....	96
Figure 6-8	A close-up view of polarization fringes on the macular region.....	97
Figure 6-9	The reconstructed 2D Mueller matrix of the macular region from a retinal data frame taken in the second clinical test. The input Stokes parameters were demodulated from an “empty polarimeter” frame with reference beam technique...	98
Figure 6-10	The reconstructed 2D Mueller matrix of the macular region from a retinal data frame taken in the second clinical test. The input Stokes parameters were created by a fitting model according to the PSG intensity modulation frame taken along with the data frame.....	98
Figure 6-11	A retinal image taken from the optic disc region of a subject’s left eye, with 565 nm green LED as illumination source.....	99
Figure 6-12	Fourier domain spatial frequency channel distribution. ϵ and η are Fourier domain coordinates correspond to the spatial coordinates x and y , only non-conjugated channels are shown in the graph.....	100
Figure 6-13	The reconstructed 2D Mueller matrix of the macular region from a retinal data image taken with 565 nm illumination in the second clinical test.....	101

Chapter 1 Introduction

Mueller matrix (MM) is a 4×4 matrix first developed by physicist Hans Mueller in 1943 [1]. It is used to describe the polarization-altering ability of objects [2]. The polarization properties decomposed from MMs are often important indicators of physical and chemical characteristics [3,4]. Imaging MM polarimetry focuses on the acquisition and interpretation of partial or full MMs from 2D scenes. It has many application scenarios in domains such as astronomy, remote sensing, biomedical imaging *etc.* [5-9].

In ophthalmometry, imaging MM polarimetry plays an important role in early diagnosis of certain retinal diseases such as glaucoma and age-related macular degeneration [10-12]. Traditional diagnosis for glaucoma is based on the observation of structural changes on eye retina by physicians with fundus photography [11]. This kind of diagnosis is not very sensitive for glaucoma at early stages, and in some circumstances not easily reproducible or reliable since it largely depends upon skills and experience of the operator/physician who performs it. Biomedical studies have demonstrated that abnormalities in the retinal nerve fiber layer (RNFL) are the earliest signs of some retinal diseases [13]. Over the years, many novel retinal detection modalities were developed with the purpose of observing these abnormalities, including confocal scanning laser ophthalmoscopy (cSLO), optical coherence tomography (OCT), and scanning laser polarimetry (SLP) [11].

While most of these methods focus on the detection of RNFL thickness loss, SLP is special since it detects RNFL birefringence loss which happens prior to thickness loss [13]. A scanning laser polarimeter sends a laser beam with pre-defined polarization states into human eye through the pupil and scans across the region of interest (ROI) on the retina. Backscattered light from the retina is collected and analyzed to reconstruct the Mueller matrices from point to point. In terms

of measuring retinal Mueller matrices, while SLP has many advantages including high spatial resolution, accurate reconstruction results and pupil-dilation-free tests, it also has some disadvantages that limit it from higher operational efficiency. For example, many currently available SLPs are incomplete polarimeters that only measure a subset of polarization parameters, which makes the measurement results susceptible to the influence of large depolarization and diattenuation [14]. Moreover, corneal birefringence compensation in these devices is a challenging task, especially for some myopic or emmetropic eyes [15]. To fully reveal the polarization properties of the retinal tissues, researchers have been working on incorporating full MM polarimetry into fundus detection. For example, Van Blokland reported a device that takes *in vivo* full MM measurement of a single retinal location [16]. Bueno has used camera-based MM imaging polarimeters to measure the polarization properties of the cornea, lens and eye [17]. Twietmeyer and Chipman have converted a Carl Zeiss GDx scanning laser partial polarimeter into a MM laser scanning polarimeter [14]. A major disadvantage of these complete polarimeters is their requirement for temporal scanning. To reconstruct full MMs, these devices need to take 16 or more measurements at each point on the retina with different incident polarization states generated by rotating elements within the devices. This makes the measurements vulnerable to unconscious eye movements [18], increases the size of datacube and the complexity/uncertainty in post-processing.

To provide a solution to these disadvantages, we have developed a snapshot retinal imaging MM polarimeter (SRIMMP) system based on channeled imaging polarimetry (CIP) technique. The spatial-spatial modulation and analysis of the polarization states makes it possible to acquire the whole 2D MM from a single snapshot image. This greatly reduces the image acquisition time and datacube size, also eliminates the needs of data concatenation and image registration in post-

processing. In addition, the device contains no moving part, which makes it mechanically more robust comparing to most of the retinal imaging polarimeters in current clinical application.

With the establishment of the SRIMMP device, we tried to answer several scientific questions: First, is the polarization grating(PG) based snapshot imaging MM polarimeter (SIMMP) design realizable? Second, is it possible to combine the SIMMP polarimeter with a retinal camera to give it the ability of acquiring data from human retina? Third, is it possible to accurately reconstruct 2D MM from human retina using a single snapshot image taken by the device? The answers to these questions can be found form different chapters of this dissertation. In this dissertation, Chapter 2 provides a brief introduction to Jones calculus and Mueller calculus, along with a review of snapshot channeled imaging polarimeters developed in recent years. It also explains the fundamental principles of SRIMMP. Chapter 3 discusses the optical design and opto-mechanical design of the SRIMMP device. In Chapter 4 and Chapter 5, the procedure of system calibration and MM reconstruction are demonstrated both theoretically and practically. Chapter 6 describes the preliminary clinical tests performed in the University of Southern California (USC). Chapter 7 concludes this work and provides some suggestions for future improvements of the system.

References

- [1] Wikipedia User: Srleffler. (2012, December 8). Mueller calculus. Retrieved from https://en.wikipedia/wiki/Mueller_calculus.
- [2] Goldstein, D. H. (2011). *Polarized light*. Boca Raton, FL: CRC Press.
- [3] Lu, S. Y., & Chipman, R. A. (1996). Interpretation of Mueller matrices based on polar decomposition. *JOSA A*, 13(5), 1106-1113.
- [4] Ossikovski, R., Anastasiadou, M., & De Martino, A. (2008). Product decompositions of depolarizing Mueller matrices with negative determinants. *Optics Communications*, 281(9), 2406-2410.
- [5] Tyo, J. S., Goldstein, D. L., Chenault, D. B., & Shaw, J. A. (2006). Review of passive imaging polarimetry for remote sensing applications. *Applied optics*, 45(22), 5453-5469.
- [6] Smith, M. H., Burke, P. D., Lompado, A., Tanner, E. A., & Hillman, L. W. (2000, May). Mueller matrix imaging polarimetry in dermatology. In *Biomedical Diagnostic, Guidance, and Surgical-Assist Systems II* (Vol. 3911, pp. 210-217). International Society for Optics and Photonics.
- [7] Dreher, A. W., & Reiter, K. (1992, December). Scanning laser polarimetry of the retinal nerve fiber layer. In *Polarization Analysis and Measurement* (Vol. 1746, pp. 34-42). International Society for Optics and Photonics.
- [8] Scarrott, S. M., Rolph, C. D., & Tadhunter, C. N. (1990). Imaging polarimetry of the high-z radio galaxy 3C368. *Monthly Notices of the Royal Astronomical Society*, 243, 5P-9P.
- [9] Gledhill, T. M., Chrysostomou, A., Hough, J. H., & Yates, J. A. (2001). Axisymmetry in protoplanetary nebulae: using imaging polarimetry to investigate envelope structure. *Monthly Notices of the Royal Astronomical Society*, 322(2), 321-342.

- [10] Miura, M., Elsner, A. E., Iwasaki, T., Yamanari, M., Yatagai, T., & Yasuno, Y. (2007). Imaging Polarimetry in Age Related Macular Degeneration. *Investigative Ophthalmology & Visual Science*, 48(13), 2857-2857.
- [11] Ervin, A. M., Boland, M. V., Myrowitz, E. H., Prince, J., Hawkins, B., Vollenweider, D., ... & Robinson, K. A. (2012). Screening for glaucoma: comparative effectiveness.
- [12] Quigley, H. A., & Broman, A. T. (2006). The number of people with glaucoma worldwide in 2010 and 2020. *British journal of ophthalmology*, 90(3), 262-267.
- [13] Fortune, B., Burgoyne, C. F., Cull, G., Reynaud, J., & Wang, L. (2013). Onset and progression of peripapillary retinal nerve fiber layer (RNFL) retardance changes occur earlier than RNFL thickness changes in experimental glaucoma. *Investigative ophthalmology & visual science*, 54(8), 5653-5661.
- [14] Twietmeyer, K. M., Chipman, R. A., Elsner, A. E., Zhao, Y., & VanNasdale, D. (2008). Mueller matrix retinal imager with optimized polarization conditions. *Optics express*, 16(26), 21339-21354.
- [15] Toth, M., & Hollo, G. (2005). Enhanced corneal compensation for scanning laser polarimetry on eyes with atypical polarisation pattern. *British Journal of Ophthalmology*, 89(9), 1139-1142.
- [16] Klein Brink, H. B., & Van Bloklant, G. J. (1988). Birefringence of the human foveal area assessed in vivo with Mueller-matrix ellipsometry. *JOSA A*, 5(1), 49-57.
- [17] Bueno, J. M., & Artal, P. (1999). Double-pass imaging polarimetry in the human eye. *Optics letters*, 24(1), 64-66.
- [18] Stevenson, S. B., & Roorda, A. (2005, May). Correcting for miniature eye movements in high resolution scanning laser ophthalmoscopy. In *Proc. SPIE* (Vol. 5688, pp. 145-151).

Chapter 2 Snapshot Channeled Polarimeter

Different from traditional rotation-based polarimeters, snapshot channeled polarimeters modulate polarization information onto spectral or spatial channels and reconstruct polarization parameters through channel demodulation in post-processing. Depending upon the polarization parameters being measured, snapshot channeled polarimeters can be divided into two major categories: snapshot channeled Stokes polarimeter, which measures Stokes parameters from the incident light; and snapshot channeled Mueller matrix (MM) polarimeter, which measures the MMs of samples under test. Both kinds of snapshot channeled polarimeters would be briefly discussed in this chapter, along with a conceptual introduction of Jones calculus and Mueller calculus. A brief introduction to the generalized channeled polarimetry theory would also be given in the last section of this chapter.

2.1 Polarization of light and its representation

As a kind of electromagnetic radiation, light has an electric field that can vary in both time and space. The concept of polarization is created to describe the oscillation of electric field of light [1,2]. For example, light with linear polarization has its electric field oscillates only in one direction, while the electric field direction of circularly polarized light constantly changes along propagation, with its tip draws a circular contour. According to different behaviors of the electric fields, the polarization of light can be divided into several different categories, including linear polarization, circular polarization, elliptical polarization, and random polarization [3].

2.1.1 Jones vector and Jones matrix

Jones calculus was developed in the 1940s by R. C. Jones as matrix formulation of polarization states of light [1]. In Jones calculus, the polarization state of a light field is denoted by its amplitudes and phases in two orthogonal directions in a 2×1 vector [3]

$$\mathbf{E} = \begin{bmatrix} \mathbf{E}_x \\ \mathbf{E}_y \end{bmatrix} = \begin{bmatrix} E_{0x} e^{i\delta_x} \\ E_{0y} e^{i\delta_y} \end{bmatrix}, \quad (1)$$

where \mathbf{E}_x and \mathbf{E}_y denote the electric field components along x and y directions, respectively. E_{0x} and E_{0y} are the amplitudes of E_x and E_y , while δ_x and δ_y are the phases of E_x and E_y . i denotes the imaginary part of a complex value. A polarizing element is denoted by a 2×2 matrix in Jones calculus

$$\mathbf{J} = \begin{bmatrix} J_{xx} & J_{xy} \\ J_{yx} & J_{yy} \end{bmatrix}, \quad (2)$$

and its interaction with a polarized light field is described by matrix multiplication

$$\mathbf{E}_{\text{out}} = \mathbf{J}\mathbf{E}_{\text{in}}, \quad (3)$$

where \mathbf{E}_{in} is the Jones vector of the input light and \mathbf{E}_{out} is the Jones vector of the output light.

2.1.2 Stokes vector and Mueller matrix

In addition to Jones calculus, the polarization of light can also be described by another matrix formulation, which is called Mueller calculus. Stokes vector and MM are both linear algebra concepts used in Mueller calculus. It was discovered in 1852 by Sir George Gabriel Stokes that any polarization state of light can be described by four quantities, which are later known as Stokes parameters [3]. The four Stokes parameters are expressed in Eq. 4 through Eq. 7 with light intensity terms that can be directly measured in practical tests.

$$S_0 = I_H + I_V, \quad (4)$$

$$S_1 = I_H - I_V, \quad (5)$$

$$S_2 = I_{+45} - I_{-45}, \quad (6)$$

$$S_3 = I_{RC} - I_{LC}, \quad (7)$$

where I_H is the intensity of linear polarization component in horizontal direction, I_V is the intensity of linear polarization component in vertical direction. I_{+45} and I_{-45} are the intensities of linear polarization components in $+45^\circ$ and -45° , respectively. I_{RC} and I_{LC} represent the intensities of right circular and left circular polarization components.

The four Stokes parameters can be combined into a 4×1 vector, which is called Stokes vector

$$\mathbf{S} = \begin{bmatrix} S_0 \\ S_1 \\ S_2 \\ S_3 \end{bmatrix}. \quad (8)$$

When light interacts with certain objects (reflection, refraction, transmission *etc.*), its polarization state often changes. This polarization alternating process, as discovered by Hans Mueller in 1943 [3], can be described by the multiplication between the 4×1 input Stokes vector and a 4×4 real matrix related to the polarization properties of the objects. The 4×4 real matrix is now known as Mueller matrix. If we denote the Stokes vector of the input light as \mathbf{S}_{in} , and the output Stokes vector as \mathbf{S}_{out} , then

$$\mathbf{S}_{out} = \mathbf{M}\mathbf{S}_{in}, \quad (9)$$

where

$$\mathbf{M} = \begin{pmatrix} m_{00} & m_{01} & m_{02} & m_{03} \\ m_{10} & m_{11} & m_{12} & m_{13} \\ m_{20} & m_{21} & m_{22} & m_{23} \\ m_{30} & m_{31} & m_{32} & m_{33} \end{pmatrix}. \quad (10)$$

Polarization-related properties of the object, such as diattenuation, retardance and depolarization are encoded within the MM. These properties can be decomposed from the MM by applying techniques such as the Lu-Chipman decomposition [4].

In description of polarization states, the main differences between Mueller calculus and Jones calculus are: 1) Jones calculus only applies to coherent light, while Mueller calculus only applies to incoherent light, 2) Jones calculus includes information of phase evolution, while Mueller calculus contains no information of phase, and 3) Jones calculus can only be used for the description of fully polarized light, while Mueller calculus can describe fully polarized light, partially polarized light and unpolarized light. Due to these differences, Jones calculus is mainly used for interference related analysis, while Mueller calculus is mainly used for light intensity related analysis.

2.2 Snapshot channeled Stokes polarimeters

To measure the Stokes parameters of light, channeled polarimeters usually create wavelength-dependent or location-dependent analyzing states using optical components such as prisms, retarders, linear polarizers (LP) and polarization gratings (PG). Using this method, multiple polarization-state-dependent channels are formed spectrally or spatially, or a combination of both. With spectral or spatial modulations, it is easy for the channeled Stokes polarimeters to have a snapshot feature, as shown in many proposed systems [5-10].

2.2.1 Snapshot channeled Stokes polarimeters with spectral modulation

Snapshot channeled Stokes polarimeters in this category usually work with relatively broadband illumination sources to ensure enough separations among wavelength channels. In 1999, Oka and Kato reported a spectroscopic channeled polarimeter design using two thick retarders and a LP as polarization state analyzer [11]. The conceptual sketch of the device is as depicted below,

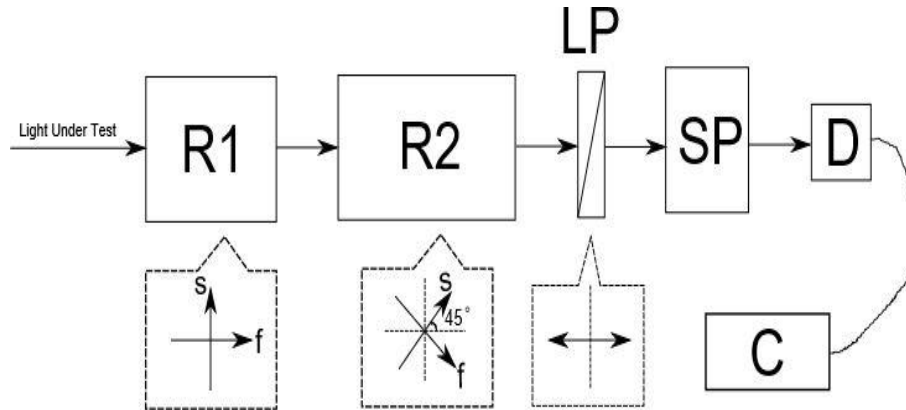


Figure. 2-1. Schematic of the spectroscopic polarimeter as reported by Oka and Kato [11].

In Figure. 2-1, R_1 and R_2 are thick retarders with a 45° angle between their fast axes. LP is a linear polarizer with its transmission axis parallel to the fast axis of R_1 . SP represents a spectrometer. D is a photodetector and C is a computer used to record and process data from the polarimeter. The light with unknown polarization states has a broadband spectrum. Since the phase retardances of thick retarders R_1 and R_2 change along with wavelengths, a channeled spectrum with cosinusoidal modulation would be captured at the receiving end of the system by the spectrometer and photodetector. The Fourier inversion of the channeled spectrum gives several optical path difference (OPD) channels and each channel contains the information of one or two Stokes parameters. Through channel isolation and phase compensation, the four components in Stokes vector can be determined. Comparing to the traditional Stokes polarimeters, this system uses no mechanically movable components to control analyzing states, which greatly reduces the system's complexity and obviates the problems like vibrating and heating. Only a single channeled

spectrum needs to be recorded in this method, however, this does not indicate a snapshot feature due to the scanning nature of the spectrometer used to acquire the spectrum. In 2002, Sabatke *et al.* modified the Oka and Kato's design by combining the spectroscopic channeled polarimeter with a computed tomography imaging channeled spectropolarimeter (CTIS), converting it into a snapshot channeled imaging spectropolarimeter [5]. In the snapshot channeled imaging spectropolarimeter system, the analyzer of the spectroscopic channeled polarimeter is inserted into the CTIS system between collimating optics and holographic dispenser, giving it the ability to record the whole channeled spectrum with a single snapshot. The authors also proposed data reconstruction model for the device and did simulations to verify the usefulness of the model. The simulation results show good agreement between reconstructed Stokes parameters and the original input. In 2014, Van Harten *et al.* reported a dual-beam implementation of channeled Stokes polarimetry with spectral modulation [12]. The device was successfully used to measure the polarization states of scattered light from blue sky. Kudenov *et al.* demonstrated a complete Fourier transform spectropolarimeter (FTSP) based upon the channeled spectral technique [6]. Two Yttrium Vanadate (YVO₄) crystals were used to make the system operate at mid-wavelength infrared band (MWIR). The reference beam technique was adopted for system calibration [6]. To investigate the influence of dichroism effect on the Stokes vector reconstruction accuracy, the authors developed an improved model of the FTSP, which is as shown below in Figure. 2-2.

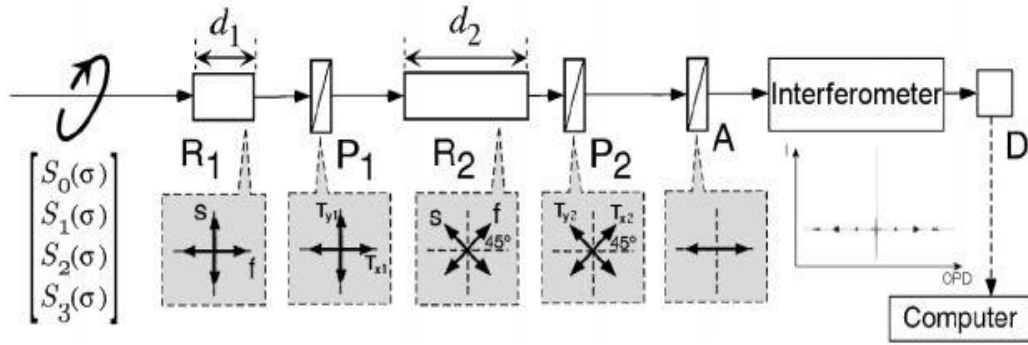


Figure. 2-2. Improved FTSP system model used to investigate the influence of dichroism on the reconstruction results, developed by Kudenov *et al.* [6].

In Figure. 2-2, T_{x1} , T_{y1} , T_{x2} , T_{y2} are transmission attenuation coefficients associated with partial polarizers P_1 and P_2 , which are used to simulate polarization-dependent transmission in the corresponding directions. Based on the analysis of the improved model, the authors derived the expression of the channeled spectrum with dichroism and improved the reference beam calibration procedure according to the expression. Tests of the system showed that, with the improved calibration, the average absolute error in Stokes parameter reconstruction was brought down from 8.7% to 1.07% for S_1 , from 2.84% to 1.06% for S_2 , and from 2.2% to 1,06% for S_3 . This experiment had shown that FTSP technique has great potential in the MWIR band.

2.2.2 Snapshot channeled Stokes polarimeters with spatial modulation

By simply switching the thick retarders in Oka and Kato's spectroscopic polarimeter to birefringent wedge prisms, polarization information from incident light could be modulated onto spatial channels instead of spectral channels, which transfers channeled Stokes polarimeter from spectral analysis to spatial analysis. This idea was first proposed in 2003 by Oka and Kaneko [7]. The schematic of the proposed polarimeter is as depicted below in Figure. 2-3.

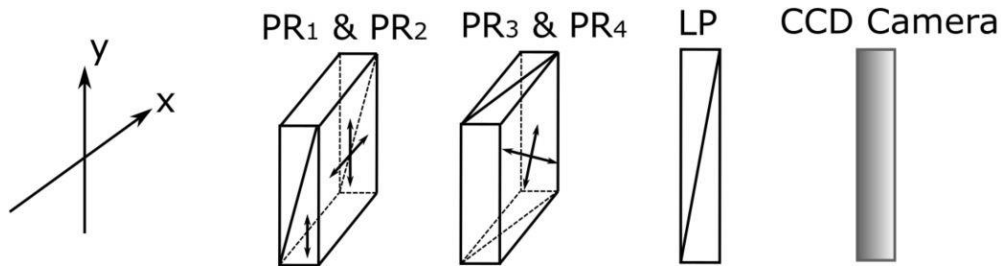


Figure. 2-3. Schematic of the polarimetric analyzer with spatial channel modulation as described by Oka and Kaneko in [7].

In Figure. 2-3, PR_1 , PR_2 , PR_3 and PR_4 are wedge prisms with birefringence, they are assembled into two pairs to provide spatial-dependent retardance. LP is a linear polarizer with transmission axis parallel to the horizontal axis, which is used to transfer the spatial-dependent retardance into spatial-dependent intensity patterns. The fast axes of PR_1 and PR_2 , are parallel to the horizontal and vertical axes while the fast axes of PR_3 and PR_4 are oriented 45° and -45° relative to the horizontal direction. This arrangement creates an intensity pattern on the CCD camera with 4 frequency components (including DC). After filtering the spatial frequency channels in Fourier domain and applying inverse Fourier transform to the filtered contents, 4 channels could be obtained in spatial domain, with channel 1 associated with S_0 , channel 2 associated with S_1 , channel 3 and channel 4 both associated with S_2+iS_3 . With reference beam calibration, the Stokes parameters can be easily resolved. The authors validated the model by reconstructing the spatial variant Stokes parameters of a 2D scene, the power spectrum of the intensity pattern received on the CCD camera is as depicted below in Figure. 2-4.

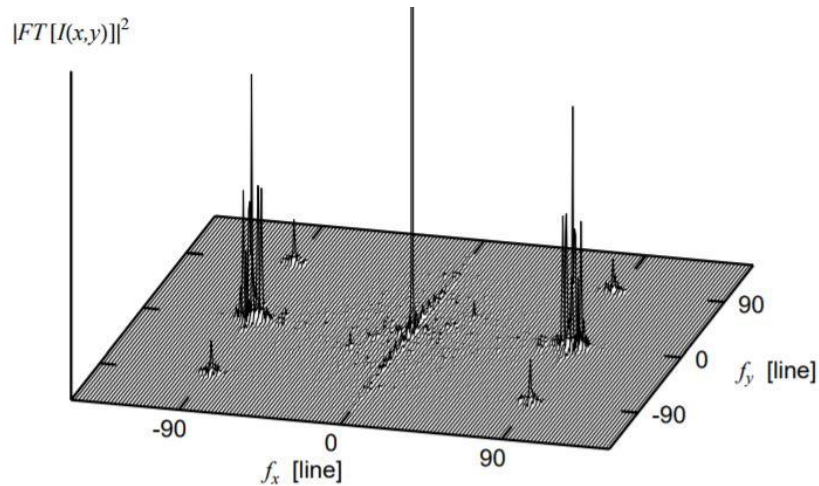


Figure. 2-4. Power spectrum of the intensity pattern captured in Oka and Kaneko’s channeled spatial polarimeter experiment [7].

The use of birefringent wedge prisms helps to keep the polarimeter system simple and compact. However, the beam-splitting errors from the prisms prevents the system from acquiring high spatial resolution intensity fringes. Thus, the spatial resolution of reconstructed Stokes parameters is limited. To solve this problem, Oka and Saito substituted the wedge prisms in the system with a pair of Savart plates (along with an additional half wave plate between the two Savart plates comparing to the original prism-based system) [8]. Kudenov *et al.* continued to replace the Savart plates (SP) with first a dispersion-compensated polarization Sagnac interferometer (DCPSI) and then a pair of polarization gratings (PG), to give the system the ability of reconstructing spatial variant Stokes parameters from broadband/white light source, which makes the system more appealing for practical applications [9,10]. Rectifications to the calibration and data reconstruction approaches were developed in correspondence to the change in system structure and components.

2.3 Snapshot channeled Mueller matrix polarimeters

The task of MM polarimeters is to acquire the MM of the sample under test. Different from Stokes polarimeters, a MM polarimeter must control both incident and analyzing polarization

states to obtain MM. This requirement often makes the configurations of MM polarimeters more complicated when compared to Stokes polarimeters. Because of the increased complexity, channeled MM polarimeters were developed later than channeled Stokes polarimeters in the history. Comparing to dual-rotational MM polarimeter, channeled MM polarimeters often have advantages such as enhanced robustness and simpler data acquisition/post-processing.

2.3.1 Snapshot channeled Mueller matrix polarimeters with spec-spec modulation

In 2007, Hagen *et al.* presented a snapshot MM polarimetry technique based on channeled spectrum [13]. The design extends the concept of channeled spectropolarimetry to not only controlling the analyzing polarization states but also controlling the input polarization states. The schematic of the polarimeter's configuration is as shown below in Figure. 2-5.

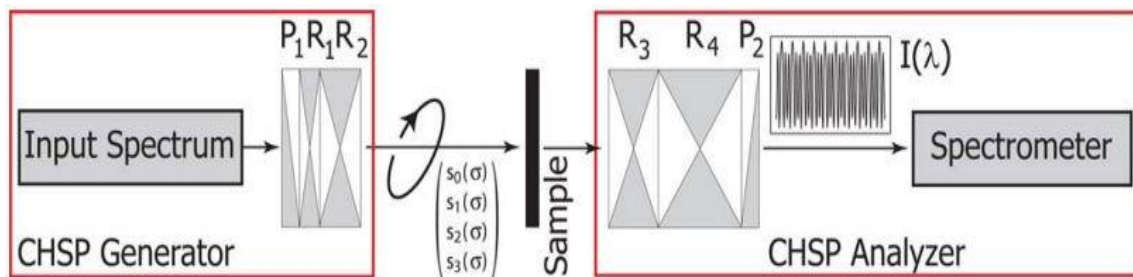


Figure. 2-5. Layout of the snapshot Mueller matrix spectropolarimeter proposed by Hagen *et al.* [13].

where P_1 and P_2 are LPs with their transmission axes oriented at 0° . R_1 and R_4 are retarders with fast axes oriented at 45° . R_2 and R_3 represent retarders with fast axes oriented at 0° . With proper choice of retarders' thicknesses, MM elements can be spread onto multiple spectral channels. When the thicknesses of R_1 , R_2 , R_3 and R_4 have a 1-2-5-10 ratio, the channel contents are as listed below in Table 2-1. By applying linear operations to the complex channel contents listed above, all the 16 MM elements can be demodulated.

Table 2-1. Fourier domain channel contents of the snapshot Mueller matrix spectropolarimeter proposed by Hagen *et al.* [13].

Channel	Content $\times (64/S_{in,0})$
C_0	$16m_{00}$
$C_{\pm 1}$	$8m_{01}+4m_{02}\pm 4im_{03}$
$C_{\pm 2}$	$-m_{22}\pm im_{23}\mp im_{32}-m_{33}$
$C_{\pm 3}$	$-4m_{02}\mp 4im_{03}$
$C_{\pm 4}$	$2m_{21}+m_{22}\mp im_{23}\pm 2im_{31}\pm im_{32}+m_{33}$
$C_{\pm 5}$	$4m_{20}\pm 4im_{30}$
$C_{\pm 6}$	$2m_{21}+m_{22}\pm im_{23}\pm 2im_{31}\pm im_{32}-m_{33}$
$C_{\pm 7}$	$-2m_{12}\pm 2im_{13}$
$C_{\pm 8}$	$-m_{22}\mp im_{23}\mp im_{32}+m_{33}$
$C_{\pm 9}$	$4m_{11}+2m_{12}\mp 2im_{13}$
$C_{\pm 10}$	$8m_{10}$
$C_{\pm 11}$	$4m_{11}+2m_{12}\pm 2im_{13}$
$C_{\pm 12}$	$m_{22}\mp im_{23}\mp im_{32}-m_{33}$
$C_{\pm 13}$	$-2m_{12}\mp 2im_{13}$
$C_{\pm 14}$	$-2m_{21}-m_{22}\pm im_{23}\pm 2im_{31}\pm im_{32}+m_{33}$
$C_{\pm 15}$	$-4m_{20}\pm 4im_{30}$
$C_{\pm 16}$	$-2m_{21}-m_{22}\mp im_{23}\pm 2im_{31}\pm im_{32}-m_{33}$
$C_{\pm 18}$	$m_{22}\pm im_{23}\mp im_{32}+m_{33}$

In the same year of 2007, another group of researchers reported a snapshot MM polarimeter with essentially the same configuration as described by Hagen [14]. Apart from theoretical demonstration, the authors also validated the system with experimental results from testing vacuum and polarizer. After multiple correction methods applied to the raw data, the authors were

able to limit the residue errors of vacuum tests and LP tests within 2% and 8%, respectively. The authors also claimed that the accuracy of the system depends a lot on systematic errors, with a better-adapted spectrometer, the performance could be enhanced significantly. This work is the first experimental validation of snapshot MM polarimeter technique. It also has the potential to be modified into a snapshot channeled imaging MM polarimeter by replacing the non-imaging spectrometer with an imaging spectrometer.

2.3.2 Snapshot channeled Mueller matrix polarimeters with spat-spat modulation

Following the same thought process of spectral-based channeled MM polarimeters, spatial-based channeled MM polarimeters can be made by adding spatial-modulated polarization states to the incident light in a channeled Stokes polarimeter setup. The system configuration of channeled imaging MM polarimeter with spatial-spatial modulation was first brought up by Kudenov *et al.* in 2012 [15].

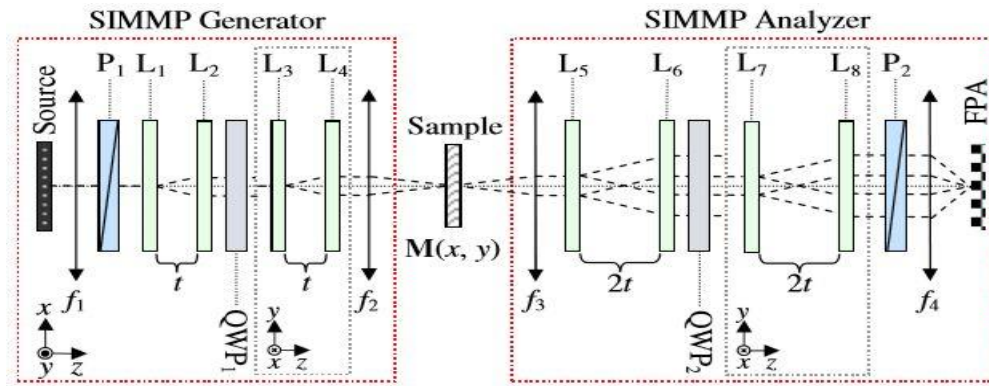


Figure. 2-6. Layout of the snapshot imaging Mueller matrix spectropolarimeter (SIMMP) proposed by Kudenov *et al.* [15].

In the system, there are both polarization state generator (PSG) and polarization state analyzer (PSA), as shown in Figure. 2-6. L_1, L_2, L_5 and L_6 are polarization gratings (PGs) that shear the incident light in x direction, while PGs L_3, L_4, L_7 and L_8 shear the incident light along y direction. P_1 and P_2 are LPs with fast axes oriented 45° to the x direction. QWP_1 and QWP_2 are quarter wave

plates with fast axes at 45° and 0° , respectively. All the PGs have a same grating period, and the distance between PGs in PSA is twice as big as that in PSG. With this configuration, each beam from the incident light field would be separated into 16 beams with different polarization states. These beams are then re-focused onto the FPA by lens f_4 after passing through polarizer P_2 , which generates polarization-related intensity fringes on top of the scene. In the process, the MM elements from the sample are modulated onto the spatial frequency components of the intensity fringes. The Fourier domain of the intensity fringes on FPA is as depicted in Figure. 2-7.

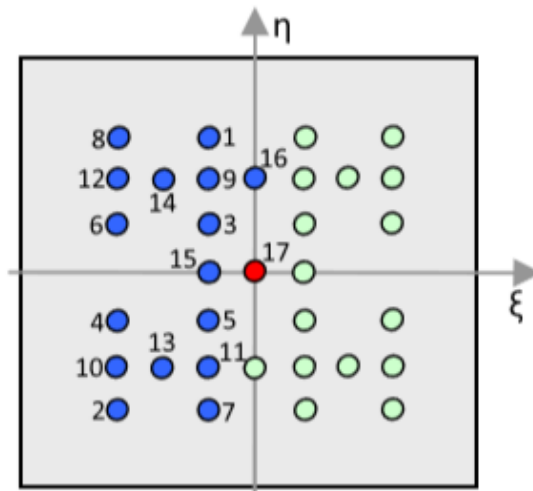


Figure. 2-7. Fourier domain of intensity fringes recorded by the SIMMP [15].

Isolate the labeled frequencies in Figure. 2-7 one by one and apply inverse Fourier transform to the contents, 17 filtered spatial frequency channels could be acquired, each carries the information of one or multiple MM elements. After calibration and phase demodulation, the spatial frequency channels could be algebraically combined to isolate the 16 MM elements. The proposed device could work with monochromatic or broadband/white light source, depending upon the working bandwidth of the PGs in it.

2.3.3 Snapshot channelled Mueller matrix polarimeter with spec-spat modulation

The possibility of a snapshot polarimeter system with spectral-spatial or spatial-spectral modulation/analysis was first mentioned in Alenin and Tyo's work [16]. In 2017, K. Oka *et al.* proposed a hyperspectroscopic channelled MM polarimeter which uses spectral modulation and spatial analysis to measure the MMs of the samples under test [17]. As depicted in Figure. 2-8, the PSG of the device consists of a polarizer P and two high-order retarders R_1 and R_2 , which spectrally modulates the polarization states of the light from the wavelength scanning source. The PSA of the device consists of two Savart plates SP_1 and SP_2 , an achromatic half wave plate $AHWP$, and a linear polarizer A , which splits the light from the sample into 4 beams according to its polarization states. The 4 beams are eventually re-focused onto the image sensor by lens L_2 to create an interference pattern, which contains several spatial frequency components as carriers of Stokes parameters information from the sample.

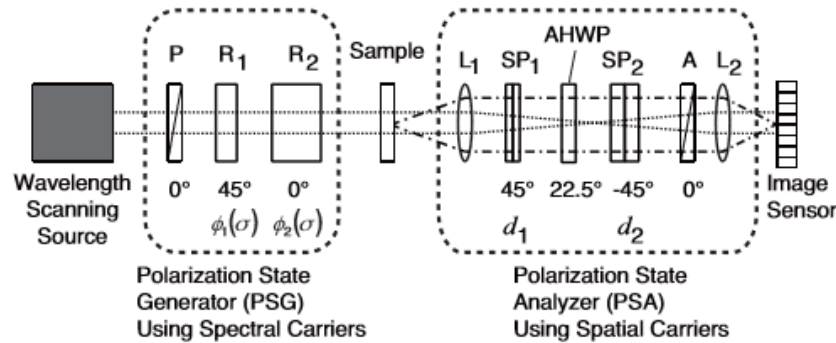


Figure. 2-8. Sketch of the hyperspectroscopic channelled Mueller matrix polarimeter as described in [17].

As described above, in this system the polarization states of the light are spectrally modulated and spatially analyzed. All the 16 MM elements can be simultaneously solved from the datacube constructed using both spatial and spectral coordinates. Due to wavelength scanning, it takes some time for the system depicted in Figure. 2-8 to collect all the data. To transfer the system into a snapshot system, the wavelength scanning source needs to be replaced by a white light

source, and the image sensor at the end of the system needs to be replaced by an imaging spectrometer accordingly.

2.4 Polarimeters based on polarization gratings

Polarization gratings are optical components that can efficiently diffract incident light into +1 and/or -1 orders with orthogonal polarization states [18]. A PG is analogous to glass beamsplitters such as Wollaston prism and Nomarski prism, with smaller physical size and larger spectral bandwidth. Thus, PGs have great potential for applications in multiple domains of optical engineering.

Before the introduction of PG-based snapshot polarimeters discussed in sections 2.2 and 2.3, various non-snapshot polarimetric devices using PGs were developed. Comparing to traditional polarimeters, these devices hold many advantages, including high speed measurement, wide bandwidth, and compact device size. In 1999, Franco Gori theoretically demonstrated that it is possible to demodulate Stokes parameters from measured intensities of +1, -1 and 0 order diffracted beams off a polarization grating after the beams getting through a LP [19]. The LP must take two orientations during the test procedure to demodulate all four Stokes parameters, which keeps the method from being able to acquire full Stokes vector with simultaneous measurements. In 2006, Escuti *et al.* experimentally demonstrated a spectropolarimeter device design consists of three inline reactive mesogen PGs and two quarter wave plates (QWPs) with different orientations [20]. By having the fast axes of the QWPs at certain orientations, the spectropolarimeter is sensitive to all four Stokes parameters. At each wavelength, only four simultaneous intensity measurements are needed to reveal the full Stokes vector of incident light. Clementina Provenzano, Gabriella Cipparrone, and Alfredo Mazzulla reported a two-grating photopolarimeter system utilizing both polarization grating and ordinary intensity diffraction grating [21]. The incident light

is first diffracted by a PG which is sensitive to circular polarization states. A conventional transmission grating, along with two fixed LPs, is placed in the optical path after the PG to measure linear polarization components. Four photodiodes are used to record intensities of the diffracted beams for Stokes vector calculation.

2.5 Snapshot retinal imaging Mueller matrix polarimeter

The proposed retinal polarimeter is based upon the polarization-grating-based channeled snapshot MM polarimeter design proposed by Kudenov *et al* [15]. The proposed system setup is as depicted in Figure. 2-9.

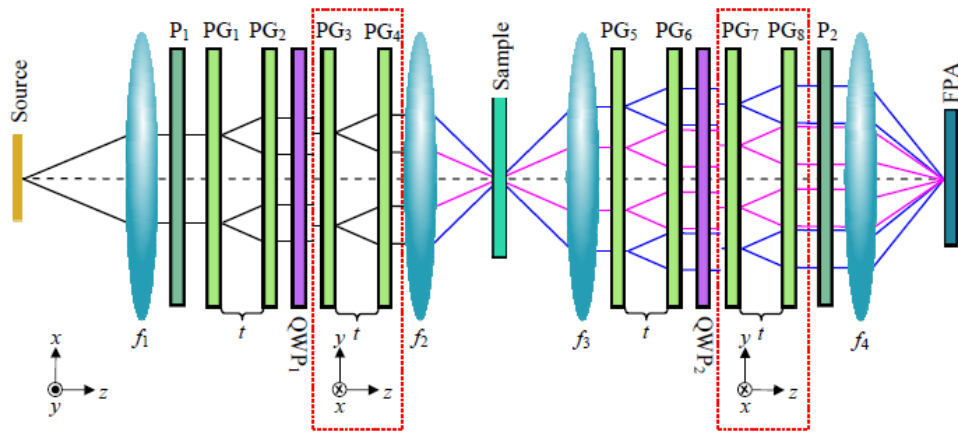


Figure. 2-9. Schematic of the snapshot imaging Mueller matrix polarimeter using pupil-plane interferometers. Each pupil-plane interferometer consists of two PGs in series. As described by Kudenov *et al.* [15].

As can be seen from Figure. 2-9, the collimated light from the illumination source is first polarized by linear polarizer P_1 before transmitted into the polarization state generator (PSG), which consists of 4 PGs and a quarter wave plate (QWP). Polarization-based dispersion generated from PG_1 is directed back to parallel propagation by PG_2 . The function of QWP_1 is to convert the circularly polarized beams produced by PG_1 and PG_2 into linear polarization states. The beams then got transmitted through PG_3 and PG_4 , which behave the same way as PG_1 and PG_2 , but in an orthogonal direction y . Then these four beams are focused onto the sample under test. This is when the sample's MM information got modulated onto the frequency components. After interaction

with the sample, the light beams are collimated and directed into the polarization state analyzer (PSA), which has similar configuration as the PSG. The light beams are eventually analyzed by a linear polarizer P_2 in the PSA before being focused onto a focal plane array (FPA) by a re-focusing lens. This forms intensity fringes on top of sample's image, which carry MM information of the sample. Table 2-2 provides a comparison of compactness, robustness, spectral bandwidth and measurement speed among several typical MM polarimeters, it can be seen that SMMP holds advantages against other types of devices.

Table 2-2. Comparison of system characteristics among typical Mueller matrix polarimeters.

Characteristic Polarimeter	Compactness	Robustness	Bandwidth	Speed
Dual-rotation polarimeter				
LC modulator polarimeter				
Snapshot MM spectropolarimeter				
SMMP				

To further reduce the complexity of the system, the originally proposed setup with 8 polarization gratings (PGs) was not adopted. Instead, a simpler image plane setup was used [22]. As can be seen from Figure. 2-10, the image plane setup reduces the number of the PGs to 4 by placing the polarization state generator (PSG) and polarization state analyzer (PSA) at focal planes conjugate to the sample under test. The PGs used for collimation in the original design are removed from this configuration, because the PSG and the PSA are placed at focal planes and their thicknesses are small (about 2 mm each), such that it is unlikely to have much shear of light beams in lateral directions. To measure MM from human retina, the snapshot imaging MM polarimeter depicted in Figure. 2-10 must be incorporated into a fundus camera design. Thus, a new optical

design must be carried out. Good optical performance must be maintained in the optical design, along with several conjugating relations among optical components.

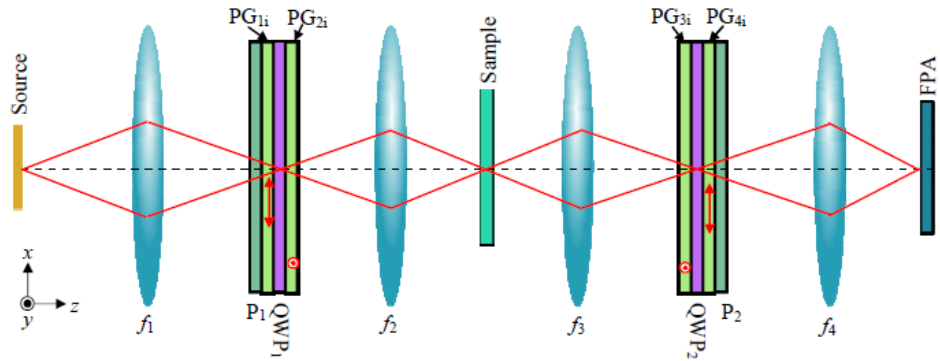


Figure. 2-10. Schematic of the snapshot imaging Mueller matrix polarimeter using image-plane Interferometers by Kudenov *et al.* [22].

To add the PSG and the PSA of the snapshot imaging MM polarimeter into a fundus camera design, two additional focal planes that are conjugate to the eye fundus must be created without changing the intrinsic relations in the fundus camera. In addition, the illumination received by the eye should not surpass ocular safety limits.

The calibration and MM reconstruction strategies are closely correlated in a channeled snapshot imaging MM polarimeter device. For the channeled snapshot imaging MM polarimeter described above, different calibration and MM reconstruction strategies have been proposed [15,22]. However, in implementation it was found that none of them is practical. In this work, we propose to treat PSA as an individual complete channeled snapshot imaging Stokes polarimeter. Using reference beam technique, 2D Stokes parameters with and without samples in the polarimeter can be extracted from the scene [23]. The MMs are reconstructed by demodulating the differences between input and output Stokes parameters. The calibration of the system can also be done by treating PSA as a standalone snapshot Stokes polarimeter and apply calibration samples known polarization states to it.

2.6 Generalized channeled polarimetry

With many channeled polarimeter designs proposed over the years, some researchers started to seek optimal configurations for devices such that the reconstruction noises can be limited to minimal. These researches usually use equally weighted variance (EWV) as metric for channeled polarimeter evaluation, which was first proposed by Sabatke *et al.* [24]. The smaller the EMV of a polarimeter is, the smaller the reconstruction noise due to channel crosstalk would be. In 2008, lemillet *et al.* discussed the optimality of a spectral-modulated channeled snapshot MM polarimeter through evaluating the relationship between system EMV and waveplate thicknesses [25]. Later in 2014, Alenin and Tyo extended the conclusion to provide a general tool for channeled polarimeter evaluation [16]. The authors proposed a matrix called frequency phase matrix (FPM), which is like a look-up-table of channel contents' forms, weight and phases at different frequencies. For a specific channeled polarimeter configuration, corresponding rows can be extracted from FPM to match the contributing frequencies and form the modulation vector. Combine the modulation vectors of unknown parameters (e.g. MM elements) together, a modulation matrix can be formed. The optimality of the polarimeter can then be revealed by calculating the EMV of the modulation matrix. With this method, the authors evaluated several channeled polarimeter designs and suggested changes in the configurations to minimize reconstruction noise, they also went on to design new polarimeter system with the principles from their optimality evaluation method [26-28].

References

- [1] Goldstein, D. H. (2011). *Polarized light*. Boca Raton, FL: CRC Press.
- [2] Mack, C. A. (2006). *Field guide to optical lithography* (Vol. 6). Bellingham, WA: SPIE Press.
- [3] Collett, E. (2005). *Field guide to polarization* (Vol. 15). Bellingham: SPIE press.
- [4] Lu, S. Y., & Chipman, R. A. (1996). Interpretation of Mueller matrices based on polar decomposition. *JOSA A*, *13*(5), 1106-1113.
- [5] Sabatke, D. S., Locke, A. M., Dereniak, E. L., Descour, M. R., Garcia, J. P., Hamilton, T. K., & McMillan, R. W. (2002). Snapshot imaging spectropolarimeter. *Optical engineering*, *41*(5), 1048-1055.
- [6] Kudenov, M. W., Hagen, N. A., Dereniak, E. L., & Gerhart, G. R. (2007). Fourier transform channeled spectropolarimetry in the MWIR. *Optics express*, *15*(20), 12792-12805.
- [7] Oka, K., & Kaneko, T. (2003). Compact complete imaging polarimeter using birefringent wedge prisms. *Optics express*, *11*(13), 1510-1519.
- [8] Oka, K., & Saito, N. (2006, September). Snapshot complete imaging polarimeter using Savart plates. In *Infrared Detectors and Focal Plane Arrays VIII* (Vol. 6295, p. 629508). International Society for Optics and Photonics.
- [9] Kudenov, M. W., Jungwirth, M. E., Dereniak, E. L., & Gerhart, G. R. (2009). White light Sagnac interferometer for snapshot linear polarimetric imaging. *Optics express*, *17*(25), 22520-22534.

- [10] Kudenov, M. W., Escuti, M. J., Dereniak, E. L., & Oka, K. (2011). White-light channeled imaging polarimeter using broadband polarization gratings. *Applied optics*, 50(15), 2283-2293.
- [11] Oka, K., & Kato, T. (1999). Spectroscopic polarimetry with a channeled spectrum. *Optics Letters*, 24(21), 1475-1477.
- [12] Van Harten, G., Snik, F., Rietjens, J. H., Smit, J. M., & Keller, C. U. (2014). Spectral line polarimetry with a channeled polarimeter. *Applied Optics*, 53(19), 4187-4194.
- [13] Hagen, N., Oka, K., & Dereniak, E. L. (2007). Snapshot Mueller matrix spectropolarimeter. *Optics letters*, 32(15), 2100-2102.
- [14] Dubreuil, M., Rivet, S., Le Jeune, B., & Cariou, J. (2007). Snapshot Mueller matrix polarimeter by wavelength polarization coding. *Optics express*, 15(21), 13660-13668.
- [15] Kudenov, M. W., Escuti, M. J., Hagen, N., Dereniak, E. L., & Oka, K. (2012). Snapshot imaging Mueller matrix polarimeter using polarization gratings. *Optics letters*, 37(8), 1367-1369.
- [16] Alenin, A. S., & Tyo, J. S. (2014). Generalized channeled polarimetry. *JOSA A*, 31(5), 1013-1022.
- [17] Oka, K., Sayama, K., & Michida, H. (2017, September). Hyperspectroscopic Mueller-matrix polarimeter based on channeled polarimetry. In *Polarization Science and Remote Sensing VIII* (Vol. 10407, p. 104070M). International Society for Optics and Photonics.
- [18] Oh, C., & Escuti, M. J. (2008). Achromatic diffraction from polarization gratings with high efficiency. *Optics letters*, 33(20), 2287-2289.
- [19] Gori, F. (1999). Measuring Stokes parameters by means of a polarization grating. *Optics letters*, 24(9), 584-586.

- [20] Escuti, M. J., Oh, C., Sánchez, C., Bastiaansen, C., & Broer, D. J. (2006, September). Simplified spectropolarimetry using reactive mesogen polarization gratings. In *Imaging Spectrometry XI* (Vol. 6302, p. 630207). International Society for Optics and Photonics.
- [21] Provenzano, C., Cipparrone, G., & Mazzulla, A. (2006). Photopolarimeter based on two gratings recorded in thin organic films. *Applied optics*, 45(17), 3929-3934.
- [22] Kudenov, M. W., Mallik, S., Escuti, M. J., Hagen, N., Oka, K., & Dereniak, E. L. (2013, October). Snapshot imaging Mueller matrix instrument. In *Electro-Optical Remote Sensing, Photonic Technologies, and Applications VII; and Military Applications in Hyperspectral Imaging and High Spatial Resolution Sensing* (Vol. 8897, p. 88970S). International Society for Optics and Photonics.
- [23] Wang, Y., Kudenov, M., Kashani, A., Schwiegerling, J., & Escuti, M. (2015, September). Snapshot retinal imaging Mueller matrix polarimeter. In *Polarization Science and Remote Sensing VII* (Vol. 9613, p. 96130A). International Society for Optics and Photonics.
- [24] Sabatke, D. S., Descour, M. R., Dereniak, E. L., Sweatt, W. C., Kemme, S. A., & Phipps, G. S. (2000). Optimization of retardance for a complete Stokes polarimeter. *Optics Letters*, 25(11), 802-804.
- [25] Lemaillet, P., Rivet, S., & Le Jeune, B. (2008). Optimization of a snapshot Mueller matrix polarimeter. *Optics letters*, 33(2), 144-146.
- [26] Alenin, A. S., & Tyo, J. S. (2016). Design of channeled partial Mueller matrix polarimeters. *JOSA A*, 33(6), 1060-1070.
- [27] Alenin, A. S., Vaughn, I. J., & Tyo, J. S. (2017, September). A nine-channeled partial Mueller matrix polarimeter. In *Polarization Science and Remote Sensing VIII* (Vol. 10407, p. 104070L). International Society for Optics and Photonics.

[28] Vaughn, I. J., Alenin, A. S., & Tyo, J. S. (2017, September). A fast Stokes polarimeter: preliminary design. In *Polarization Science and Remote Sensing VIII* (Vol. 10407, p. 1040702). International Society for Optics and Photonics.

Chapter 3 System Design and Assembly

To build a functional snapshot imaging Mueller matrix (MM) retinal polarimeter system, optical design and opto-mechanical design need to be carried out. The purpose of optical design is to find a way of combining the snapshot imaging MM polarimeter system with a fundus camera, while maintaining good optical performance in the combined optical system. Opto-mechanical design is to be conducted after the optical design, to provide a plan to integrate the optics in the optical design into a functional instrument. In this work, the optical design was conducted in Zemax, and the opto-mechanical design was conducted in both Autodesk Inventor and Solidworks.

3.1 Optical designs

3.1.1 Optical design of SRIMMP

A fundus camera is an imaging device specifically designed to photograph the interior surface of human eye [1]. It has been used for the diagnosis of certain retinal diseases for almost a century [2]. The designs of fundus cameras can be roughly divided into two categories according to different illumination styles: internal illumination design and external illumination design [3]. Two conceptual sketches of internal and external illumination designs are as shown in Figure. 3-1. As can be seen, in the internal illumination layout, the objective lens $2b$ locates right next to patient's eye. A holed mirror (or polarization beam-splitter in some designs) $3b$, is used to separate the illumination pathway from the imaging pathway. A black dot $8b$, is placed in conjugation with the back surface of the objective to reduce reflection from it. An annulus $10b$, which forms a doughnut-shaped image on the surface of cornea, helps to reduce corneal reflection. An advantage of internal illumination layout is that, the distance between eye and the objective lens can be made relatively large by simply changing the focal length of the objective lens, making it easier to create a comfortable optical interface for patients. Another advantage is the potentially larger field of

view (FOV). The major drawback of internal illumination design is its comparatively complicated system configuration. In external illumination design, the objective lens $3a$ is only in the imaging pathway. The two optical pathways are separated right in front of the eye by a beamsplitter $2a$. There is no need to include a blockage for objective lens reflection because the objective lens is excluded from the illumination system. Annulus $9a$ functions in the same way as its counterpart in the internal illumination design. Comparing to internal illumination design, it is harder to have a big eye relief, but the complexity of system configuration is smaller.

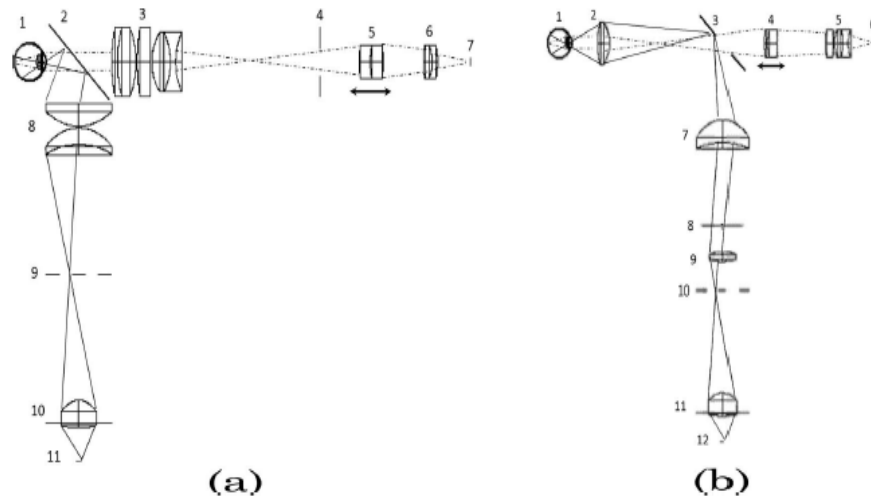


Figure. 3-1. Sketches of fundus camera designs with a) external and b) internal illuminations [3].

To successfully combine the imaging MM polarimeter system with a fundus camera system, there are several principles to be followed during the optical design:

- Use as many off-the-shelf lenses as possible to save building time
- The annulus in the illumination pathway must conjugate to eye cornea
- The FOV should be approximately 30°
- The PSG conjugates to eye fundus, the PSA and FPA sensor
- Eye relief should be as big as possible

Both internal illumination design and external illumination design were examined for the possibility of PSG and PSA incorporation. Initially, we decided to carry out the optical design of SRIMMP with internal illumination, since it is easier to get a large eye relief with a shared objective lens. To check the feasibility of a potential SRIMMP design with internal illumination, a paraxial model of illumination pathway was created in Zemax, assuming a PSG location between the illumination source and the annulus. The 2D layout of the model is as shown in Figure. 3-2, for simplicity, the point source is not shown, which makes the PSG first surface in the model. The structure and dimensions of the model eye in all the optical designs of this work follow the Arizona eye model [4].

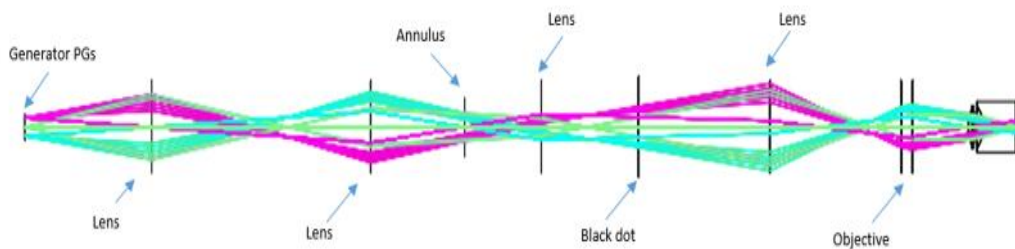


Figure. 3-2. Paraxial illumination pathway model with internal illumination in Zemax.

With all the conjugation relations satisfied, the annulus and the black dot get imaged onto the cornea and the first surface of objective lens, as depicted in Figure. 3-3. However, problem appeared at the retinal plane. Figure. 3-4 shows the system's transmission of a grid pattern from the PSG plane onto the retinal plane. Obscuration appears in the central field, which is intolerable. To solve the problem within the frame of internal illumination, we tried to alter the position of PSG plane in the illumination pathway, yet similar problems appeared. Soon we realized that, with the PSG and the black dot in the same optical space, the optical field of the PSG plane would always be affected by the black dot. This issue could be solved by adding an artificial pupil into the illumination pathway. However, since this would complicate the design, we finally decided to give up the internal illumination design and examined the external illumination design instead.

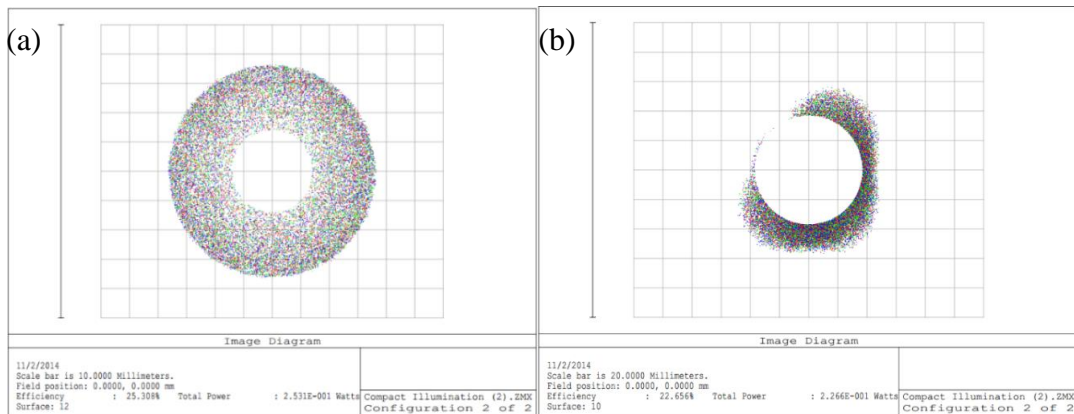


Figure. 3-3. Light pattern on a) cornea and b) the first surface of objective lens in the paraxial internal illumination design verification model.

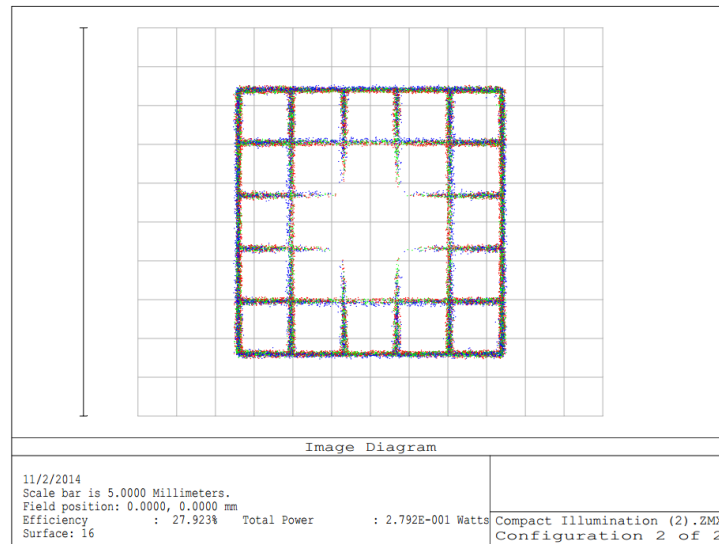


Figure. 3-4. Light pattern on retina with internal illumination, central blockage observed.

Like what was done for the internal illumination layout, before starting the actual design, a simplified model of illumination pathway was created in Zemax to verify the feasibility. As depicted in Figure. 3-5 and Figure. 3-6, a spider aperture was defined at the PSG plane as a target for pattern transmission verification between the PSG and the retina. The pattern is transferred successfully to the retina with minimal impairment, which means it is viable to place the PSG and the PSA in an external illumination configuration.

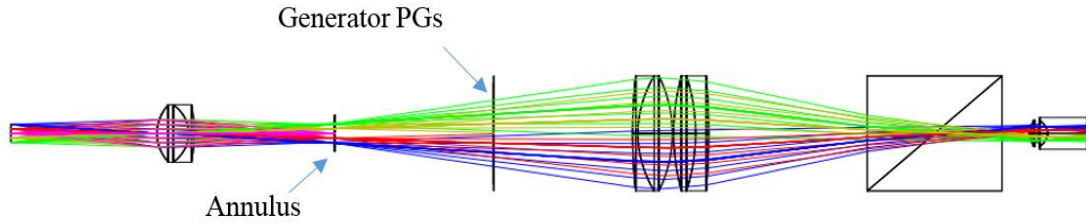


Figure. 3-5. Simplified model with external illumination in Zemax used to verify the viability of SRIMMP optical design.

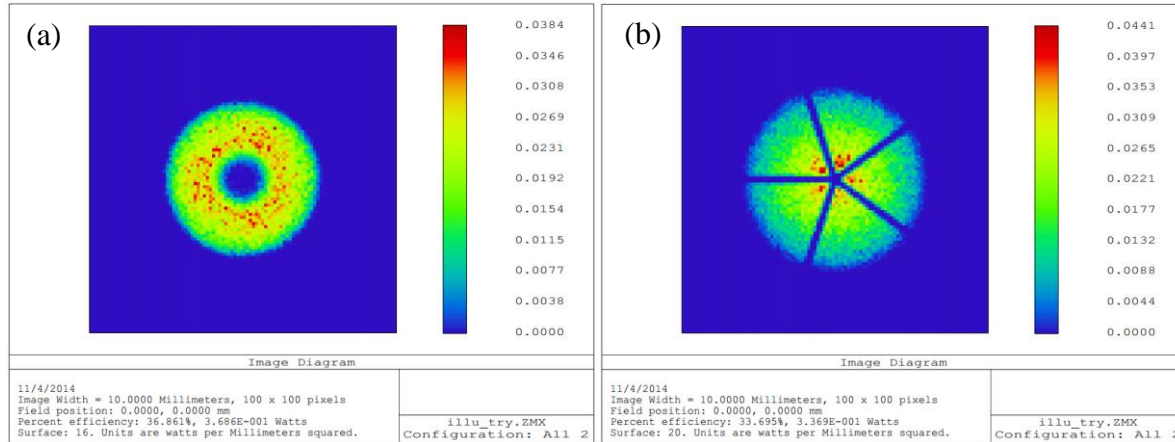
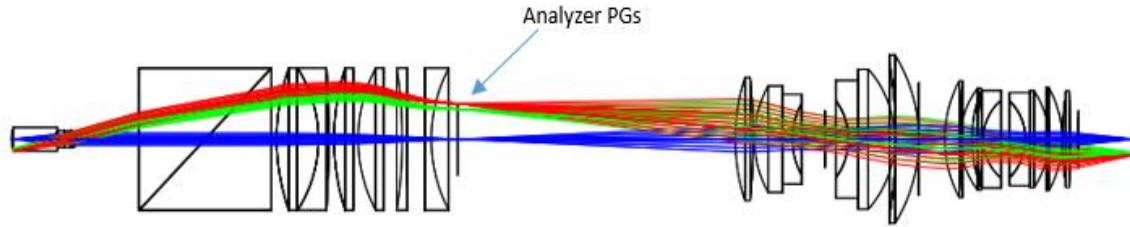


Figure. 3-6. Light pattern on a) cornea and b) eye fundus in the paraxial external illumination verification model. As can be seen, the annulus image projects onto the cornea and the aperture pattern defined on the PSG plane is imaged onto the retina.

A schematic of the SRIMMP optical design with external illumination is as depicted in Figure. 3-7. Comparing Figure. 3-7 to Figure. 3-1a, the objective lens in the imaging pathway and the imaging lens in the illumination pathway have to be re-designed to support conjugation relations among the PSG, the PSA and the eye fundus.

such as lens splitting, iterations of local/global optimization *etc.* Finally, all the optics in this design were replaced by off-the-shelf products without sacrificing too much optical performance.



(a)

Surf.Type	Comment	Radius	Thickness	Glass	Semi-Diameter	Conic	Pac 0 (unused)	Focal Length	OPF Mode	Pac 3 (unused)	Pac 4 (unused)	Pac 5 (unused)	Pac 6 (unused)	Pac 7 (unused)
0B2	Standard	retina	13.400	16.713	1.94,61.1	4.198	0.000							
1*	Standard	vitreous	5.224	3.787	1.42,51.9	3.000	-1.124							
2	Standard	lens	-12.000	2.970	1.74,61.3	3.000	-7.519							
3*	Standard	squene	-6.500	0.550	1.39,57.1	3.000	-0.250							
4*	Standard	cornea	-7.800	0.000	3.000	0.000	-0.250							
5	Paraxial		0.000		1.862			0.000	1					
6	Paraxial		25.000		1.862			0.000	1					
7*	Standard		Infinity	25.400	N-BK7	25.400	0.000							
8*	Tilted		25.400		N-BK7	25.400		0.000	1.000					
9*	Standard		Infinity	2.000		25.400	0.000							
10*	Standard	AC508-100-A	71.120	16.000	N-BAF10	25.400	0.000							
11*	Standard	Thorlabs	-44.170	4.000	SF10	25.400	0.000							
12*	Standard		-363.100	2.000		25.400	0.000							
13*	Standard	LAla17-A	72.300	2.000	BK7	25.400	0.000							
14*	Standard	Thorlabs	Infinity	2.000		25.400	0.000							
15*	Standard	LAla50-A	51.500	5.700	BK7	25.400	0.000							
16	Standard	Thorlabs	Infinity	7.166	V	17.718	0.000							
17*	Standard	015-0670-A55	-155.700	2.000	BK7	25.400	0.000							
18	Standard	Optosigma	Infinity	6.713		15.525	0.000							
19	Standard	KPCOTAR-1A	Infinity	2.500	BK7	14.041	0.000							
20*	Standard	Newport	51.680	10.000		25.400	0.000							
21	Hologram 1		Infinity	104.650	V	12.760	0.000	0.000	0.000	500.000	0.000	0.000	1.000E+006	0.653
22	Paraxial		60.000		0.000			100.000	1					
23*	Standard		67.148	6.858	SK16	22.000	0.000							
24*	Standard		-196.417	0.300		21.000	0.000							
25*	Standard		36.980	10.834	SK16	19.000	0.000							
26*	Standard		Infinity	3.777	FS	16.000	0.000							
27*	Standard		25.685	12.428		13.000	0.000							
28	Standard		Infinity	8.989		10.000	0.000							
29*	Standard		-22.270	3.777	FS	14.000	0.000							
30*	Standard		Infinity	14.000	SK16	21.000	0.000							
31*	Standard		-35.951	0.500		25.000	0.000							
32*	Standard		-152.522	5.747	SK2	28.000	0.000							
33*	Standard		-54.153	0.000		30.000	0.000							
34*	Standard		Infinity	10.000		20.000	0.000							
35	Paraxial		49.999		0.000			50.000	1					
36*	Standard		41.745	5.907	TAF1	20.833	0.000							
37*	Standard		274.475	0.145		20.564	0.000							
38*	Standard		28.548	4.414	TAF1	18.214	0.000							
39*	Standard		44.963	3.916		17.477	0.000							
40*	Standard		83.167	2.421	F1	17.403	0.000							
41*	Standard		17.612	6.750		15.897	0.000							
42	Standard		Infinity	9.424		13.894	0.000							

(b)

Figure. 3-8. a) Layout of the imaging pathway in Zemax sequential mode; b) lens prescription of the imaging pathway.

The FFT MTF curves of light from the center, the middle and the periphery of the FOV, as indications of system's optical performance, are depicted in Figure. 3-9. The dominant Seidel aberration in the system is distortion. It could be corrected by applying pre-distortion to the PGs. The procedure is: pre-warp the PGs in the PSG to make the fringes projected onto the fundus straight, then pre-warp the PGs in the PSA to make them have the same extent of distortion as the fundus image on the PSA surface. At this point, the fringes and the retinal image have same extent of distortion and can be corrected together in post-processing. To calculate the needed pre-

distortion, a Matlab code was created. The distortion data were pulled from the “Grid Distortion” analysis in Zemax and were used in fitting the polynomial function that describes 2D distortion. From the output of the code, it can be seen that the distortion in the imaging pathway is much larger than that in the illumination pathway. The supposed pre-warp for the PSG is small enough to be neglected, while the PSA might need pre-warping. However, due to difficulties in manufacturing, we decided to order straight patterned PGs for this experiment. Except the distortion, other Seidel aberrations are very small and can be ignored.

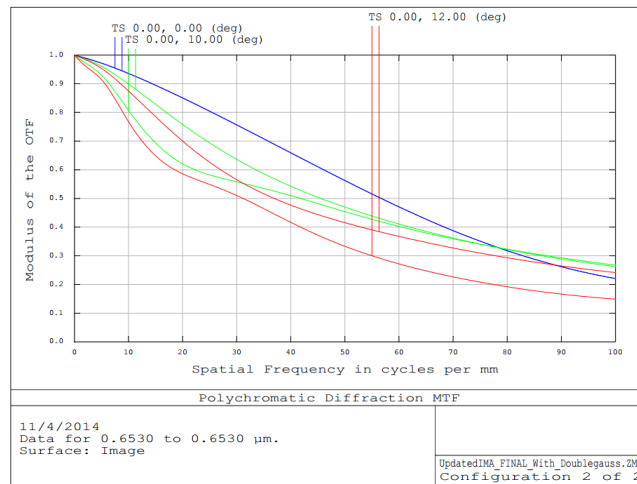
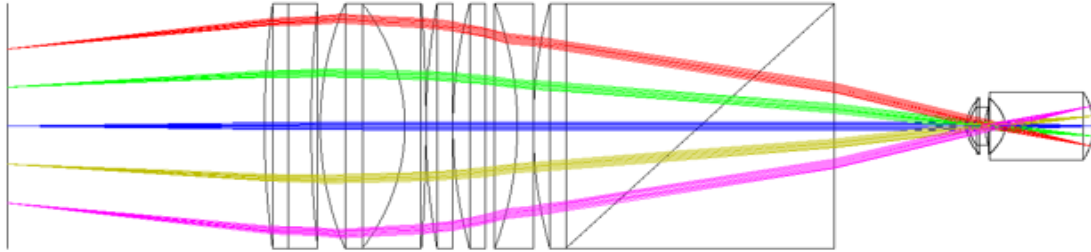


Figure. 3-9. MTF curves of the imaging pathway with 4 mm pupil size.

The illumination pathway was also designed using the sequential mode of Zemax. The key in illumination design is the lens set between the PSG and the eye. After the design of these lenses are nailed, the annulus can be simply placed at the conjugate position of the cornea, since the optical performance between the annulus and the cornea does not need to be very good. A condenser lens is added right next to the illumination source for collimation. The Zemax sequential layout of the design and its corresponding lens prescription are as presented in Figure. 3-10.



(a)

Surf.Type	Comment	Radius	Thickness	Class	Semi-Diameter	Conic	Par 0 (unused)	Par 1 (unused)	Par 2 (unused)	Par 3 (unused)	Par 4 (unused)	Par 5 (unused)	Par 6 (unused)	Par 7 (unused)
1*	Standard	Infinity	46.604		25.400	0.000								
1*	Standard	206.720	4.566	BK7	25.400	0.000								
2*	Standard	Infinity	0.000		25.400	0.000								
3*	Standard	Infinity	4.251	BK7	25.400	0.000								
4*	Standard	258.400	1.731		25.400	0.000								
5*	Standard	ACS08-100-A	71.120	16.000	N-BK7	25.400	0.000							
6*	Standard	Thorlabs	-44.170	4.000	SF10	25.400	0.000							
7*	Standard	-363.100	0.000		25.400	0.000								
8*	Standard	LA1417-A	155.040	5.095	BK7	25.400	0.000							
9*	Standard	Thorlabs	Infinity	0.000	25.400	0.000								
10*	Standard	LA1050-A	103.360	6.170	BK7	25.400	0.000							
11*	Standard	Thorlabs	Infinity	6.000	25.400	0.000								
12*	Standard	-77.850	3.000	BK7	25.400	0.000								
13*	Standard	Infinity	0.000		25.400	0.000								
14*	Standard	103.360	6.170	N-BK7	25.400	0.000								
15*	Standard	Infinity	0.000		25.400	0.000								
16*	Standard	Infinity	25.400	N-BK7	25.400	0.000								
17*	Tilted		25.400	N-BK7	25.400	0.000		0.000	1.000					
18*	Standard	Infinity	25.000		25.400	0.000								
19*	Standard	cornea	7.800	0.550	1.38,57.1	5.869	0.000							
20*	Standard	aqueous	6.500	2.970	1.34,61.3	4.000	0.000							
*	Standard		12.000	3.767	1.42,51.9	4.000	0.000							
22*	Standard		-5.220	16.713	1.34,61.1	5.851	0.000							
*	Standard	fundus	-13.700	-	7.000	0.000								

(b)

Figure. 3-10. a) Layout of illumination pathway design from the PSG to the eye fundus, all the optical components are off-the-shelf, b) Zemax lens prescription of the illumination pathway design from the PSG plane to the eye fundus.

The corresponding FFT MTF curves are as shown in Figure. 3-11. It can be seen from the MTF curves that, at 50 cycles/mm, the very edge of the field has a >0.4 MTF value, which indicates satisfactory optical performance. The distance between the eye and the last surface of the beam splitter was set to be 25 mm assuming the use of a beamsplitter made from N-BK7 glass (refractive index 1.51). A homogeneous round source was placed at the beginning of the sequential model to simulate a homogeneous illumination, which could not be modeled in the sequential mode of Zemax. The illuminated area on the fundus can be as large as 4.6 mm in radius, which corresponds to 26.5° FOV, the illumination on the fundus shows good homogeneity across the whole area. The

AC254-030-A achromatic lens in the optical design was later replaced by a pair of LA1401-A plano-convex lenses due to an availability issue.

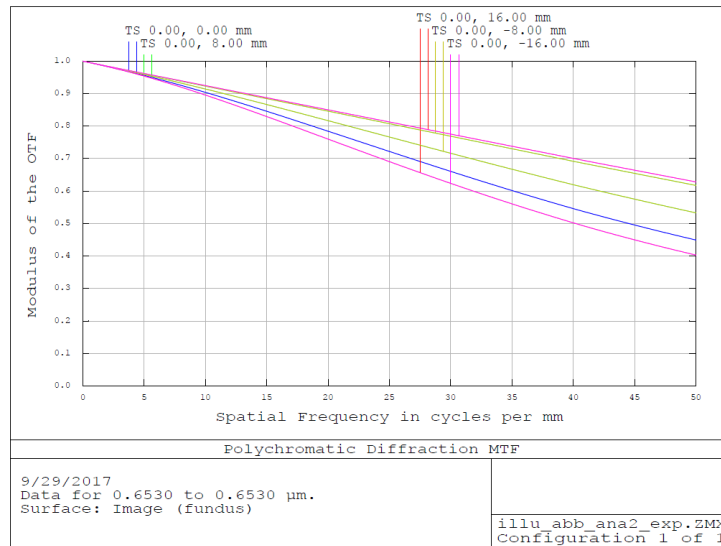


Figure. 3-11. MTF curves of the illumination pathway from the PSG plane to the eye fundus.

The tolerance analysis for the illumination pathway and the imaging pathway was also carried out in Zemax sequential mode, the results have shown that, the system's resistance to potential errors and misalignments during assembly is satisfactory. A default merit function and Monte Carlo method were used for the analysis.

The illumination pathway design and the imaging pathway design in sequential mode of Zemax were then combined and transferred into a single non-sequential model for ray-tracing simulations, as depicted in Figure. 3-12. In the model, three detectors are placed at the cornea, the FPA, and the eye fundus, to monitor the illumination distribution at these locations. 1,000,000 monochromatic rays at 660 nm were traced with a total power of 1 Watt, the light fields recorded by the detectors are as shown in Figure. 3-13. As can be seen, the shapes of light fields captured by the three detectors are as expected. The illumination pattern at the retina is homogeneous and has a 5.2 mm radius, which is larger than the expected value in the sequential mode. This is probably caused by light scattering and helps to enlarge the overall field of view (FOV).

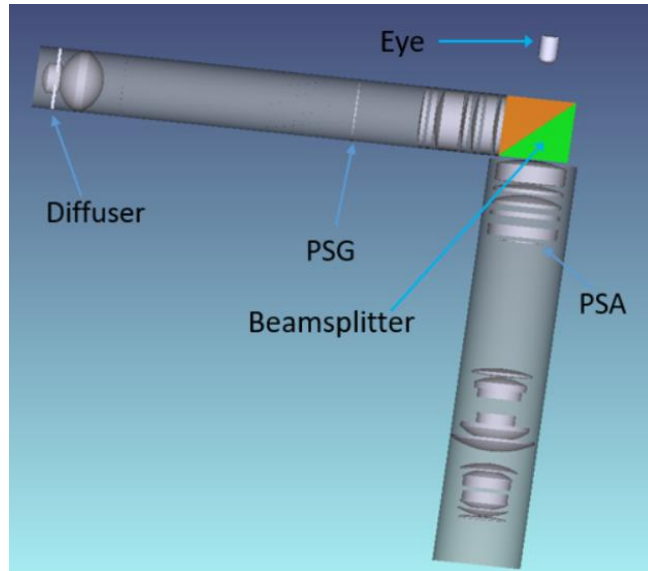


Figure. 3-12. Layout of the SRIMMP optical design in non-sequential mode of Zemax.

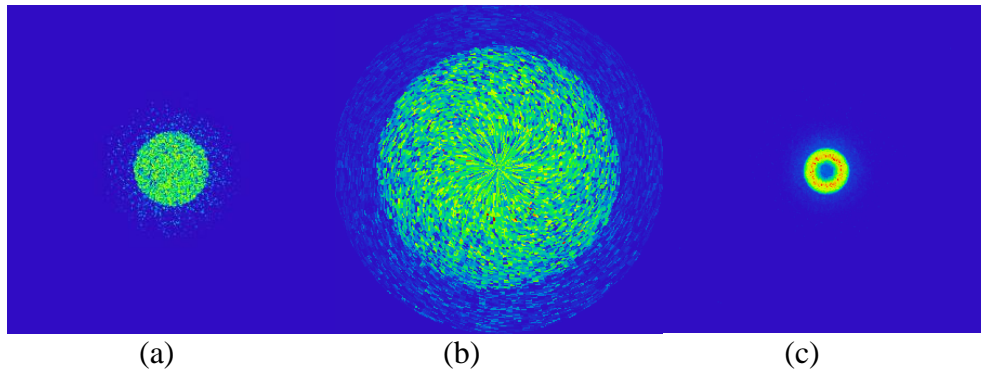
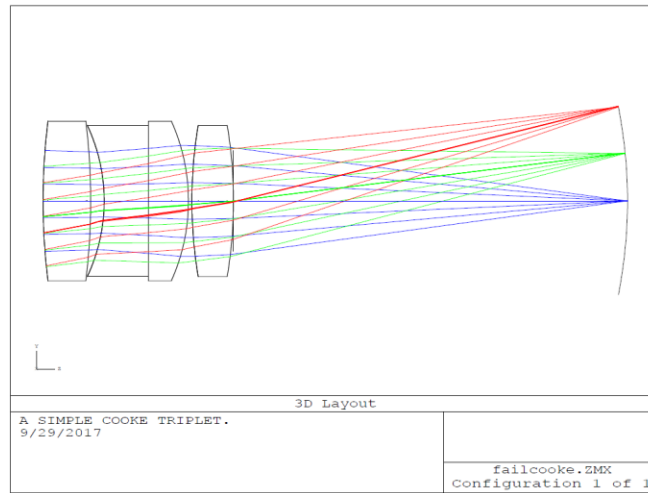


Figure. 3-13. Light distribution on the detectors at a) FPA; b) fundus; and c) cornea resulted from the ray-tracing simulation.

A ray-tracing simulation without eye fundus in the non-sequential model was also performed to quantify the influence of corneal reflection. In this simulation, the light received at the FPA is only from the corneal reflection and stray light within the optical system. The simulation result shows that the total power received was only about 1/12 as in the previous simulation with the fundus, which means that the light arrived at the FPA was mainly from the eye fundus. The overall cost of optics in this optical design is around \$2,000.

3.1.2 Optical design of model eye

To perform system alignment, calibration and validation, a model eye is needed. The optical design of the model eye was also carried out in Zemax sequential mode. Figure. 3-14 illustrates the optical design layout of the model eye and its corresponding lens prescription.



(a)

Surf#	Type	Comment	Radius	Thickness	Glass	Semi-Diameter	Conic	Par 0 (unused)	Par 1 (unused)	Par 2 (unused)	Par 3 (unused)	Par 4 (unused)	Par 5 (unused)
OBJ	Standard		Infinity	Infinity		Infinity	0.000						
1*	Standard	newport	51.234	3.790	BK7	6.350	U	0.000					
2*	Standard	KMX037AR.14	-51.234	1.070		6.350	U	0.000					
3*	Standard	edmund	-14.120	3.500	SF11	6.000	U	0.000					
4*	Standard	48-343	Infinity	0.000		6.000	U	0.000					
5*	Standard	Thorlabs	Infinity	3.200	BK7	6.350	U	0.000					
6*	Standard	LAI289-A	-15.500	0.280		6.350	U	0.000					
7*	Standard	Edmund	36.650	3.300	N-BK7	6.000	U	0.000					
8*	Standard	45-876	-36.650	0.000		6.000	U	0.000					
STO	Standard	Newport	Infinity	31.338	V	4.000	U	0.000					
10*	Standard	KPC043AR.14	-12.920	2.500	BK7	12.700	U	0.000					
11*	Standard		Infinity	0.000		12.700	U	0.000					
IMA	Standard		-37.300	-		7.449	-4.000						

(b)

Figure. 3-14. a) Layout of the model eye design in Zemax sequential mode; b) the corresponding lens prescription.

Figure. 3-15 depicts the FFT MTF curves of the model eye design. Due to the time limit of the project, the design was restricted to use off-the-shelf ½-inch optics only, which made the choices very limited. As a result, the theoretical optical performance of the design is average, however, later in practice we have found that the performance of the model eye is sufficient for its purpose.



Figure. 3-15. FFT MTF curves of the Model eye design in Zemax.

3.2 Opto-mechanical designs

3.2.1 Opto-mechanical design of SRIMMP

To transfer the optical design of SRIMMP into an instrumental design, opto-mechanical design is needed. Similar to the optical designs, in the opto-mechanical design, we aimed to use as few customized parts as possible. Autodesk Inventor was used as the computer-aided design (CAD) software for this task. Most of the CAD models of off-the-shelf parts were downloaded from manufacturers' websites and the rest were built according to the dimensions found online. The opto-mechanical design of SRIMMP adopts a 60-mm cage system to mount the optics in the optical design. The only customized part in the cage system is the case for the 2-inch cubic beamsplitter, which is also the connector between the illumination pathway and the imaging pathway. Both pathways have lenses placed very close to or even nearly touching the cube beamsplitter, a cage mount that supports this kind of connections could not be found from the market. Thus, the beamsplitter case was modeled in Autodesk Inventor, the 3D layout of the case can be seen in Figure. 3-16. The case body supports zero-distance connection between the beamsplitter cube and Thorlabs 2-inch lens tube. The optics would be placed into the lens tubes

which have a close connection with the beamsplitter cube. One side of the beamsplitter case remains open, which is the side towards patient's eye. A device-eye interface could be added here to help exclude the influence of ambient light. To avoid contact between opto-mechanical parts and patient's forehead, the LCP09 cage plate was cut off 10mm on the side of the towards patient's face. The lid of the beamsplitter case can be taken off the case body, to allow easier insertion and removal of the beamsplitter cube.

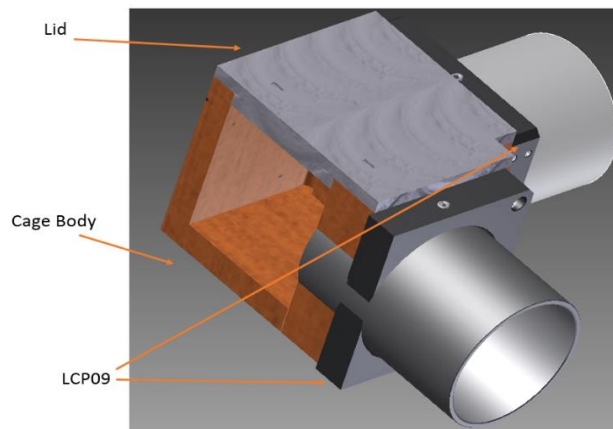


Figure. 3-16. Opto-mechanical CAD design of the beamsplitter case as part of the 60-mm cage system.

To verify the dimensions of the beamsplitter case design and its compatibility with other parts of the system, a plastic model was made using 3D printing technique prior to the actual manufacture of the metal beamsplitter case. The 3D-printed model fitted with other parts of the system well. An aluminum beamsplitter case was then made with the same dimension parameters. The metal beamsplitter case can provide more support to the system than the plastic model. The 3D printed model and the aluminum beamsplitter case are as depicted in Figure. 3-17.

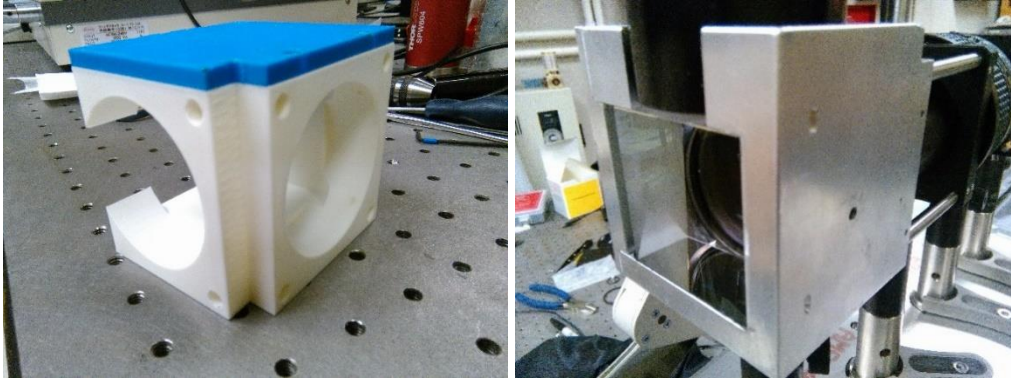


Figure. 3-17. Left: 3D printed prototype of the beamsplitter case; right: the aluminum beamsplitter case.

It was supposed that, during the development and test of the device, a lot of re-alignments are needed. So, it is better that the position of the PSG can still be adjustable after the whole device is assembled. In the opto-mechanical design this is realized by mounting PSG into a Thorlabs SM2L20C slotted lens tube. With an opening of 21.6 mm, the slotted lens tube allows small adjustments of PSG position. The position of the slotted lens tube in the SRIMPP system is as illustrated in Figure. 3-18.

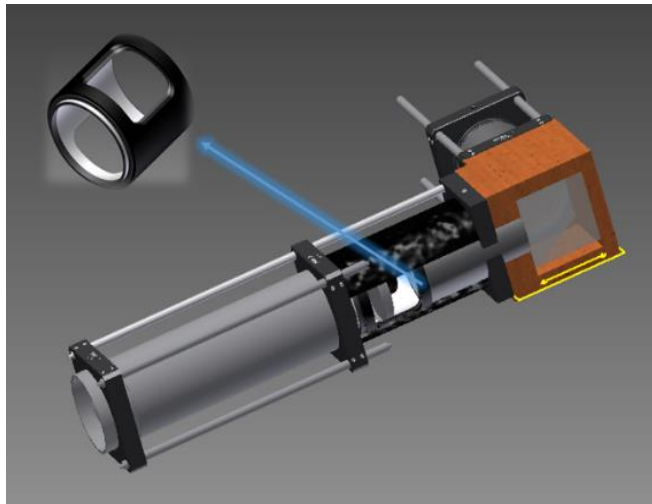


Figure. 3-18. Position of the slotted lens tube containing the PSG in the SRIMPP opto-mechanical design.

The opto-mechanical design model of the SRIMPP device is as depicted in Figure. 3-19, the corresponding part list is in Table 3-1.

Table 3-1. Parts list of the optics and opto-mechanical components used in the SRIMMP design, including the part number (PN), the part name as well as their associated model provided by the vendor, and the required quantities.

Part Number	Part Name	Vendor	Model	Quantity
1A	Ø2" N-BK7 Plano-Convex Lens	Thorlabs	LA1401A	1
1B	Ø2" N-BK7 Plano-Convex Lens	Thorlabs	LA1401A	1
2	Retaining Ring	Thorlabs	SM2RR	29
3	60mm Cage Plate	Thorlabs	LCP09	3
4	Annulus	-----	-----	1
5	Extension Tube	Thorlabs	SM2E60	1
6	SM2 Coupler with External Threads	Thorlabs	SM2T2	2
7	PSG	-----		1
8	SM2 Slotted Lens Tube	Thorlabs	SM2L20C	1
9	SM2-Lens Tube	Thorlabs	SM2M30	1
10	N-BK7 Plano-Convex Lens	Thorlabs	LA1725A	1
11	Ø2" N-BK7 Achromatic Doublet	Thorlabs	AC508-100-A	2
13	Ø2" N-BK7 Plano-Convex Lens	Thorlabs	LA1256A	1
14	Ø2" N-BK7 Plano-Convex Lens	Thorlabs	LA1979A	2
15	BK7 Plano-Concave Lens	Optosigma	015-0640	1
16	Beam Splitter	Esco Optics	-----	1
17	Beam Splitter Cage	-----		1
19	N-BK7 Plano-Convex Lens	Thorlabs	LA1417A	1
20	N-BK7 Plano-Convex Lens	Thorlabs	LA1050A	1
21	BK7 Plano-Concave Lens	Optosigma	015-067-A55	1
22	N-BK7 Plano-Concave Lens	Newport	KPC076AR	1
23	Cage Rod	Thorlabs	ER3&ER6	6

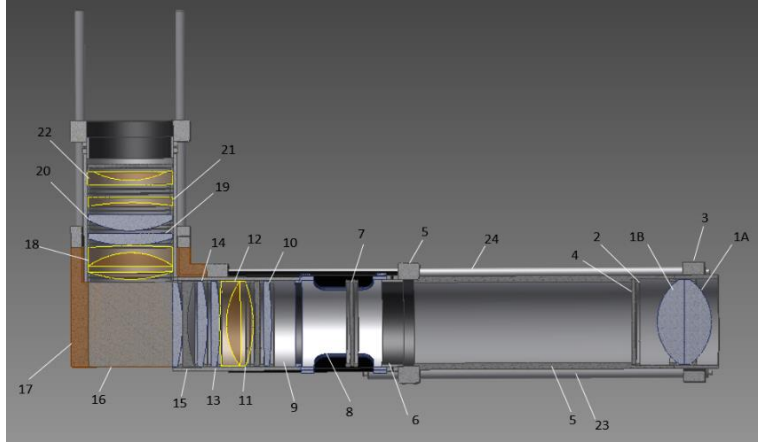


Figure. 3-19. The opto-mechanical CAD design model of the SRIMMP system. The details of the labeled parts are shown in Table 4-1.

3.2.2 Opto-mechanical design of model eye

The opto-mechanical design of model eye was also done in Autodesk Inventor. A curved mirror is placed at the back of the model eye as dummy retina, to induce more signal reflection. As can be seen from the 3D layout in Figure. 3-20, a distance adjustable mount is used to house the dummy retina, which makes the distance between the "retina" and the "eye lens" adjustable. This feature, along with the adjustable PSG position, helps to simplify the re-alignment of the system.

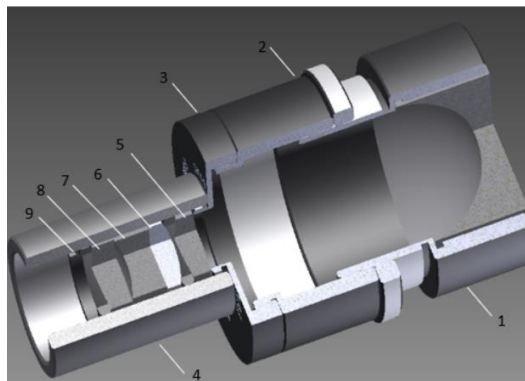


Figure. 3-20. The 3D model of the model eye assembly in Autodesk Inventor.

Lenses, mirror and opto-mechanical parts were purchased according to the optical design and opto-mechanical design of the model eye. The part list is as shown in Table 3-2.

Table 3-2. Parts list of the optics and opto-mechanical components used in the model eye design, including the part number (PN), the part name as well as their associated model provided by the vendor, and the required quantities.

Part Number	Part Name	Vendor	Model	Quantity
1	Ø1" Adjustable Lens Tube	Thorlabs	SM1V05	1
2	Ø1" Lens Tube	Thorlabs	SM1L05	1
3	Thread Adapter	Thorlabs	SM1A1	1
4	Ø0.5" Lens Tube	Thorlabs	SM05M10	1
5	Ø0.5" N-BK7 Plano-convex Lens	Thorlabs	LA1289-A	1
6	Ø0.5" N-BK7 Bi-convex Lens	Newport	KBX037AR.14	1
7	Ø12mm N-SF11 Plano-concave Lens	Edmund	#48-343	1
8	Ø12mm N-BK7 Bi-convex Lens	Edmund	#45-876	1
9	Retaining Ring	Thorlabs	SM05RR	2

3.3 Choice of illumination source

In the SRIMMP system, two major requirements need to be considered when choosing illumination source:

- The wavelength has strong response from the retina
- The intensity of the source is safe for human eye

To satisfy both requirements, we chose Thorlabs M660L3 660 nm deep red mounted LED, with a maximum current of 1.2 A and typical power output of 1000 mW. To ensure that the illumination power enters the eye does not exceed the limit and cause hazard, the prototype of SRIMMP was built on an optical table to go through a radiometry test. In the test, a Thorlabs S14C integrating sphere photodiode power sensor was placed at the position of eye cornea, to capture the illumination power enters subject's eye. The sensor was connected to a Thorlabs PM100D compact power and energy meter console, after wavelength correction and background subtraction, the result could be read out from the screen of the console. When the output power of the LED

was on maximum, the average power received by the photodiode of three individual tests was 3.34 ± 0.1 mW.

According to the ICNIRP guidelines [6], three types of visual damage can be caused by sources in visible and infrared range: thermal injury of retina (380-1400 nm), photochemical injury of retina (300-550 nm), and near-infrared thermal injury of crystalline lens (800-3000 nm). Since the wavelength of the chosen source is 660 nm, the only possible damage to the eye is the thermal injury of retina. In 2007, François C. Delori *et al.* derived a concise formulation of the ANSI-2000 ocular safety standards to make them more applicable to typical ophthalmic devices [7]. In this new formulation, the safety limits are evaluated in the form of radiant power (Watts) entering the pupil of the eye. Under the new formulation, the thermal and photoacoustic maximum permissible radiant power ($MP\Phi$) entering through pupil can be expressed as follow, when the illumination duration is larger than 0.07s,

$$MP\Phi = 6.93 \times 10^{-4} C_T C_E P^{-1} t^{-0.25} \quad (1)$$

where $MP\Phi$ is the maximum permissible radiant power entering eye pupil, CT is a function of wavelength, when $\lambda=660$ nm, $CT=1$, CE is a function of α , which is the visual angle, and the unit for α is mrad. In this case, $\alpha \approx 27^\circ = 471$ mrad, $CE = 1496.6$; P is called pupil function, which depends on both α and λ , $P = 100.0074 \times (700 - \lambda) = 1.977$; t is the duration of illumination.

Assuming the average duration of test before the fundus image capture is 60 seconds, then

$$MP\Phi = 6.93 \times 10^{-4} \times 1 \times 1496.6 \times 1.977^{-1} \times 60^{-0.25} = 188.5 \text{ mW} \quad (2)$$

As mentioned earlier in this section, in our system, the maximum radiant power into the eye is about 3.46 mW, about 50 times smaller than the limit specified above in Eq. 2. It is unlikely for the illumination in our SRIMMP system to cause visual hazards to human eye. In addition, the system under test was assembled without the PSG and the PSA, considering the PGs would also

cause a little loss in optical power, the actual radiant power entering patient's eye would be even smaller. In conclusion, the choice of illumination source is safe for human eyes.

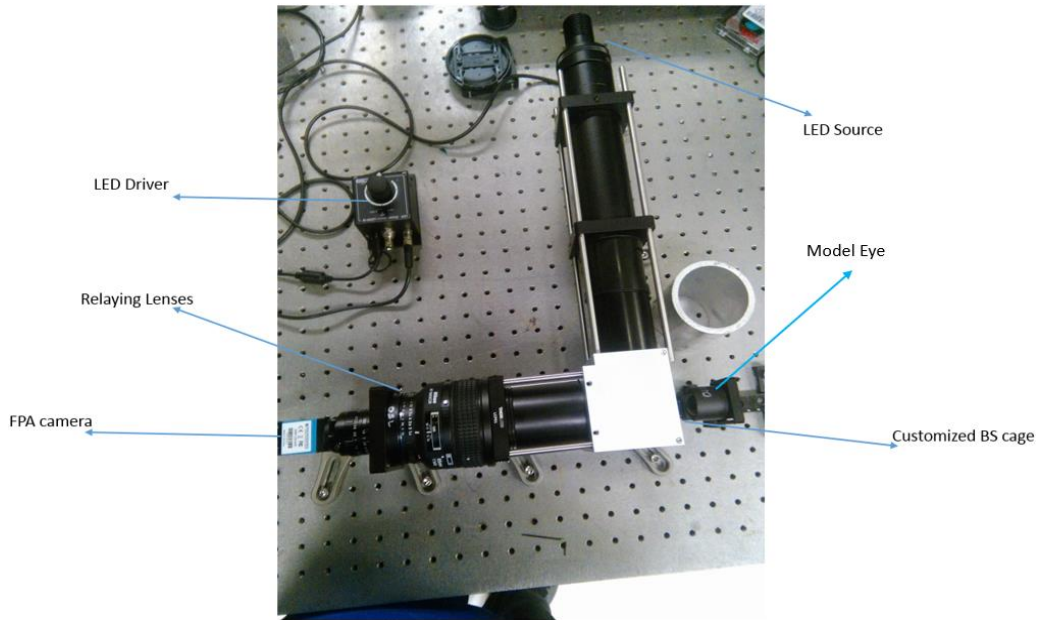


Figure. 3-21. The initial SRIMMP experimental setup on an optical table for radiometry tests. The model eye would be replaced by a photodetector during the tests.

3.4 Choice of polarization gratings

In the SRIMMP device, the PSG consists of a LP, two orthogonally oriented PGs and a quarter wave plate (QWP) in between them. The PSA has the same structure, with a smaller grating period of the PGs. The choice of PG periods is closely related to the system's configuration. The PSG and the PSA take an $x/y/x/y$ arrangement, which means in the PSG, the period of the first PG is along x direction, and that of the second PG is along y direction. For the PSA, the arrangement for the PGs is the same, with smaller PG periods. The period of PSG defines the spatial resolution of reconstructed MM. In the optical design of SRIMMP, the magnification from PSG to retina is about 0.32, so $3500 \mu\text{m}$ PSG period corresponds to $1 \text{ mm} \times 1 \text{ mm}$ area on retina. Within each of these areas, all the input polarization states provided by PSG present in a periodic fashion, and the MM values are considered to be constant. Considering the overall illuminated area on the retina is

circular with a diameter of 15 mm, there would be about 176 independent MMs used to describe the 2D MM of the ROI. The PSA provides carrier frequencies for the PSG modulation, its period should be much smaller than that of PSG such that the PSG modulations at different Fourier domain channels do not entangle. It should be noted that this arrangement is different from the recommended optimal arrangement by Alein and Tyo [8]. In their paper, an $x/x/y/y$ arrangement is recommended to maximize the signal-to-noise ratio in all MM components. However, the $x/x/y/y$ arrangement intrinsically assumes an algebraical MM reconstruction strategy, to apply a reference-beam-technique-based MM reconstruction strategy on the $x/x/y/y$ arrangement would be difficult. Moreover, in our SRIMMP system, to use an $x/x/y/y$ arrangement requires higher spatial frequencies from the generator and the retina, which means greater attenuation due to the MTF limit of the intermediate lenses. In addition, since we initially chose to use a 4:1 grating period ratio instead of the 2:1 ratio specified in [8], the frequency channel would locate further away from each other. The channel components detangling would automatically take place. Such that in our system, $x/x/y/y$ arrangement is not necessary for simplification of channel contents. According to these reasons, $x/y/x/y$ arrangement was chosen to be applied into the SRIMMP system.

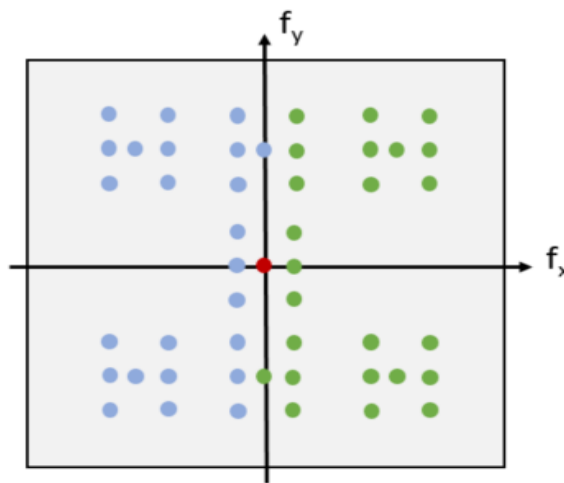
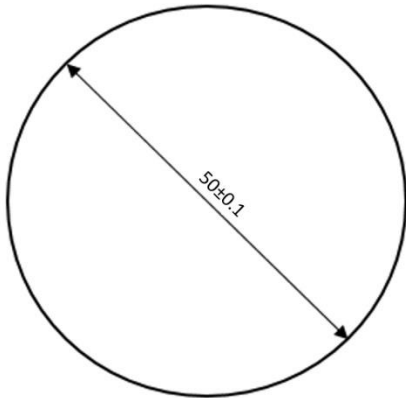


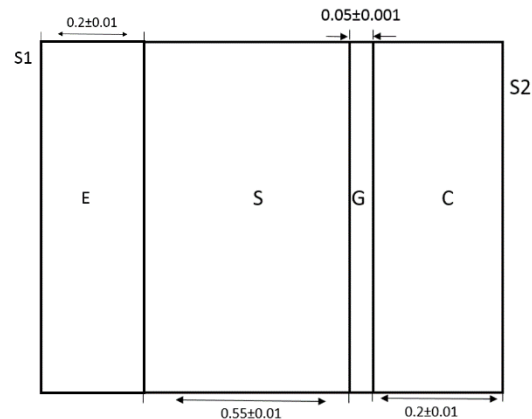
Figure. 3-22. All the ideal channels in the Fourier domain of a channeled image obtained from the SRIMM with $x/y/x/y$ arrangement. The ratio between the PG periods of the PSG and the PSA is 4:1. f_x and f_y axes in Fourier domain correspond to x and y axes in spatial domain.

Based upon the PG configuration discussed above, the specifications of PGs can be selected. After a series of tests upon human skin and retina, the PG period ratio between the PSG and the PSA was enlarged to 14:1, to increase the visibility of polarization fringes on retina. The PGs used were fabricated in the phase photonics laboratory of North Carolina State University. After delivery to our lab, each PG was optical bonded to thin glass windows on both sides, to protect the grating surface. The coated PGs were then optical bonded into pairs, along with QWPs, LPs to form the PSG and the PSA. The configurations of PGs in the PSG and the PSA are as shown in the following two pages.

Polarization Grating 1&2 in PSG
front view



side view



All length dimensions are in mm. Angles are in degrees. **Diagram is not to scale.**

Dimensional specifications:

1. One the side view of the polarization grating, S stands for substrate, G stands for grating surface, E stands for endcap and C stands for cover glass. All the three components should be circular with diameter of 50 ± 0.1 mm.
2. The nominal thickness is 0.55 mm for substrate S, 0.05 mm for grating surface G and 0.2 mm for cover glass C and endcap E, tolerances as depicted above.

General specifications:

1. Surface S1 should be AR coated. The transmitted wavefront should be 1/4 wave at 633 nm, the surface quality should be 40-20 scratch-dig.
2. The minimum clear aperture of the polarization grating would need to be at least 90%.
3. All surfaces are Plano.
4. The spectral operation range of the polarization grating should be 620 nm-700 nm.
5. Zeroth order leakage of this polarization grating should be less than 0.5%.

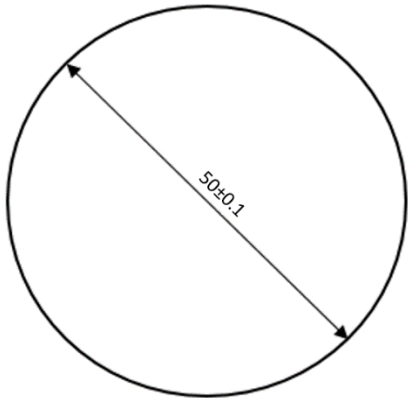
Substrate Material: N-BK7 glass

Cover Glass Material: N-BK7 glass

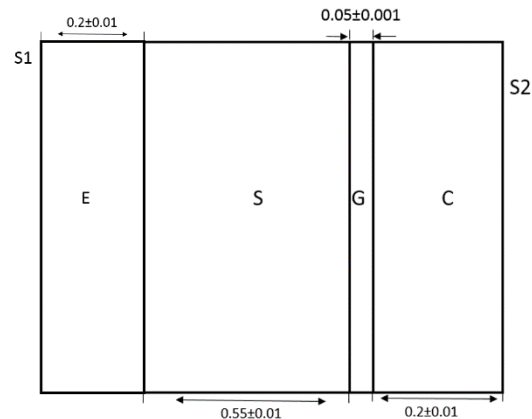
Endcap Material: N-BK7 glass

Grating Period: 3500 μ m

Polarization Grating 3&4 in PSA
front view



side view



All length dimensions are in mm. Angles are in degrees. **Diagram is not to scale.**

Dimensional specifications:

1. One the side view of the polarization grating, S stands for substrate, G stands for grating surface, E stands for endcap and C stands for cover glass. All the three components should be circular with diameter of 50 ± 0.1 mm.
2. The nominal thickness is 0.55 mm for substrate S, 0.05 mm for grating surface G and 0.2 mm for cover glass C and endcap E, tolerances as depicted above.

General specifications:

1. Surface S1 should be AR coated. The transmitted wavefront should be 1/4 wave at 633 nm, the surface quality should be 40-20 scratch-dig.
2. The minimum clear aperture of the polarization grating would need to be at least 90%.
3. All surfaces are Plano.
4. The spectral operation range of the polarization grating should be 620 nm-700 nm.
5. Zeroth order leakage of this polarization grating should be less than 0.5%.

Substrate Material: N-BK7 glass

Cover Glass Material: N-BK7 glass

Endcap Material: N-BK7 glass

Grating Period: 250.8 μm

3.5 Assembly of the SRIMMP device

After the radiometry tests, the device was transplanted onto the xyz translational stage of an old Kowa Fx50R fundus camera to give it the ability of 5-dimensional movement (xyz, azimuth and inclination). The chin-rest of the old fundus camera was also cannibalized and used in the new system after re-enforcement. A newly made forehead-rest was used along with the chin-rest to fix the position of subject's face. The initial setup of the SRIMMP system on the translational stage is as presented in the photo below.

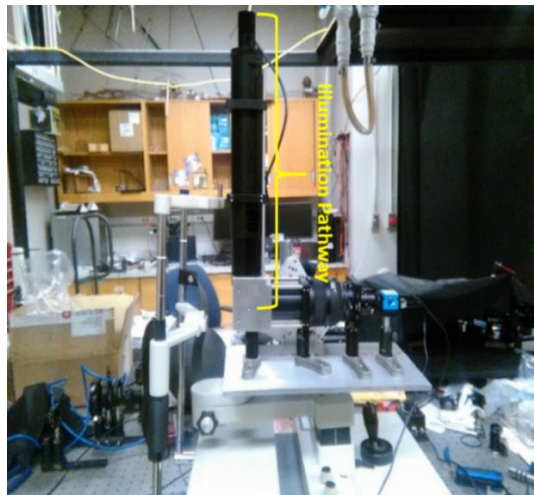


Figure. 3-23. The initial system setup of SRIMMP on the translational stage cannibalized from an old Kowa FX50R fundus camera. The illumination pathway is labeled by the yellow curly bracket.

As depicted in Figure. 3-23, the illumination pathway was vertically mounted on the top of the beamsplitter cage in the initial system setup. It was supported by two Thorlabs cage assembly rods, each with 6 mm diameter cross-section. In practice, it was found that the limited support greatly limited the stability of the illumination pathway. When the translational stage was in motion, the illumination pathway wiggled a lot. Because the layout put most of the device's weight on the front-end of the baseplate, it also has a negative effect on the stability of the SRIMMP device in the long run. To fix the problem and increase the stability of the system in the long run, the illumination pathway was later folded with an elliptical mirror in the middle of the

optical path. With the folded optical path, the first half of the illumination pathway is connected to the cage rods of the imaging pathway by two Thorlabs clip-on cage plates, increasing the number of supporting points from two to four. The center of gravity in the new layout lies in the middle of the baseplate. As a result, the system is more stable when in motion. In addition, in the new layout the PSG plane locates out of lens tube, which further simplifies the re-alignment operations. To implement this modification, some additional opto-mechanical components were purchased, including 2-inch lens tubes and 2-inch right-angle kinematic mirror mount, 2-inch silver elliptical mirror and two snap-on 60mm cage mounting brackets. The new setup of the system is as depicted in Figure. 3-24.

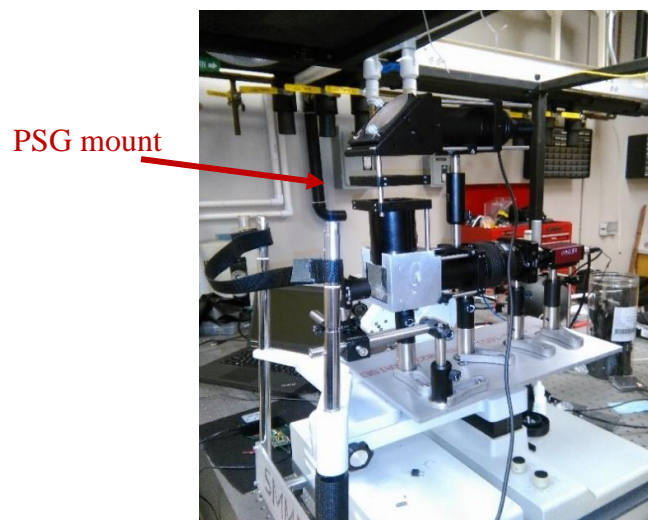


Figure. 3-24. The system setup of SRIMMP after illumination pathway modification. Note that the PSG is out of the lens tube.

A motor-driven rotational plate, along with corresponding motor, sensor, and circuits were also incorporated into the SRIMMP system, the function of them would be discussed later in this dissertation. The final assembly of the SRIMMP device is as depicted in Figure. 3-25.

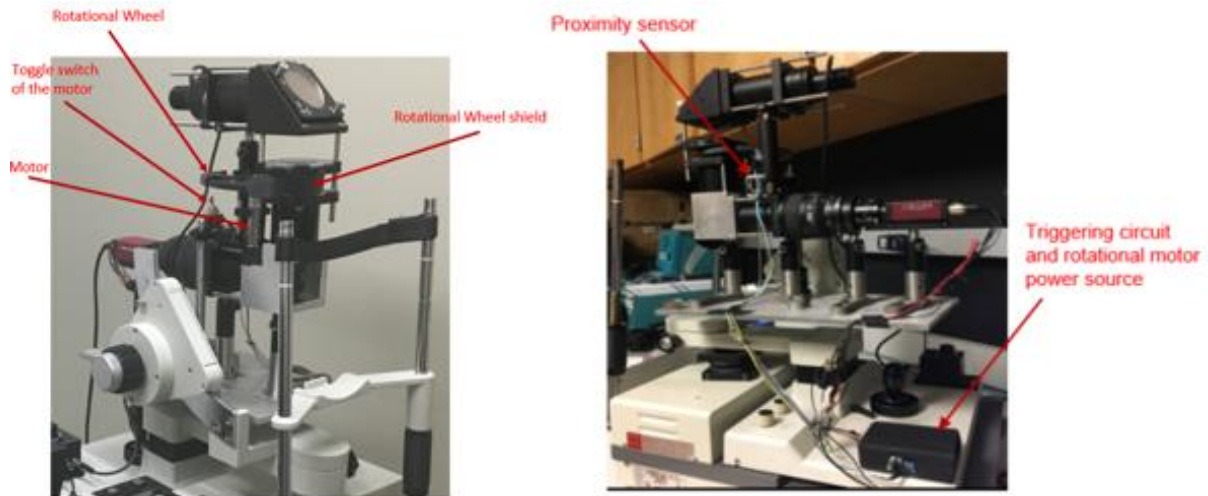


Figure. 3-25. The updated fundus camera hardware with the motor-driven rotational wheel and corresponding motor, sensor, and circuits incorporated.

The plastic electronic box that contains the control circuits, the joystick that controls the movement of the translational stage, and the current controller which controls the illumination level are placed together at the front panel of the fundus camera body, for the ease of operation during device tests.

References

- [1] Tran, K., Mendel, T. A., Holbrook, K. L., & Yates, P. A. (2012). Construction of an inexpensive, hand-held fundus camera through modification of a consumer “point-and-shoot” camera. *Investigative ophthalmology & visual science*, 53(12), 7600-7607.
- [2] Wikipedia User: Group2cla. (2015, September 21). Fundus photography. Retrieved from https://en.wikipedia.org/wiki/Fundus_photography.
- [3] DeHoog, E., & Schwiegerling, J. (2009). Fundus camera systems: a comparative analysis. *Applied optics*, 48(2), 221-228.
- [4] Schwiegerling, J. (2004, November). Field guide to visual and ophthalmic optics. SPIE.
- [5] Wang, Y., Kudenov, M., Kashani, A., Schwiegerling, J., & Escuti, M. (2015, September). Snapshot retinal imaging Mueller matrix polarimeter. In *Polarization Science and Remote Sensing VII* (Vol. 9613, p. 96130A). International Society for Optics and Photonics.
- [6] Protection, R. (1997). Guidelines on Limits of Exposure for Broad-band Incoherent Optical Radiation (0.38 to 3 μm). *Health Phys*, 73(3), 539-597.
- [7] Delori, F. C., Webb, R. H., & Sliney, D. H. (2007). Maximum permissible exposures for ocular safety (ANSI 2000), with emphasis on ophthalmic devices. *JOSA A*, 24(5), 1250-1265.
- [8] Alenin, A. S., & Tyo, J. S. (2014). Generalized channeled polarimetry. *JOSA A*, 31(5), 1013-1022.

Chapter 4 System Calibration and Mueller Matrix Reconstruction

4.1 System calibration

As mentioned in the earlier chapters, the calibration and Mueller matrix (MM) reconstruction approaches are closely related in a snapshot channeled MM polarimeter. Several approaches could be used for channeled MM polarimeter calibration [1-3]. The system errors to be compensated by calibration include misalignments in optics, birefringence in optical coatings, *etc.* For the channeled snapshot imaging MM polarimeter configuration introduced by Kudenov *et al.* [4], two different approaches were applied in the past to conduct the calibration and MM reconstruction, which tried to calibrate the PSG and the PSA simultaneously as a single instrument [4,5]. However, neither of the approaches could provide satisfactory calibration or MM reconstruction performance for the device to work practically. With the PSA and the PSG coupled in calibration and MM reconstruction procedures, the complexity of channel multiplexing is high. As a result, small tilts and wedges were often misregistered as polarization characteristics of the samples under tests. To simplify the situation, we propose a new perspective to the calibration and MM reconstruction of the system. If regarded separately, the PSA, optics in the imaging pathway and the FPA sensor from a complete channeled snapshot Stokes polarimeter as described in [2]. And the PSG is a polarization modulator which provides light input to the PSA with spatially periodic polarization states. Thus, for the calibration of the SRIMMP instrument, the imaging pathway could be calibrated as an independent channeled snapshot imaging Stokes polarimeter, while there is no need to calibrate the illumination pathway, as it is just a provider of input polarization states to the Stokes polarimeter. With this perception, in retinal MM reconstruction of SRIMMP, the 2D MM from retina would be revealed by comparing the Stokes parameters measured by the imaging pathway before and after the retina is placed into the system. Even if

polarization-related errors exist in the illumination pathway, as long as they are consistent, the influence of them would be offset in the MM reconstruction process.

To calibrate the imaging pathway as a channeled snapshot imaging Stokes polarimeter, the illumination pathway is temporarily taken away from the system. Illumination from a diffuser arrives at the imaging pathway of the SRIMMP after passes through different calibration samples made of LP or LP + QWP at various orientations one at a time. If the incident polarization state can be described by Stokes vector as $[S_1, S_2, S_3, S_4]^T$, the intensity fringes on the FPA have the following expression:

$$I(x, y) = S_0(x, y) + S_1(x, y)\cos[2\pi U(x + y)] + S_2(x, y)\sin[2\pi U(x + y)] + S_3(x, y)\cos[2\pi U(y)] \quad (1)$$

where I is the intensity at position (x, y) , U is the unit spatial carrier frequency. Apply a 2D Fourier transform to the intensity expression above, gives the corresponding frequency domain expression as:

$$I(\varepsilon, \eta) = S_0(\varepsilon, \eta) + \frac{1}{4}[S_1(\varepsilon, \eta) + iS_2(\varepsilon, \eta)][\delta(\varepsilon + U, \eta + U) + \delta(\varepsilon + U, \eta - U) + \delta(\varepsilon - U, \eta + U) + \delta(\varepsilon - U, \eta - U)] + \frac{1}{2}S_3(\varepsilon, \eta)[\delta(\varepsilon, \eta + U) + \delta(\varepsilon, \eta - U)] \quad (2)$$

where ε and η are the Fourier domain variables correspond to x and y in the spatial domain, respectively. δ is the Dirac delta function. The expression in Eq. 2 reveals the existence of three non-conjugate channels in the Fourier domain, associated with S_0 , $S_1 + iS_2$ and S_3 , respectively. The distribution of Fourier domain channels is as depicted in Figure. 4-1, note that only non-conjugated channels appear in the graph.

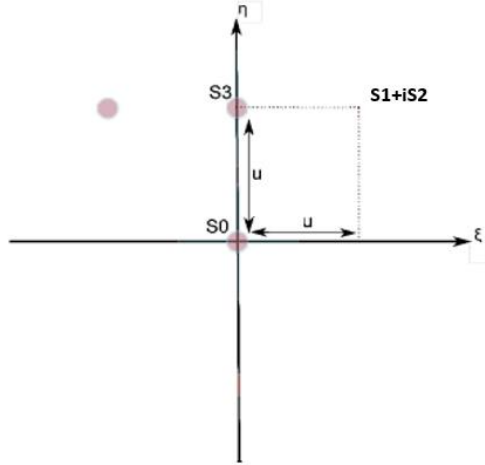


Figure. 4-1. Ideal channel distribution of the PSA in Fourier domain, ϵ and η are Fourier domain coordinates correspond to the spatial coordinates x and y , only non-conjugated channels are shown in the graph.

It should be noted that, Figure. 4-1 shows the ideal distribution of spatial frequency channels. In practice, due to imperfections in PGs, sub-channels would appear. As long as the magnitude of these sub-channels is negligible when compared to that of the major channels, the accuracy of Stokes parameters measurement wouldn't be affected too much. To acquire the isolated channel contents in the spatial domain, we could apply 2D filters to each Fourier domain channel depicted in Figure. 4-1, and then perform an inverse Fourier transform after the filtering. The isolated spatial domain channels are denoted as C_0 , C_1 and C_2 .

$$C_0 = S_0(x, y), \quad (3)$$

$$C_1 = \frac{1}{4}[S_1(x, y) + iS_2(x, y)]e^{(i2\pi Ux + 2\pi Uy)}, \text{ and} \quad (4)$$

$$C_2 = \frac{1}{2}S_3(x, y)e^{i2\pi Uy} \quad (5)$$

From the above equations of channel contents, it is obvious that S_0 can be directly extracted from C_0 , while S_1 , S_2 and S_3 are modulated by phase factors, and cannot be directly retrieved from C_1 and C_2 . To demodulate the phase factors and retrieve S_1 , S_2 and S_3 , the isolated channels from

sample data are compared to those of two previously recorded reference frames with pure linear polarization and pure circular polarization states, respectively. The influence of phase factors can be eliminated by division and normalization between data channels and reference channels. This demodulation technique is called the reference beam technique [2].

$$S_0(x, y) = |C_{0,sample}|, \quad (6)$$

$$\frac{S_1(x, y)}{S_0(x, y)} = \text{Re} \left[\frac{C_{1,sample}}{C_{1,reference}} \times \frac{C_{0,reference}}{C_{0,sample}} \right], \quad (7)$$

$$\frac{S_2(x, y)}{S_0(x, y)} = \text{Im} \left[\frac{C_{1,sample}}{C_{1,reference}} \times \frac{C_{0,reference}}{C_{0,sample}} \right], \text{ and} \quad (8)$$

$$\frac{S_3(x, y)}{S_0(x, y)} = \text{Re} \left[\frac{C_{2,sample}}{C_{2,reference}} \times \frac{C_{0,reference}}{C_{0,sample}} \right]. \quad (9)$$

In Eq. 6 through Eq. 9, $C_{i,sample}$ ($i = 0, 1, 2$) represents channel demodulated from the sample frame, and $C_{i,reference}$ ($i = 0, 1, 2$) represents channel demodulated from the reference frames. Stokes parameters demodulated are normalized by the intensity. The compensation of phase factors is a part of the SRIMMP calibration.

Additional errors arise from imperfections in PG fabrication, retardance/mis-alignments of optics, *etc.* They must be compensated through calibration as well. In Mueller calculus, a PG is equivalent to a half wave plate with periodic fast axis orientation along its grating direction. The PSA in our system is made of two orthogonal PGs, a LP, and a QWP, the MM of it can be written in the form of matrix multiplication as:

$$A(x, y) = M_{LP}(0) * M_R(\theta_2(x, y), 180 + \Phi_3) * M_R(0, 90 + \Phi_2) * M_R(\theta_1(x, y), 180 + \Phi_1) \quad (10)$$

where \mathbf{A} is the PSA's MM, θ_1 is the fast axis orientation of the first PG, θ_2 is the fast axis orientation of the second PG, Φ_1 , Φ_2 , Φ_3 are errors caused by PG imperfections, optics

misalignment or system retardance in the imaging pathway, **MR** denotes the MM of a general retarder. Figure. 4-2 is an example of the Fourier domain channel distribution when Φ_1, Φ_2, Φ_3 all equal to 10° .

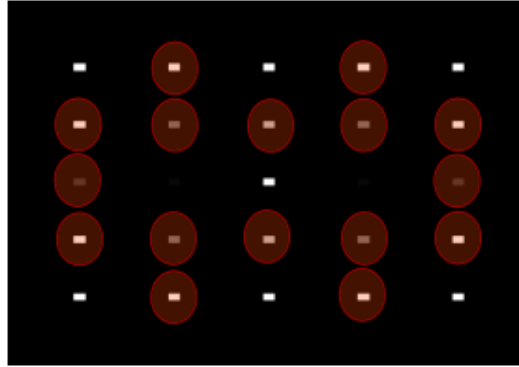


Figure. 4-2. The Fourier domain of the PSA when the two PGs and the QWP each has 10° retardance error. Channels circled are additional channelled due to the errors.

As depicted in Figure. 4-2, system errors in the system result in additional spatial frequency channels. These additional channels take energy away from the main channels, cause inaccuracies in the measurement of Stokes parameters. Since this effect is mostly linear, it can be calibrated by creating a correction matrix at each spatial domain pixel for the measured Stoke parameters. To get this correction matrix, more than 16 sample frames with known polarization states are needed. Calibration samples made of LP and QWP could be used to generate these known polarization states. A possible calibration procedure is as sketched in Figure. 4-3.

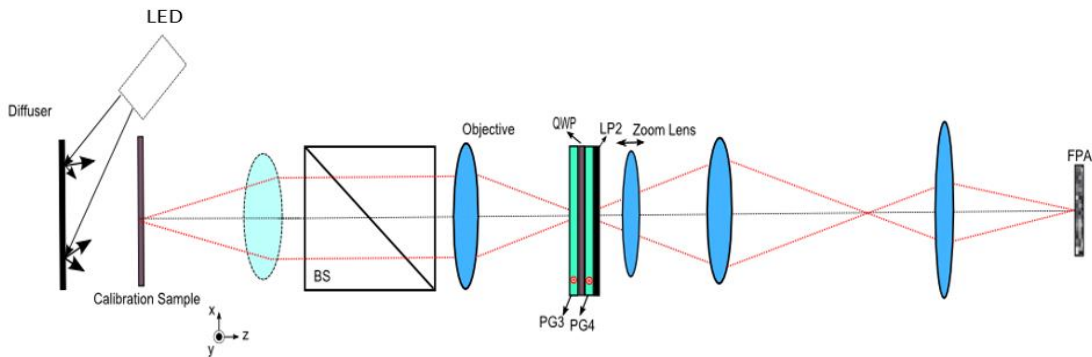


Figure. 4-3. The SRIMMP calibration with calibration samples used to generate known polarization states.

In practice, 38 different polarization states were generated by the combination of a LP and a QWP with different transmission axis and fast axis orientations. The illumination source was taken from the illumination pathway of the SRIMMP to keep the wavelength consistent in calibration and instrument test. For better performance, the diffuser in Figure. 4-3 was replaced by an integration sphere during calibrations. The calibration configuration of the device is as illustrated in Figure. 4-4.

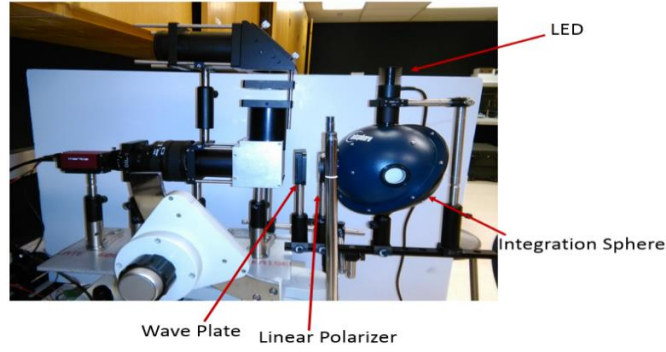


Figure. 4-4. The calibration setup for the SRIMMP.

Using the reference beam technique, the Stokes parameters from the 38 known polarization states were measured. With the measured polarization states, a 4×38 matrix of measured Stokes parameters could be generated for every pixel in the ROI as:

$$\mathbf{S}_{\text{meas}} = \begin{pmatrix} S_{m0,t1} & S_{m0,t2} & S_{m0,t3} & \dots S_{m0,t38} \\ S_{m1,t1} & S_{m1,t2} & S_{m1,t3} & \dots S_{m1,t38} \\ S_{m2,t1} & S_{m2,t2} & S_{m2,t3} & \dots S_{m2,t38} \\ S_{m3,t1} & S_{m3,t2} & S_{m3,t3} & \dots S_{m3,t38} \end{pmatrix} \quad (11)$$

where the subscript m_j ($j = 0, 1, 2, 3$) refers to the j th measured Stokes parameter. Similarly, another 4×38 matrix of the nominal Stokes parameters could be generated in the same fashion.

$$\mathbf{S}_{\text{nom}} = \begin{pmatrix} S_{n_0,t_1} & S_{n_0,t_2} & S_{n_0,t_3} & \dots S_{n_0,t_{38}} \\ S_{n_1,t_1} & S_{n_1,t_2} & S_{n_1,t_3} & \dots S_{n_1,t_{38}} \\ S_{n_2,t_1} & S_{n_2,t_2} & S_{n_2,t_3} & \dots S_{n_2,t_{38}} \\ S_{n_3,t_1} & S_{n_3,t_2} & S_{n_3,t_3} & \dots S_{n_3,t_{38}} \end{pmatrix} \quad (12)$$

where the subscript n_i ($i = 0, 1, 2, 3$) refers to the nominal values of Stokes parameters, t_j refers to the i th sample. A 4×4 correction matrix could be then generated by applying linear algebra operations to both 4×38 matrices.

$$\mathbf{W} = \begin{cases} W_{\text{row1}} = (\text{pinv}(S_{\text{nom}}) * S_{\text{meas,column1}})^T \\ W_{\text{row2}} = (\text{pinv}(S_{\text{nom}}) * S_{\text{meas,column2}})^T \\ W_{\text{row3}} = (\text{pinv}(S_{\text{nom}}) * S_{\text{meas,column3}})^T \\ W_{\text{row4}} = (\text{pinv}(S_{\text{nom}}) * S_{\text{meas,column4}})^T \end{cases} \quad (13)$$

In Eq. 13, pinv denotes the pseudoinverse operation. It should be noted that, the operation in Eq. 13 is valid only when the condition number of the 4×38 matrix with nominal Stokes parameters is small otherwise the results would subject to large numerical errors. To obtain matrices with small condition numbers, the combination of calibration sample must be carefully selected. The correction matrix \mathbf{W} could be used for correcting future measurements, as it is the bridge between measured Stokes parameter values and real Stokes parameter values. Let the measured Stokes vector be \mathbf{S} , the corrected Stokes vector \mathbf{S}' can be determined by:

$$\mathbf{S}' = \text{inv}(\mathbf{W}) * \mathbf{S} \quad (14)$$

To evaluate the performance of the aforementioned calibration procedure, the generated correction matrices were applied to the measured Stokes parameters from the calibration samples. In an ideal scenario, the corrected Stokes parameter would perfectly match the nominal values. In practice, however, there is still a little discrepancy between the corrected values and the nominal values, especially in S_3 when its real value is close to 0. This is likely caused by the errors in the

manual calibration procedure and could be minimized by repeating the calibration process until a satisfactory result is obtained.

4.2 2D Mueller matrix reconstruction

After being calibrated, the imaging pathway of the SRIMMP device could be seen as an accurate snapshot imaging Stokes polarimeter, which measures 2D polarization states of the incident light. Based on this, Mueller matrices of a 2D scene could be reconstructed by comparing the input and the output Stokes parameters. With the PSG and the illumination pathway in the system, additional frequency domain channels would appear around the PSA channels shown in Figure. 4-1. This is caused by the low-frequency spatial modulation of polarization states. The Fourier domain channel distribution of the polarization fringe pattern received by the FPA is as depicted in Figure. 4-5. The graph shows all the ideal channels, in practice there might be less channels, depending on the sample under test.

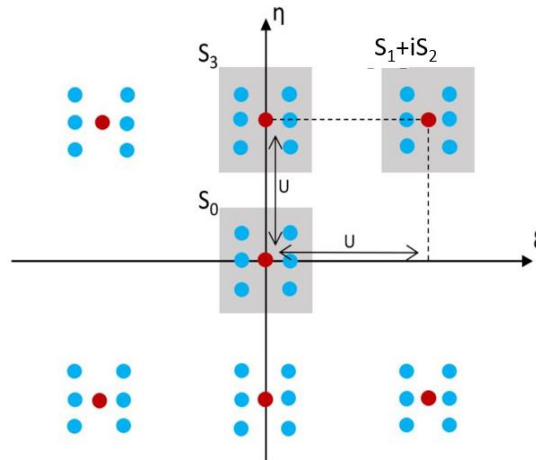


Figure. 4-5. Fourier domain spatial frequency channel distribution of PSA with incident polarization states from the PSG. The relationship between channels and Stokes coefficient are as labeled.

Prior to the acquisition of sample frame, the input Stokes parameters should be determined first. This can either be done by taking an “empty polarimeter” frame or by running a fitting program, which will be discussed in detail later. The output Stokes parameters $[S_{0,out}, S_{1,out}, S_{2,out},$

$S_{3,out}$] could be demodulated from sample frame by applying reference beam technique. With both input and output Stokes parameters, an input measurement matrix S_{in} and an output measurement matrix S_{out} can be formed by combining the Stokes parameters of every pixel in a small square window [6], as shown in Figure. 4-6, where N is the number of the pixels within the square window. The intrinsic assumption here is, the MM of every pixel in the region is similar. The size of the synthesis window has to be chosen such that it covers at least one full period of the spatial carrier frequency in both x and y directions, otherwise S_{in} and S_{out} might be ill-conditioned.

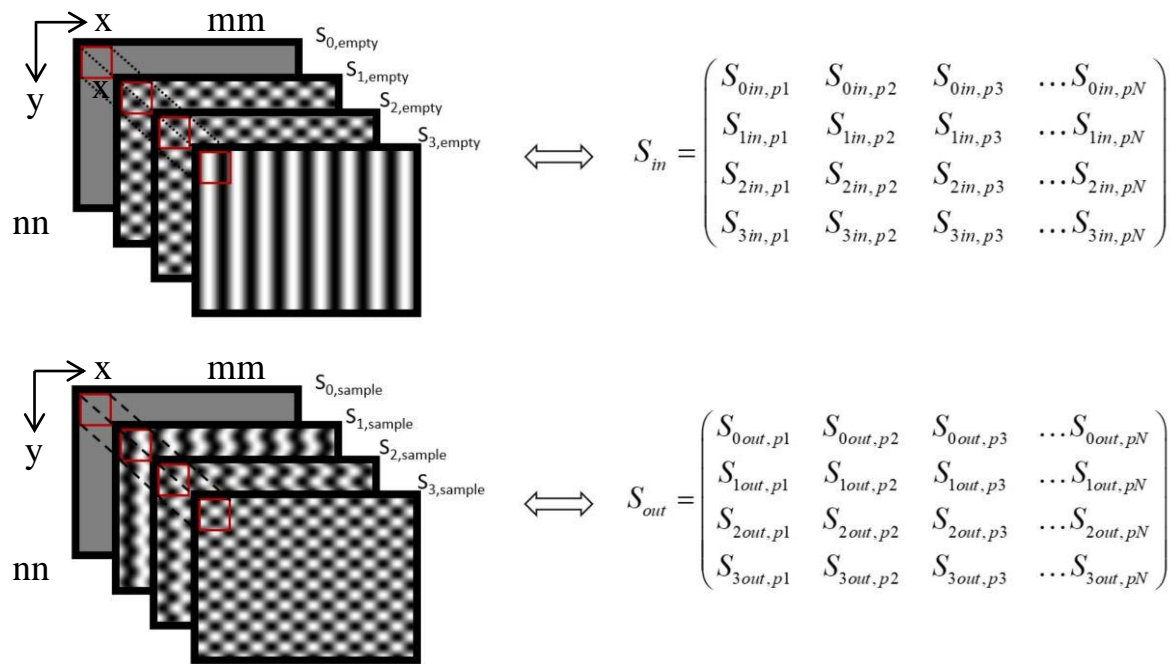


Figure. 4-6. Schematic of how to form the S_{in} matrix and the S_{out} matrix from Stokes parameters obtained using reference beam technique. N is the number of pixels within the square filter window.

With the two over-defined matrices S_{in} and S_{out} , the corresponding MM can be calculated by:

$$MM = \begin{cases} MM_{row1} = (pinv(S_{in}) * S_{out, column1})^T \\ MM_{row2} = (pinv(S_{in}) * S_{out, column2})^T \\ MM_{row3} = (pinv(S_{in}) * S_{out, column3})^T \\ MM_{row4} = (pinv(S_{in}) * S_{out, column4})^T \end{cases} \quad (15)$$

where p_{inv} represents the pseudoinverse operation. After the MM of one position is acquired, the square filter window would be moved to the next position with a shift of only one pixel. This process is repeated until every pixel of the 2D scene is traversed by the filter window. The resulting datacube will be a 4D matrix with a size of $nn \times mm \times 4 \times 4$, where nn and mm are integers denoting the horizontal and vertical dimensions of the 2D area.

In practice, the input Stokes parameters of the 2D scene can be obtained in two ways, one through an “empty polarimeter” frame taken before the actual test starts, the other through a fitting program coded in Matlab. The two approaches are discussed below.

4.2.1 2D input Stokes parameters from the “empty polarimeter” frame

The “empty polarimeter” frame is taken with an empty model eye. The input Stokes parameters can be acquired from this frame following the same procedure as in the acquisition of output Stokes parameters. The procedure of MM reconstruction in this fashion can be briefly summarized as follow:

- Calibrate the system with 38 standard polarization states, acquire the calibration matrix for each pixel in the ROI
- Take polarization modulation and intensity modulation frames from target and empty model eye, the intensity modulation frame will be discussed later
- Filter the intensity modulation frame to only reserve the comparatively low frequency features
- Acquire the input Stokes parameters of each pixel through the isolated frequency channels by using reference beam method
- Apply calibration matrices to the input Stokes parameters, as mentioned earlier

- Map the input Stokes parameters to match the coordinates on the polarization modulation frame by using image registration algorithms, with intensity modulation as registration targets. The algorithm applied here involves only tilt and translational moves on the xoy plane
- Acquire the output Stokes parameters of each pixel from the polarization modulation frame with reference beam technique
- Apply calibration matrices to the output Stokes parameters
- Reconstruct the Mueller matrices with both input and output Stokes parameters, within a square moving-window filter

4.2.2 2D input Stokes parameters from the Stokes parameter fitting program

In addition to the “empty polarimeter” frame, input Stokes parameters could also be obtained through a fitting procedure. This needs a fitting target, which is to be obtained from the same target as the data frame. The fitting target was chosen to be the PSG’s intensity modulation pattern acquired by inserting a linear polarizer (LP) between the PSG and the beamsplitter when capturing images. With this LP, the spatial-variant polarization states from the PSG are analyzed before light entering the imaging pathway. This results in a low-frequency intensity modulation that can be recorded by the FPA without being affected by any influence from the sample or the system components in the imaging pathway. Figure. 4-7 illustrates an example of the PSG intensity modulation frame captured by the FPA, the low-frequency sinusoidal intensity modulation and the high-frequency polarization fringes from the PSA both present on the image. A low-frequency filter could be applied to the Fourier domain of the PSG intensity modulation frame to filter out the polarization fringes from the PSA and leave only the PSG intensity modulation pattern on the frame, as input Stokes parameters fitting target.

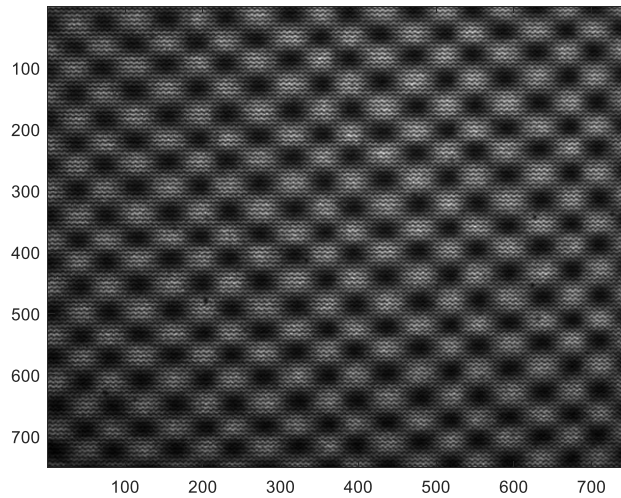


Figure. 4-7. A PSG intensity modulated frame from with an empty model eye.

Since the sinusoidal PSG intensity modulation contains information of phase and magnitude from input polarization states, it can be used as target for input Stokes parameters fitting. To minimize the influence of unconscious eye movements, a PSG intensity modulation frame must be taken immediately after the corresponding data frame. A motor-driven rotational plate was designed for the capture of PSG intensity modulation frames. As can be seen from the Solidworks model in Figure. 4-8, the rotational plate has four symmetrical 2-inch round slots on it to hold polarization elements like polarizers and waveplates. The rotational plate locates right below the PSG plane, connects to the rest of the system through a cover case, which consists of an upper piece and a lower piece. The cover case holds a photodiode and a LED of a simple light triggering circuit. Once the motor is powered up, the rotational wheel repeatedly inserts the LP into the illumination pathway. When one of the four 2-inch round slots is aligned with the lens tubes of the illumination pathway, a notch on the edge of the rotational plate allows light from the LED to shine upon the photodiode. This creates a change in the electrical resistance of the photodiode, which is converted to a pulse signal by the triggering circuit. This pulse signal is then sent into the

camera at the end of the imaging pathway through wire connection to trigger a snapshot. Through synchronizing the speed of the rotational plate and camera exposure time, occlusion on captured images can be avoided.

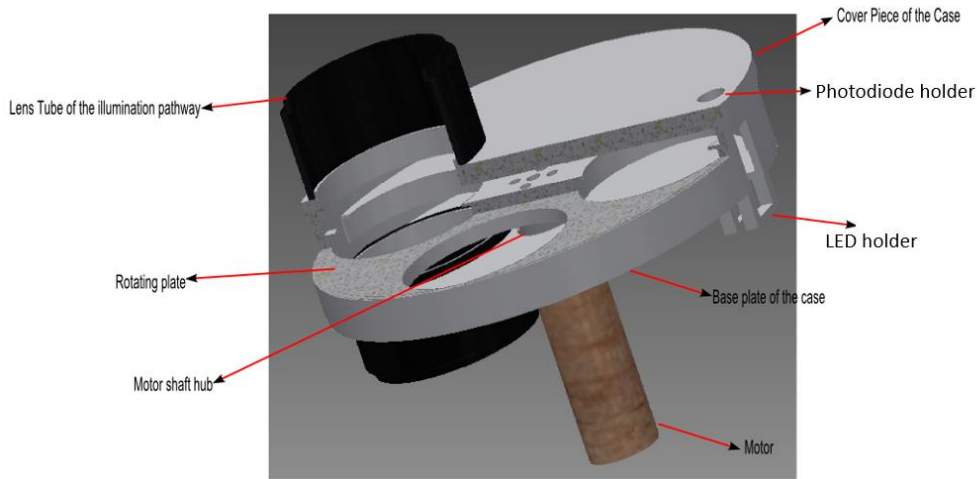


Figure. 4-8. The 3D CAD design for the rotational plate in Solidworks.

In practice, the rotational plate was incorporated into the SRIMMP device without the cover case, due to the limited space beneath the PSG. Accordingly, the original light switch circuit was replaced by an infrared proximity sensor placed below the rotational plate. Triggering principle and synchronization procedure remained unchanged. A plastic shield was added to make sure the rotational plate does not touch the forehead of patients during clinical tests.

A first-order fitting model was coded in Matlab to estimate the input Stokes parameters at each pixel from the filtered sinusoidal PSG intensity modulation pattern. The model was written following the Mueller calculus, eight parameters of the PSG are to be estimated, including the main grating frequency, the secondary grating frequency, the magnitude of the main frequency component, the magnitude of the secondary frequency component, the phase of the main frequency component, the phase of the secondary frequency component, *etc.* These eight variables were selected from a variety of variables through trials to model the possible errors in the PSG, since

too many variables would increase the complexity of the fitting model and drastically reduce the credibility of fitting results. The Matlab command *fminsearch* is used in the fitting model to find the scalar minimum of residue error. Several functions were also written in Matlab to reduce the complexity of the fitting model and increase its robustness. The fitting procedure is done in two steps. First, *fminsearch* is used to fit a down-sampled version of the sinusoidal intensity modulation pattern to guess the initial values of the variables before the detailed fitting begins. Then, detailed fitting is carried out in smaller sub-sections with the initial guess of fitting parameters as start point. In some instances, constraints among the fitting parameters can also be placed to further increase the robustness of this fitting procedure. The fitted Stokes parameters do not need to be corrected by the correction matrix, because they are fitted from a pattern that is not affected by the retardance errors in the imaging pathway of the SRIMMP.

The steps of MM reconstruction through input Stokes parameter fitting are summarized as follow:

- Calibrate the system with the 38 standard polarization states acquire the calibration matrices for each pixel on the MM reconstruction region
- Take polarization modulation and PSG intensity modulation frames from subject's eye
- Filter the intensity modulation frame to only reserve the comparatively low frequency features
- Acquire the input Stokes parameters through a fitting model, with the filtered intensity modulation pattern as fitting target
- Acquire the output Stokes parameters of each pixel from the polarization modulation frame with reference beam technique

- Apply calibration matrices to the output Stokes parameters
- Reconstruct the Mueller matrices with both input and output Stokes parameters, using a moving square window filter

Comparing to obtaining the input Stokes parameters from empty polarimeter frames, using a fitting model has both advantages and disadvantages. A major advantage is, with this approach, the source images of both the input and the output Stokes parameters come from the same target (retina), the potential MM reconstruction errors caused by the differences between model eye and retina are eliminated. The biggest disadvantage is, the acquisition of PSG intensity modulation frames makes the SRIMMP a quasi-snapshot system, because two frames must be taken during the test, instead of just one. Through system integration, the two frames can still be taken within a very short time by one-click in the control program, there's no need for image registration between them either. As a result, the advantages of snapshot are still preserved in this quasi-snapshot scenario.

4.3 Simulation model of system calibration and 2D Mueller matrix reconstruction

A first-order simulation model was coded in Matlab to verify the above-mentioned system calibration approach and data reconstruction technique. The ROI was defined as a 200×200 square, the MM reconstructed is to be carried out for every pixel in this square region. The model starts with the generation of reference beam images and calibration samples. Figure. 4- 9 illustrates the simulated reference beam images, one with linear polarization at 0° degree and the other with right circular polarization. The intensity fringes recorded by the PSA are as depicted. Calibration samples are in similar forms as the reference beam samples, just with different polarization orientations.

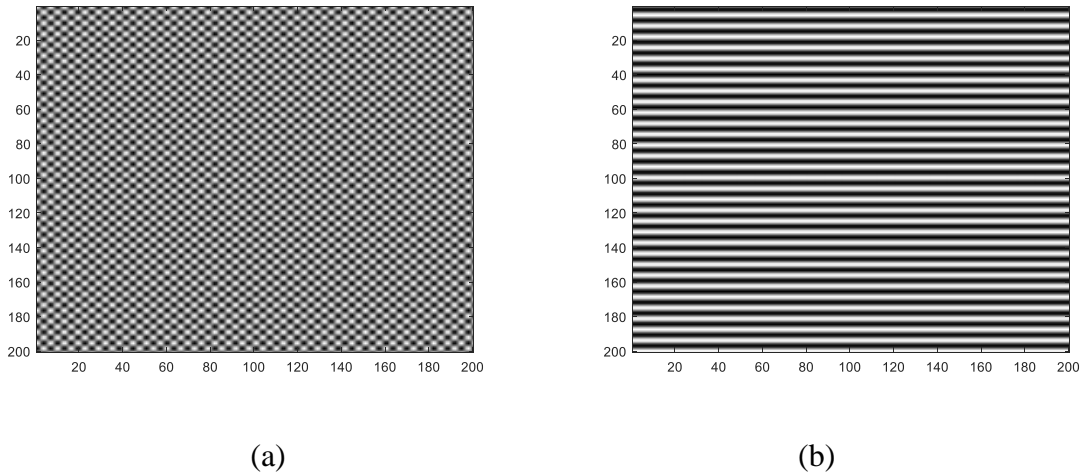


Figure. 4-9. The intensity fringes on simulated reference beam images with a) linear polarization at 0° , and b) right circular polarization.

After calculating the correction matrix \mathbf{W} for every pixel in the 200×200 square, the polarization fringes are generated by the simulation model with “empty polarimeter” configuration. The polarization fringes are as depicted in Figure. 4-10, with a 6:1 ratio between the PG periods in the PSG and the PSA.

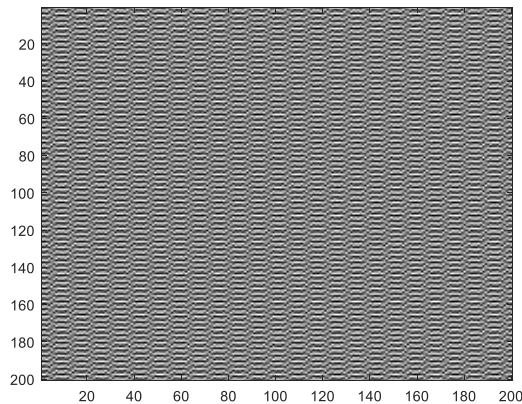


Figure. 4-10. The intensity fringes on simulated reference beam images with a) linear polarization at 0° , and b) right circular polarization.

The simulation model isolates spatial frequency channels from the “empty polarimeter” frame in Fourier domain and inversely transfer them into spatial domain. The Stokes parameters

are extracted from these isolated channels using the reference beam technique mentioned earlier in this chapter, as shown below after applying the correction matrices obtained from calibration.

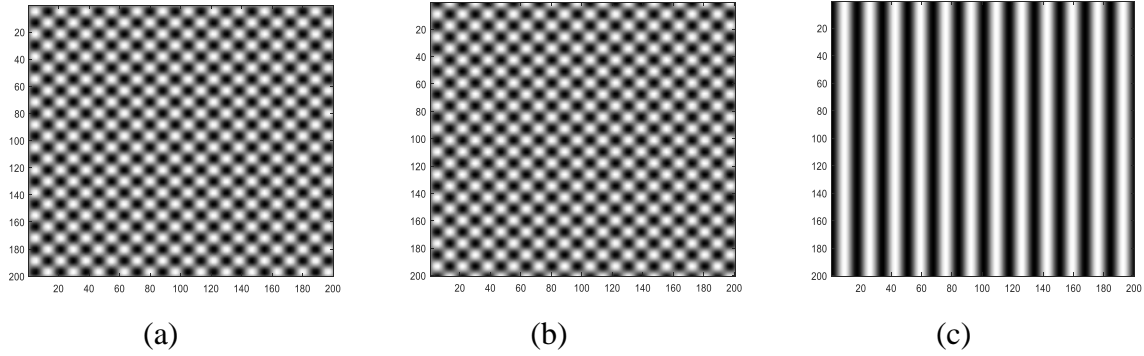


Figure. 4-11. The demodulated 2D Stokes parameters a) S_1 , b) S_2 , and c) S_3 from the “empty polarimeter” frame generated by the simulation model.

The sample to be “measured” in the simulation model contains a cross-shaped area in the middle with different MM, as depicted in Figure. 4-12.

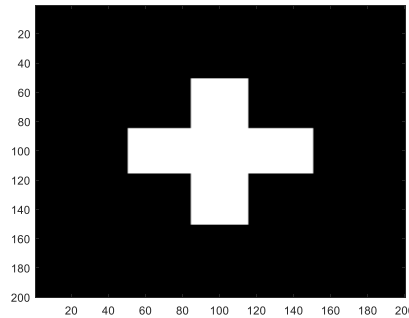


Figure. 4-12. An illustration of the test sample in the simulation model. The pixels on the central cross-shaped region have Mueller matrices that are different from those of the other pixels.

Every pixel in the cross-shaped area has a MM as shown below in Eq. 16, which is the MM of a half wave plate with its fast axis oriented at 25° . The other pixels on the 200×200 square have 4×4 identity matrices as their MMs.

$$\mathbf{MM}_{\text{cross}} = \begin{bmatrix} 1 & 0 & 0 & 0 \\ 0 & -0.1736 & 0.9848 & 0 \\ 0 & 0.9848 & 0.1736 & 0 \\ 0 & 0 & 0 & -1 \end{bmatrix} \quad (16)$$

The Stokes parameters of the test sample are demodulated from the simulated polarization fringes using reference beam technique. Based on the demodulated Stokes parameters from both the “empty polarimeter” frame and the test sample frame, the 2D MM is reconstructed using the moving-window-filter method as described in section 4.2. The size of the square window filter is set to be 17×17 , slightly larger than the PSG period in both horizontal and vertical directions. The reconstructed 2D MM is as depicted in Figure. 4-13. As can be seen, the cross-shaped area is clearly differentiable from the background at m_{22} , m_{23} , m_{32} , m_{33} and m_{44} . Some ripples can be seen near the edges of the cross, due to averaging errors in the MM reconstruction process. This effect can be mitigated by increasing the size of the square window filter. However, doing this would also decrease the resolution of the reconstructed 2D MM. To avoid the resolution decrease, we can keep the size of the square window unchanged and increase the grating frequency of the PSG. When planning the reconstruction of 2D MMs from a specific scene, filter window size, PSG grating frequency and image resolution should all be considered simultaneously.

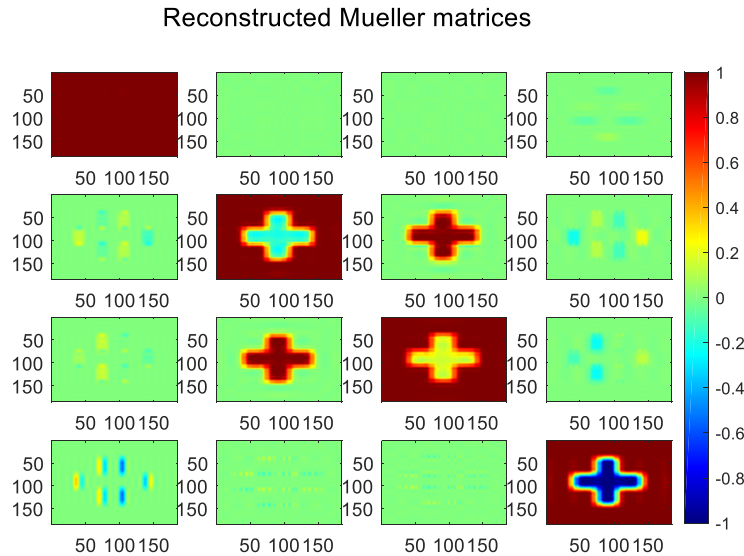


Figure. 4-13. The reconstructed 2D Mueller matrix from the Matlab simulation model.

The average MM of 20×20 pixels in the center of the cross-shaped area is

$$\mathbf{MM}_{\text{reconstructed}} = \begin{bmatrix} 0.999 & 0.0002 & -0.0001 & 0.0001 \\ -0.0003 & -0.1869 & 0.9942 & 0.0001 \\ 0.0017 & 0.995 & 0.1664 & -0.0055 \\ -0.0032 & -0.0022 & -0.0043 & -1.0078 \end{bmatrix}. \quad (16)$$

The absolute differences between the measured MM and the target MM is then

$$\mathbf{MM}_{\text{difference}} = \begin{bmatrix} 0.0001 & 0.0002 & 0.0001 & 0.0001 \\ 0.0003 & 0.0133 & 0.0094 & 0.0001 \\ 0.0017 & 0.0102 & 0.0073 & 0.0055 \\ 0.0032 & 0.0022 & 0.0043 & 0.0078 \end{bmatrix}. \quad (17)$$

As can be seen, the maximum absolute difference between the two MMs is at m_{22} with a value of 0.0133, or 1.33% of the maximum possible value of MM elements. The MM reconstruction result from the Matlab simulation model verifies that, the system calibration approach and the MM reconstruction technique described in this chapter are theoretically feasible and can be potentially applied to practical data.

References

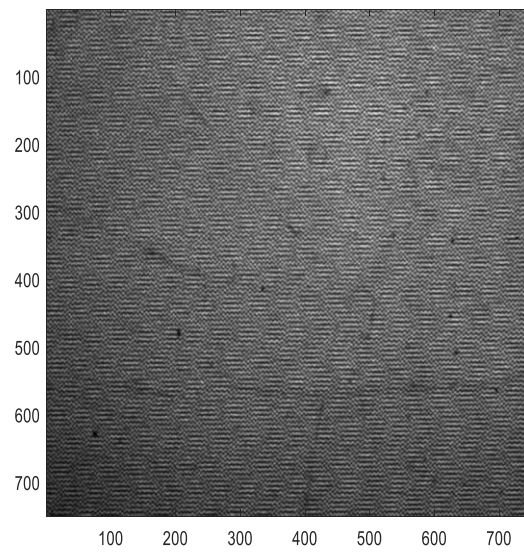
- [1] Dubreuil, M., Rivet, S., Le Jeune, B., & Cariou, J. (2007). Snapshot Mueller matrix polarimeter by wavelength polarization coding. *Optics express*, *15*(21), 13660-13668.
- [2] Kudenov, M. W., Escuti, M. J., Dereniak, E. L., & Oka, K. (2011). White-light channeled imaging polarimeter using broadband polarization gratings. *Applied optics*, *50*(15), 2283-2293.
- [3] Taniguchi, A., Oka, K., Okabe, H., & Hayakawa, M. (2006). Stabilization of a channeled spectropolarimeter by self-calibration. *Optics letters*, *31*(22), 3279-3281.
- [4] Kudenov, M. W., Escuti, M. J., Hagen, N., Dereniak, E. L., & Oka, K. (2012). Snapshot imaging Mueller matrix polarimeter using polarization gratings. *Optics letters*, *37*(8), 1367-1369.
- [5] Kudenov, M. W., Mallik, S., Escuti, M. J., Hagen, N., Oka, K., & Dereniak, E. L. (2013, October). Snapshot imaging Mueller matrix instrument. In *Electro-Optical Remote Sensing, Photonic Technologies, and Applications VII; and Military Applications in Hyperspectral Imaging and High Spatial Resolution Sensing* (Vol. 8897, p. 88970S). International Society for Optics and Photonics.

Chapter 5 Experimental Results

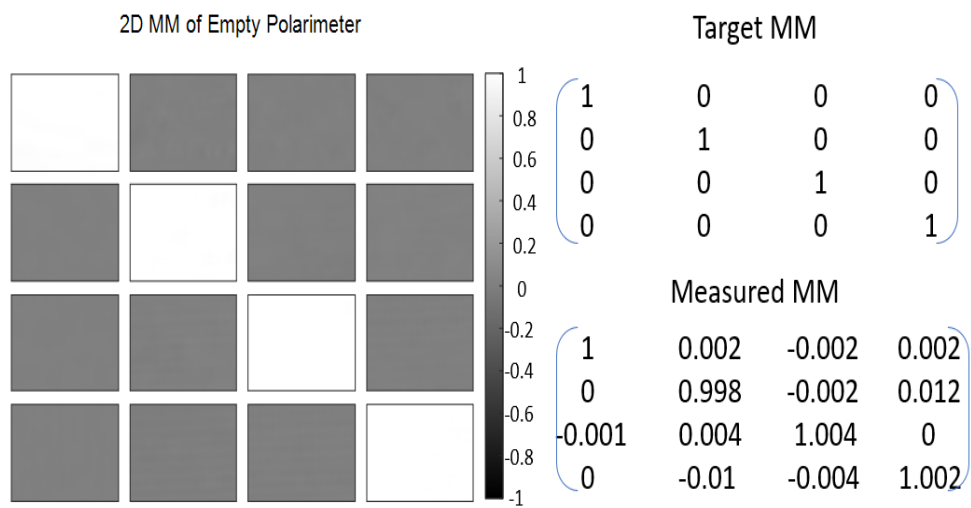
To validate the Mueller matrix (MM) reconstruction ability of the SRIMMP instrument, lab tests were conducted with the model eye as target. Three types of polarization scenarios were generated for the validation: air, linear polarizer (LP) and quarter wave plate (QWP). LPs and QWPs were taped onto the surface of the curved mirror at the back of the model eye to fit its shape. Since with model eye, the light passes through the samples twice before and after reflection, the retardance of the quarter wave plates doubles in the measurement, such that this type of test targets equal to half wave plates (HWP) in terms of retardance. MMs were reconstructed in a 701×701 pixels region using a 100×100 -pixel square filter window for air, HWP and LP samples. Empty polarimeter frame acquisition and system calibrations were done prior to the acquisition of data frames. The PSG intensity modulation frames were also recorded along with the data frames for the fitting model mentioned in previous chapters. Same pair of reference beam frames were used in both calibrations and data acquisition to eliminate any error caused by using difference references. Each MM coefficient was normalized by corresponding transmittance. Figure 5-1, Figure 5-2 and Figure 5-3 illustrate the MM reconstruction results of several different targets with an empty polarimeter frame as the source of input Stokes parameters. The average MM values were taken from a 200×200 square region within the areas covered by the target samples. Using input Stokes parameters from the fitting model generated similar results.

20 data frames with HWP were taken, each with a unique fast axis orientation of the HWP. The MM reconstruction results demonstrated an absolute error of 0.047 averaged across all 16 MM elements. 20 data frames with LP sample were also taken, each data frame with a unique transmission axis orientation of the LP. The MM reconstruction results demonstrated an absolute error of 0.064 averaged across all 16 MM elements. The average error of LP sample is larger,

because the data frames with LPs are comparatively darker and the darkest regions on them nearly reach the lower limit of the GigE camera's dynamic range. Thus, the stray light and random noise of the GigE camera severely affects the accuracy of MM reconstruction of these frames. This problem can be potentially solved by applying random noise reduction technique to the camera, together with subtracting stray light signal. Another type of error that can be observed from reconstruction results is the periodic fluctuation of MM values within the sample region. This is most likely caused by channel cross-talk in the Fourier domain, and can be potentially reduced by applying a 2D dual-beam background noise reduction technique like the one currently being used in polarimeter-spectrometers [1]. In addition, the surface reflection of samples could also contribute to the inaccuracies in 2D MM reconstruction, which can be potentially mitigated by creating a sample reflection model.

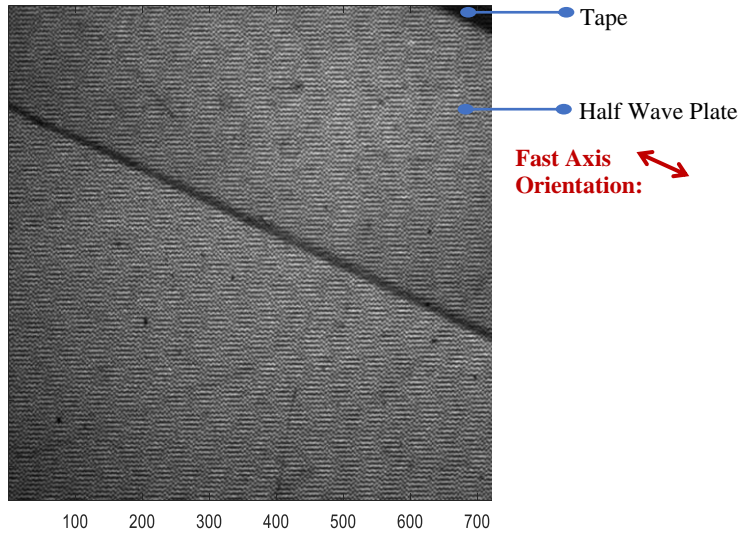


(a)



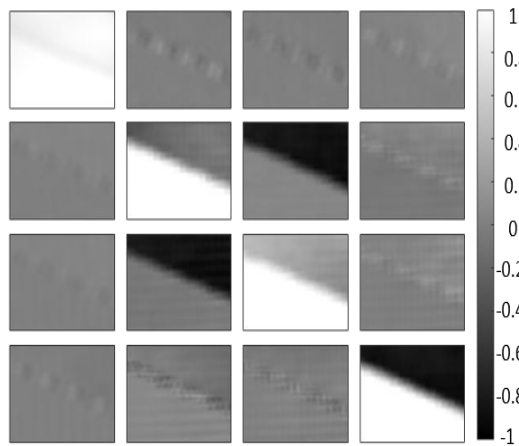
(b)

Figure. 5-1. a) Data frame from an empty polarimeter. b) The reconstructed 2D Mueller matrix of (a).



(a)

2D MM of Half Wave Plate with Fast Axis Oriented at 155°



Target MM

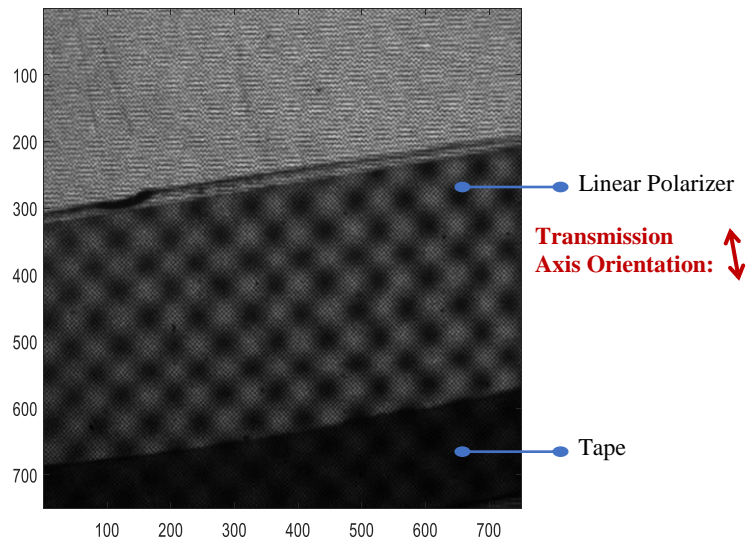
$$\begin{pmatrix} 1 & 0 & 0 & 0 \\ 0 & -0.174 & -0.985 & 0 \\ 0 & -0.985 & 0.174 & 0 \\ 0 & 0 & 0 & -1 \end{pmatrix}$$

Measured MM

$$\begin{pmatrix} 1 & -0.016 & -0.014 & 0.059 \\ 0.033 & -0.069 & -0.870 & 0.008 \\ 0.032 & -0.876 & 0.195 & 0.076 \\ -0.040 & -0.088 & -0.016 & -0.855 \end{pmatrix}$$

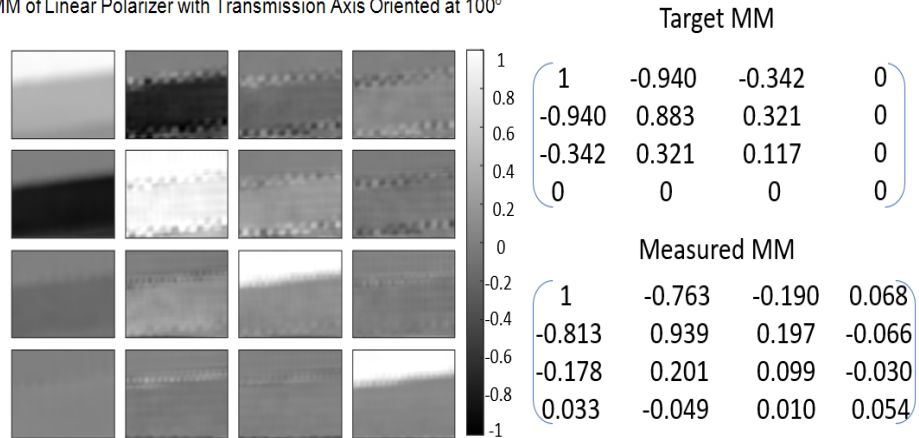
(b)

Figure. 5-2. a) Data frame from a half wave plate with fast axis oriented at 155°. b) The reconstructed 2D Mueller matrix of (a), each Mueller matrix coefficient is normalized by transmittance.



(a)

2D MM of Linear Polarizer with Transmission Axis Oriented at 100°



(b)

Figure. 5-3. a) Data frame from a linear polarizer with transmission axis 100° to the horizontal direction. b) The reconstructed Mueller matrix of (a), each Mueller matrix coefficient is normalized by light transmittance.

To reduce the errors in MM reconstruction, several techniques were proposed and tested. A scattering model was proposed to quantify the influence of scattered light, such that it could be subtracted from images acquired during the experiments. To find out the distribution of scattered light across the field of view (FOV) of the device, a cross-shaped dark tape with small width was

applied to the cover glass of the polarization state generator (PSG), the shadow of the dark cross was projected onto the fundus of the model eye by the imaging optics in the device. If no scattering exists in the SRIMMP system, on the captured image of the fundus, the area under the cross-shaped shadow should have no optical power after dark frame subtraction because the illumination of this area is blocked at the PSG plane. In practice, however, the recorded optical power underneath the cross-shaped shadow was not zero due to light scattering. Since the optical power from the covered area was contributed only by light scattering, the distribution of scattered light along horizontal and vertical directions could be extracted by examining the pixel values within the shadowed area. The distribution of scattered light along horizontal and vertical directions obtained using this method is as depicted in Figure. 5-4. The average reflection strength from the model eye fundus in the test was about 2300 (arbitrary unit).

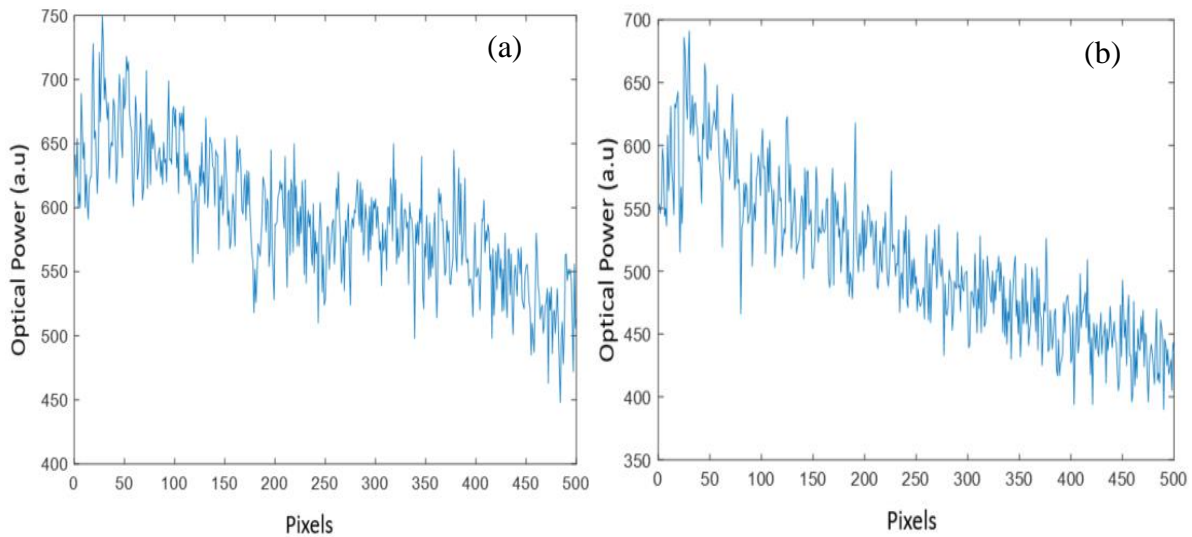


Figure. 5-4. The distribution of scattered light from the center of the FOV to the periphery along a) horizontal and b) vertical directions in the SRIMMP device.

With the light scattering distribution in both horizontal and vertical directions, the 2D distribution of scattered light can be derived, as depicted in Figure. 5-5.

During the experiments, the cross-shaped dark tape was lifted, and a small black dot made of dark tape was placed on the PSG cover glass at the periphery of the FOV. The shadow of the black dot was captured along with the images taken during experiments. Averaged optical power within the black dot region and the normalized 2D light scattering distribution were used together to deduce the 2D light scattering distribution of the corresponding images. Before being used in the reconstruction of 2D MM, the 2D light scattering distribution was subtracted from these images. This scattering subtraction method applies only to situations in which the symmetry of light scattering is not severely broken by the samples under test, for example, retinal tests.

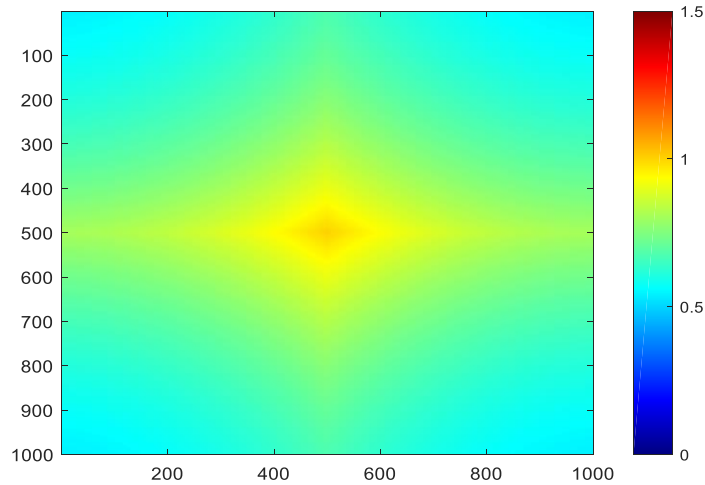


Figure. 5-5. The normalized 2D distribution of scattered light in the SRIMMP device.

The HWP test sample with its fast axis oriented at 155° was used to test the effectiveness of subtracting scattered light in 2D MM reconstruction. As depicted in Figure. 5-2, without subtracting scattered light, the maximum absolute error in the reconstructed MM elements is about 0.145, and the average error across all the 16 MM elements is about 0.055. After applying the subtraction of scattered light, the maximum absolute error in the reconstructed MM elements decreased from 0.145 to 0.131, and the average error across all the MM elements decreased from 0.055 to 0.053. Although subtracting the scattered light did help in reducing errors, the extent of

error reduction was rather small. This suggested that the influence of light scattering on MM reconstruction accuracy might not be as big as the previous expectation. Due to this reason, the scattering subtraction method is not included in the standard post-processing procedures of SRIMMP.

An additional calibration procedure was proposed, which creates 4×4 correction matrices for output Stokes parameters by investigating the relationship between the measured output Stokes parameters and the ideal output Stokes parameters from certain test samples. For example, a half wave plate with its fast axis 135° oriented has a MM as shown below

$$\mathbf{M}_{135^\circ} = \begin{bmatrix} 1 & 0 & 0 & 0 \\ 0 & -1 & 0 & 0 \\ 0 & 0 & 1 & 0 \\ 0 & 0 & 0 & -1 \end{bmatrix}, \quad (1)$$

such that the relationships between the input and output Stokes parameters are

$$\begin{cases} S_{0,out} = S_{0,in} \\ S_{1,out} = -S_{1,in} \\ S_{2,out} = S_{2,in} \\ S_{3,out} = -S_{3,in} \end{cases}, \quad (2)$$

where $S_{i,in}$ ($i = 0, 1, 2, 3$) denotes input Stokes parameter and $S_{i,out}$ ($i = 0, 1, 2, 3$) denotes output Stokes parameter. As mentioned in earlier chapters, the measured input and output Stokes parameters of the HWP can be obtained by using reference beam technique. With the relationships specified in Eq. 2, the ideal output Stokes parameters can be calculated from the measured input Stokes parameters. The 4×4 correction matrix at each pixel can be obtained by multiplying the pseudoinverse of a measurement matrix to an ideal value matrix, similar to the correction matrix generating procedure described in Chapter 4. The Stokes parameters used in the measurement matrix and the ideal value matrix of a pixel are collected from multiple locations near the pixel to

increase the condition numbers of the matrices. The generated 4×4 correction matrices can then be used to correct the measured output Stokes parameters from experiments with other polarizing element samples. As an example, applying the output correction matrices obtained from 135° oriented HWP to the 2D MM reconstruction of 155° oriented HWP, gives reconstructed 2D MM as illustrated in Figure. 5-6.

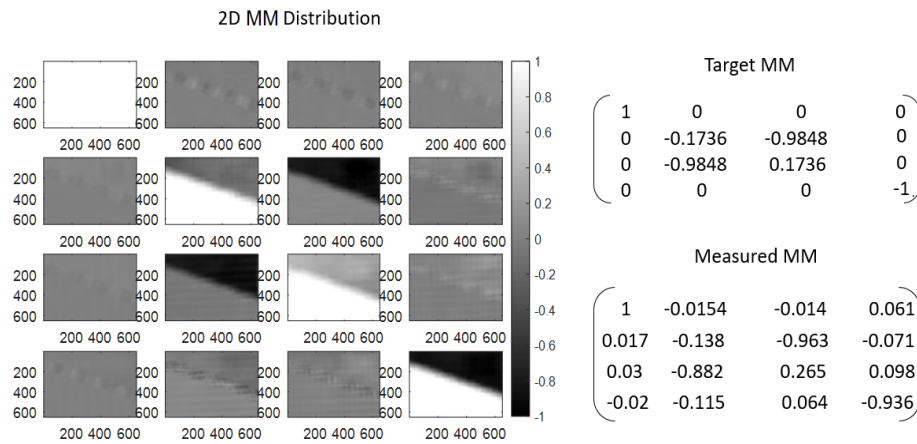


Figure. 5-6. The reconstructed 2D Mueller matrix from a half wave plate sample with its fast axis oriented at 155° . Output correction matrices were applied to the measured output Stoke parameters to increase reconstruction accuracy.

Comparing to the reconstruction result without output Stokes parameters correction, the maximum absolute error in the reconstructed MM elements decreased from 0.145 to 0.115, and the average error across all the MM elements decreased from 0.055 to 0.051. While the maximum error takes a major drop of about 20%, the drop in average error is not obvious. This additional correction method is not included in the standard post-processing procedures of SRIMMP due to its limited overall effect on the reduction of MM reconstruction errors.

References

- [1] Craven, J., & Kudenov, M. W. (2010). False signature reduction in channeled spectropolarimetry. *Optical Engineering*, 49(5), 053602.

Chapter 6 Preliminary Clinical Tests

Preliminary clinical tests of the SRIMMP instrument were carried out in the medical campus of the University of South California (USC). The SRIMMP device was connected to a windows laptop for real-time data acquisition. The rotational wheel was equipped to help acquiring the polarization state generator (PSG) intensity modulation frames along with the retinal data frames.

6.1 The control program of SRIMMP

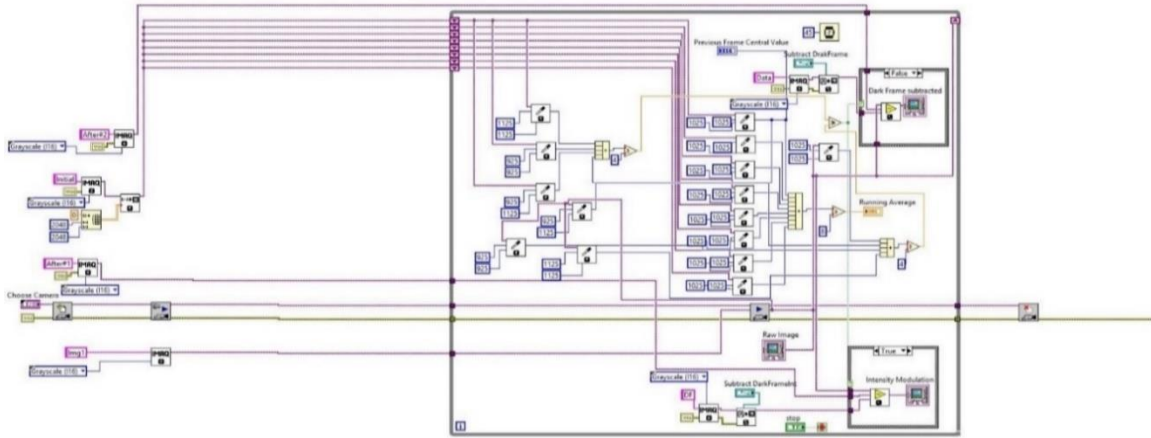
Different from the lab tests, in clinical tests several practical issues must be addressed before implementing data acquisition. First, a graphical user interface (GUI) needs to be provided, such that the operator can monitor the status of SRIMMP from the laptop. Second, the speed of the rotational wheel and the camera's exposure time must be synchronized to avoid blockage of field of view (FOV). Third, to collect enough reflectance from human retina, the illumination level must be higher than in the model eye tests. As a result, the light reflection from inside the beamsplitter also brings much greater noises to the data frames. This must be compensated before data acquisition to guarantee correct image contrast. Fourth, since the camera repeatedly shifts between capturing data frame and capturing PSG intensity modulation frame, the raw video stream constantly blinks and makes it difficult for the operator to observe retinal features.

A simple control program was coded using LabVIEW in response to these needs. As depicted in Figure. 6-1, the control system mainly consists of 3 modules: video stream separation & dark frame subtraction (VSSDFS), dark frame acquisition (DKFA) and data frame(s) acquisition (DTFA). The VSSDFS module pulls raw video stream from the GigE camera, divides it into two sub-streams: data stream and PSG intensity modulation stream according to the average intensity of captured frames, and displays the two sub-streams separately on the GUI panel. In addition, the

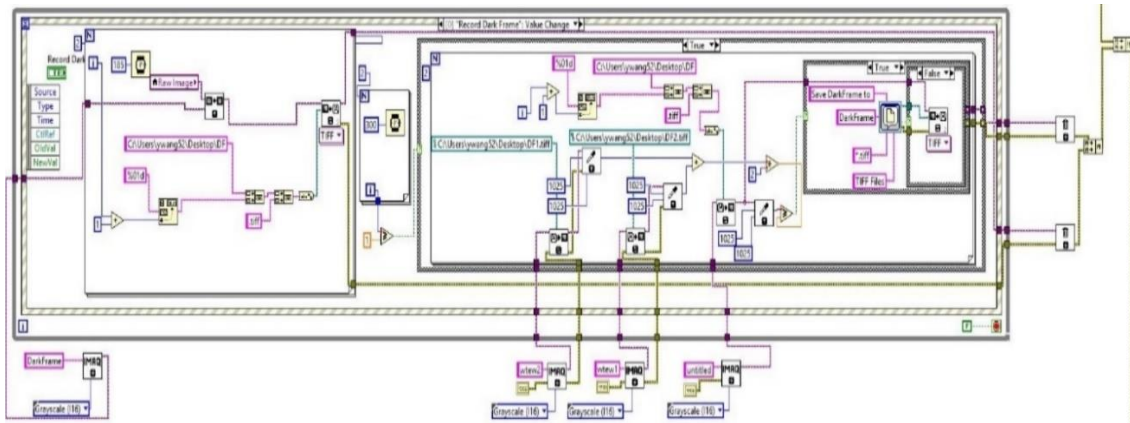
VSSDFS module feeds the sub-streams into the DKFA module. Without patient's eye in the system, the DKFA module records beamsplitter reflections (dark frames) for the data stream and the PSG intensity modulation stream, respectively. The recorded dark frames are then returned to the VSSDFS module, to be subtracted from the corresponding video streams. The DTFA module records data frames from retina and their corresponding PSG intensity modulation frames when user clicks the "Record Data Frame" button on the GUI, and automatically puts the recorded contents into a folder with user-specified name. The number of data frame & PSG intensity modulation frame pairs is also defined by users. Together, the three modules also determine the system's frame rate and data acquisition intervals.

The control program provides a GUI for the operator of the device, as can be seen in Figure. 6-2. There are three display windows on the GUI panel, the left window displays the raw video stream directly pulled out from the camera, which keeps blinking, the middle window and the right window display the separated data stream and intensity modulation stream, respectively, which are stable video streams that help the operator observing retinal features. The procedure of acquiring retinal data in clinical tests is as described below,

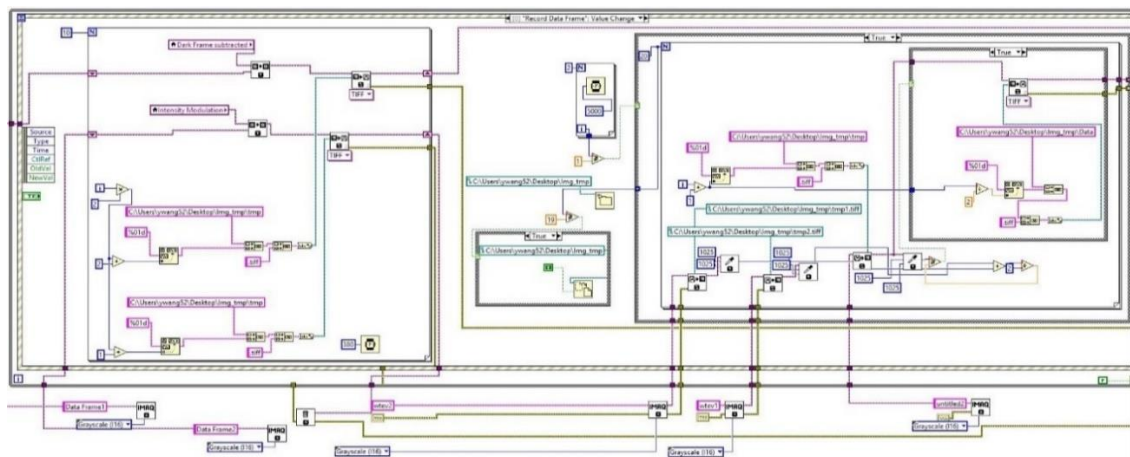
- Turn off the room light (to reduce ambient light noise)
- Turn on the LED illumination source of the device
- Switch on the rotational wheel, and set rotational speed to the correct value
- Connect the SRIMMP device and a windows laptop with an ethernet cable
- Open the SRIMMP control program on the laptop through LabVIEW
- Select "AVT Manta G419-B" in the "Choose Camera" dropdown list
- Click the "Record Dark Frame" button to record dark frames and save them to a designated location in the pop-up dialog windows



(a)



(b)



(c)

Figure 6-1. Sub-sections of the control system's LabVIEW block diagram. a) Video stream separation & dark frame subtraction. b) Dark frame acquisition. c) Data frame acquisition.

- Load the saved dark frames using the “Subtract DarkFrameInt” button and the “Subtract DarkFrame” button on the GUI panel
- Place patient’s eye in the correct position and tell the patient to look at the external target
- Find the region of interest (ROI) on the retina using the joystick controller of the translational stage
- Click the “Record Data Frame” button and save the data into a folder with user-specified name and location in the pop-up dialog windows

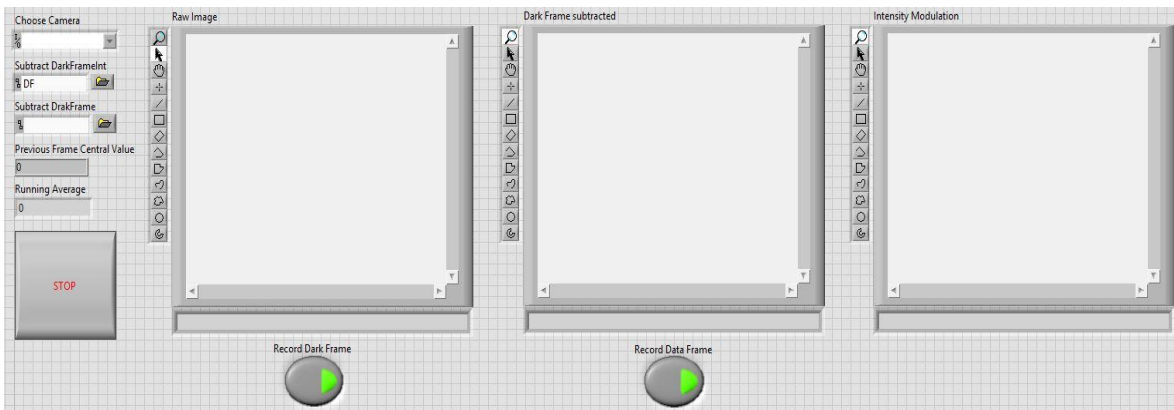


Figure. 6-2. The graphical user interface (GUI) of the control program of SRIMMP.

6.2 The first clinical test

The first set of clinical tests were carried out with two subjects, one with normal vision after contact lens correction, the other with -4D myopia. Subjects’ eyes had been dilated before the tests to reduce corneal reflection and increase signal throughput. The macular region on the retina was chosen to be the ROI, for some of its 2D Mueller matrix (MM) elements have a bow-tie pattern that can be easily identified [1]. Figure. 6-3 pictures a data frame and its corresponding PSG intensity modulation frame taken from the left eye of the subject with contact lenses. The macular region is labeled by a red circle on both frames. As can be seen, the contrast of polarization

fringes on the data frame is very low, which results in a weak signal that is vulnerable to random noises. Moreover, the fitting model of input Stokes parameters cannot work properly on this PSG intensity modulation frame due to its low contrast. As a result, the input Stokes parameters of the macular region were demodulated from an “empty polarimeter” frame with model eye taken before the clinical tests, fitted input Stokes parameters were not used in the 2D MM reconstruction.

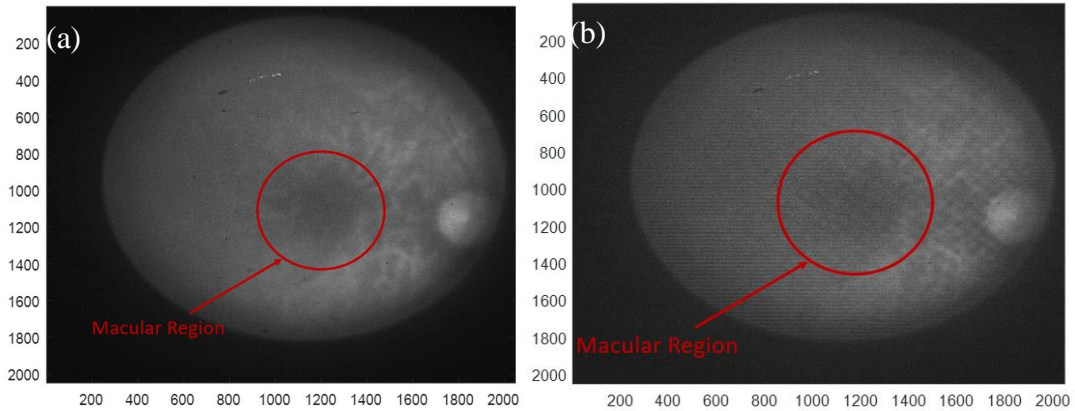


Figure. 6-3. a) Polarization modulation frame and b) intensity modulation frame taken from the retina of subject’s left eye.

The reconstructed 2D MM of the macular region on the above pictures is as depicted below in Figure. 6-4. Figure. 6-5 depicts the reconstruction result of the same region with a lower resolution, which corresponds to higher signal-to-noise (SNR) ratio. As can be seen, most of the MM elements have very small values, and the expected bow-tie structure cannot be distinguished from the background.

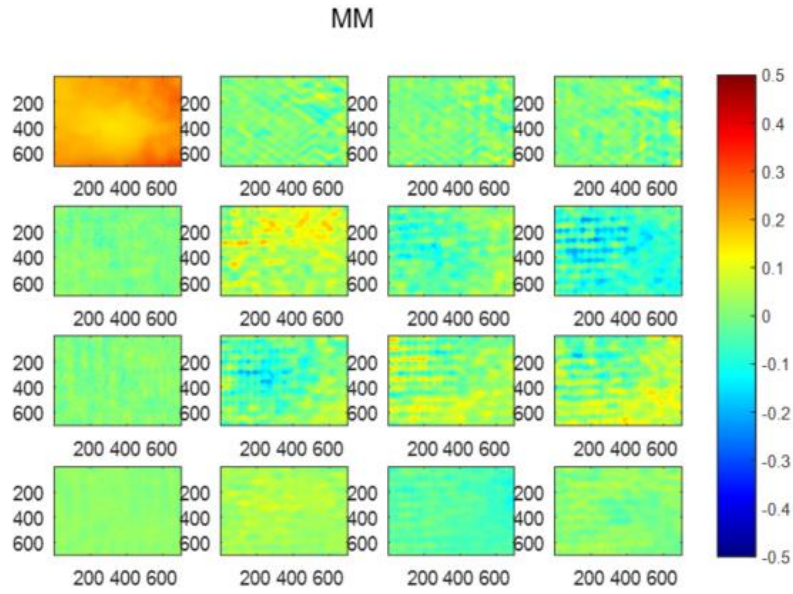


Figure. 6-4. The reconstructed 2D Mueller matrix of the macular region in Figure. 7-3.

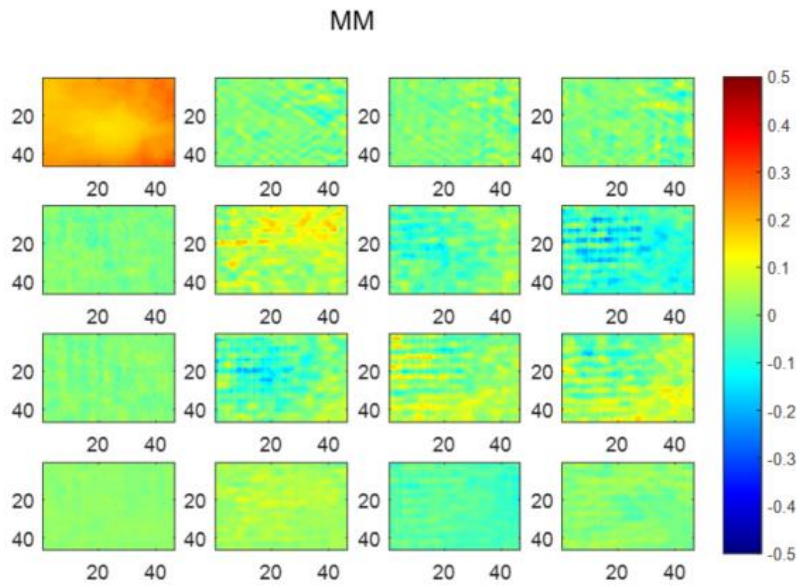


Figure. 6-5. The reconstructed Mueller matrix of macular region in Figure. 7-3. with lower resolution and better signal-to-noise (SNR) ratio.

The lack of contrast on the data images was mainly caused by defocus of PSA and PSG images, which is due to the lack of refocus mechanism in the SRIMMP system. In a traditional fundus camera design (external illumination or internal illumination), the re-focusing mechanism is simply realized by adding a zoom lens in the imaging pathway, to adapt to structural dimensions

of patients' eyes, which is difference from person to person. Unlike in the traditional designs, in the optical design of SRIMMP the PSG, the PSA, and patient's retina must be on conjugate planes when taking pictures, such that same extent of refocus must be applied to the illumination pathway and the imaging pathway simultaneously. To fulfill this requirement, the zoom lens in SRIMMP was planned to be placed between the beamsplitter and patient's eye, such that it is in both optical pathways. The addition of zoom lens would inevitably reduce the eye relief, to limit this negative effect we decided to use a set of interchangeable thin optometry lenses as zoom lenses. For each patient, a most appropriate optometry lens would be selected and placed into a lens-slot on the front side of the beamsplitter case for vision correction. An optometry lens set was purchased for this purpose and sent to a lens-coating vendor for anti-reflection coating. The coated lenses, however, showed much stronger surface reflection than had been expected, making it impossible to acquire useful retinal images with one of them in the optical path. The tests were forced to be carried out without zoom lenses, which resulted in defocused polarization fringes. The comparatively long wavelength of the illumination source could be another reason for the contrast loss, mainly in the background layer, a simple knife-edge experiment in the lab showed that red light cannot represent sharp features from human tissues as good as light with smaller wavelengths.

Apart from weak signal, the reconstructed 2D MM also suffers from a periodic error, which is likely caused by channel cross-talks in Fourier domain. To reduce the channel cross-talks, a Fourier domain background subtraction technique inspired by Craven' work was proposed [2]. To apply this technique, multiple data frames of a same retinal scene needs to be taken. In practice, a set of 10 data frames were taken to test the feasibility of this technique. The background subtraction technique assumes that, among the multiple data frames, the shift of polarization fringes is very small comparing to the shift of retinal background. Thus, the background could be separated and

subtracted from the data frames, which helps to mitigate the central burst's influence on spatial frequency channels in the Fourier domain. In the feasibility test, one data frame was chosen to be the target frame and the background shifts of the rest 9 frames were estimated by applying image registration technique. The estimated spatial shifts were then transformed into Fourier domain phase shifts. A 20×4 measurement matrix could be formed for each pixel in the Fourier domain channels using the phase shift information.

$$V = (R_p + R_b) + (I_p + I_b)i \quad (1)$$

As can be seen from Eq. 1, the value V at each pixel in the Fourier domain consists of a real part $R_p + R_b$ and an imaginary part $I_p + I_b$, in which b represents for background and p represents for polarization fringes. If the estimated Fourier domain phase shifts of polarization fringes and background are Δ_p and Δ_b , respectively, then

$$\begin{cases} I' = I_p \cos(\Delta_p) + R_p \sin(\Delta_p) + I_b \cos(\Delta_b) + R_b \sin(\Delta_b) \\ R' = R_p \cos(\Delta_p) - I_p \sin(\Delta_p) + R_b \cos(\Delta_b) - I_b \sin(\Delta_b) \end{cases} \quad (2)$$

where I' is the imaginary part after the phase shift, and R' is the real part after the phase shift. Combining the above equations for all the 10 data frames leads to a linear algebra equation with the 20×4 measurement matrix

$$\begin{bmatrix} \sin(\Delta_{p,1}) & \cos(\Delta_{p,1}) & \sin(\Delta_{b,1}) & \cos(\Delta_{b,1}) \\ \cos(\Delta_{p,1}) & -\sin(\Delta_{p,1}) & \cos(\Delta_{b,1}) & -\sin(\Delta_{b,1}) \\ \cdot & \cdot & \cdot & \cdot \\ \cdot & \cdot & \cdot & \cdot \\ \cdot & \cdot & \cdot & \cdot \\ \sin(\Delta_{p,10}) & \cos(\Delta_{p,10}) & \sin(\Delta_{b,10}) & \cos(\Delta_{b,10}) \\ \cos(\Delta_{p,10}) & -\sin(\Delta_{p,10}) & \cos(\Delta_{b,10}) & -\sin(\Delta_{b,10}) \end{bmatrix} * \begin{bmatrix} R_p \\ I_p \\ R_b \\ I_b \end{bmatrix} = \begin{bmatrix} I_1' \\ R_1' \\ I_2' \\ \cdot \\ \cdot \\ \cdot \\ I_{10}' \\ R_{10}' \end{bmatrix} \quad (3)$$

where the numbers in the subscripts represent different source images of the coefficients. Since Δ_{ps} are significantly smaller than Δ_{bs} , they could be approximated to 0. Replacing all the Δ_{ps} in Eq. 3 with 0s, we get

$$\begin{bmatrix} 0 & 1 & \sin(\Delta_{b,1}) & \cos(\Delta_{b,1}) \\ 1 & 0 & \cos(\Delta_{b,1}) & -\sin(\Delta_{b,1}) \\ \cdot & \cdot & \cdot & \cdot \\ \cdot & \cdot & \cdot & \cdot \\ \cdot & \cdot & \cdot & \cdot \\ 0 & 1 & \sin(\Delta_{b,10}) & \cos(\Delta_{b,10}) \\ 1 & 0 & \cos(\Delta_{b,10}) & -\sin(\Delta_{b,10}) \end{bmatrix} * \begin{bmatrix} R_p \\ I_p \\ R_b \\ I_b \end{bmatrix} = \begin{bmatrix} I_1' \\ R_1' \\ I_2' \\ \cdot \\ \cdot \\ \cdot \\ I_{10}' \\ R_{10}' \end{bmatrix} \quad (4)$$

the real and imaginary components from the background could then be solved by multiplying the pseudoinverse of the measurement matrix to the right-hand-side (RHS) of Eq. 4.

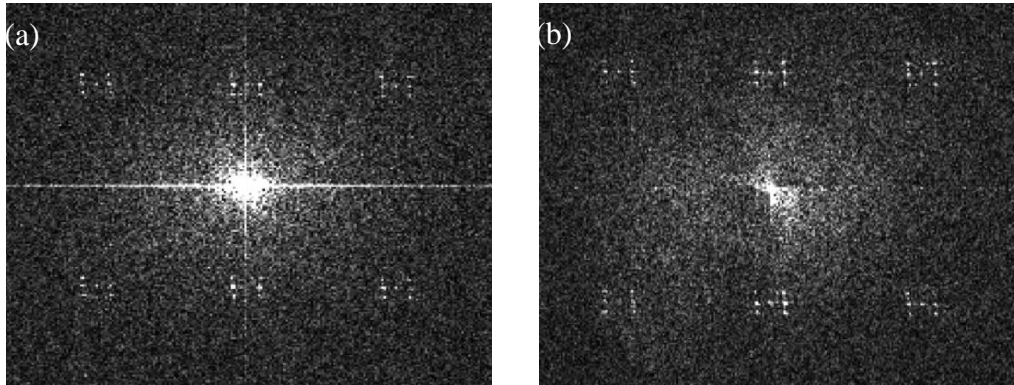


Figure. 6-6. The Fourier domain of a retinal data frame a) before and b) after the background subtraction. It can be seen from the pictures that the influence of the central burst decreases after applying our background subtraction technique.

The Fourier domain of a data frame before and after background subtraction are as depicted in Figure. 6-6(a) and Figure. 6-6(b). It can be seen from the pictures that, after the background subtraction the influence of central burst on higher frequency channels got reduced. The reconstructed 2D MM after applying the background subtraction technique is as depicted in Figure. 6-7, several elements of the 2D MM show more features when compared to their counterparts in

the original reconstruction. However, the symbolic bow-tie pattern was not observed from any of the MM elements, plus that the periodic errors remained on the 2D MM. This suggested that the influence of the channel cross-talk might not be the main reason for errors in 2D MM reconstruction.

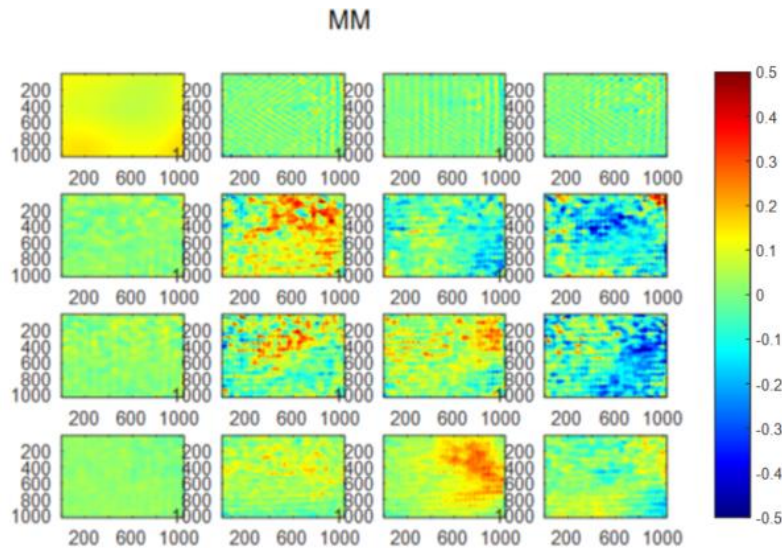


Figure. 6-7. The reconstructed 2D Muller matrix of the macular region from a retinal data frame after applying our background subtraction technique. More features appeared on the Mueller matrix elements, but no bow-tie pattern was observed.

6.3 The second clinical test

From the results of the first clinical test, it was determined that the defocus of polarization fringes was the biggest issue affecting 2D MM reconstruction. Without a re-focusing mechanism in the system, the only option to keep the polarization fringes in focus was to manually adjust the positions of the PSG and the PSA to fit a specific eye structure. The chosen eye for test was a left eye with -4D myopia. To place the PSA into the new position, two lenses were taken out of the imaging pathway, degraded performance of the imaging lens set and limited the focused polarization fringes to a smaller region on retina. Figure. 6-8 depicts the polarization fringes on the macular region of a data frame taken during the second clinical test, as can be seen, the polarization fringes have higher contrast when compared to those in the first clinical test. However,

the periodic contrast imbalance suggests that the polarization fringes were still not fully focused in the second clinical test, which was because the positions of the PSG and the PSA were already at physical limits and could not be further adjusted.

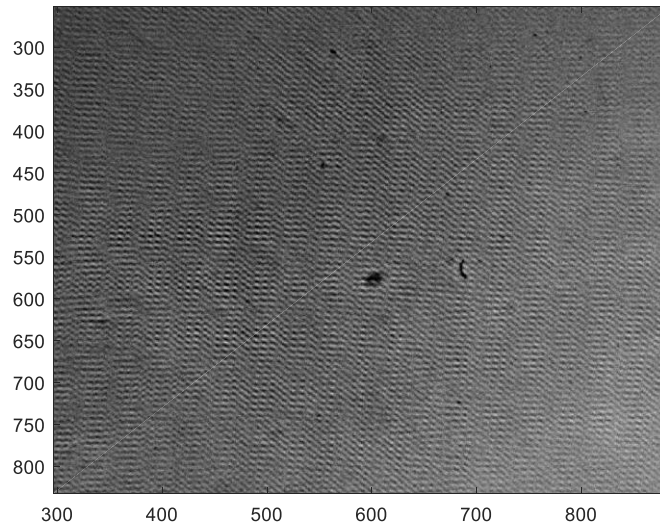


Figure. 6-8. A close-up view of polarization fringes on the macular region.

The 2D MM of the macular region was reconstructed with input Stokes parameters from the “empty polarimeter” frame and the fitting model, respectively. Figure. 6-9 depicts the reconstructed 2D MM of the macular region with input Stokes parameters from the “empty polarimeter” frame, while Figure. 6-10 represents the reconstructed MM of the same region with input Stokes parameters from the fitting model. As can be seen, in both cases the reconstructed 2D MM have similar patterns in some of the 16 elements. However, these stripe patterns seem to be caused by the defocus of polarization fringes, not by the optical properties of corresponding regions on the retina.

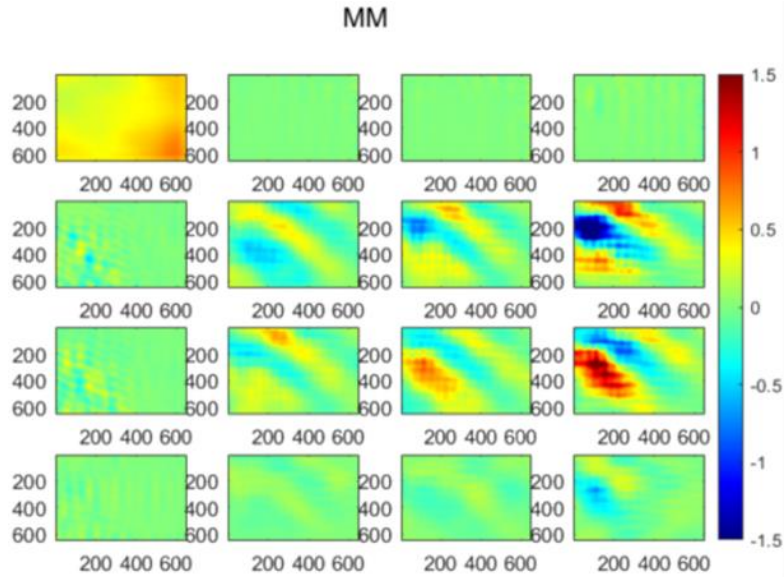


Figure. 6-9. The reconstructed 2D Mueller matrix of the macular region from a retinal data frame taken in the second clinical test. The input Stokes parameters were demodulated from an “empty polarimeter” frame with reference beam technique.

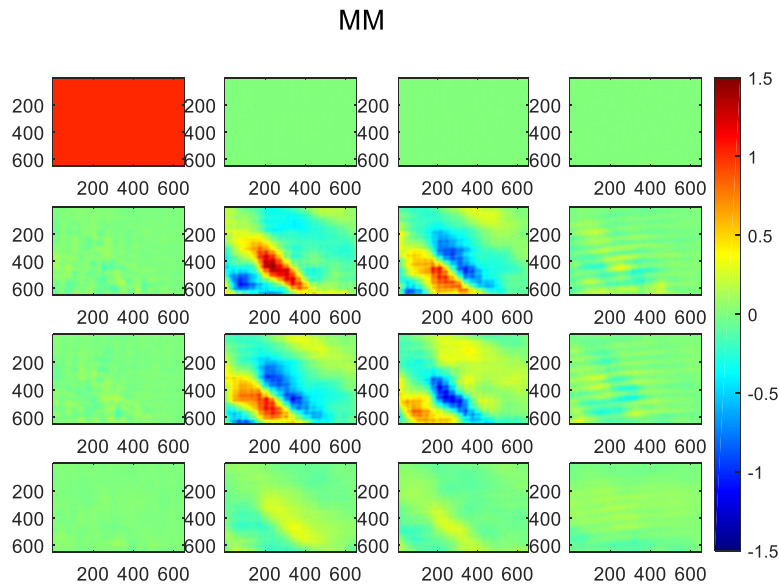


Figure. 6-10. The reconstructed 2D Mueller matrix of the macular region from a retinal data frame taken in the second clinical test. The input Stokes parameters were created by a fitting model according to the PSG intensity modulation frame taken along with the data frame.

Data frames were also taken with a 565 nm green LED source after a switch of illumination source, to see if images with higher contrast could be obtained under a shorter wavelength. The

picture in Figure. 6-11 was taken from the optic disc region of a subject's left eye. As can be seen, the details from the retinal background appear to be clearer than that of the red light retinal images. However, the polarization fringes still show a periodic contrast imbalance, which is an indication of defocus of the PSG and the PSA images.

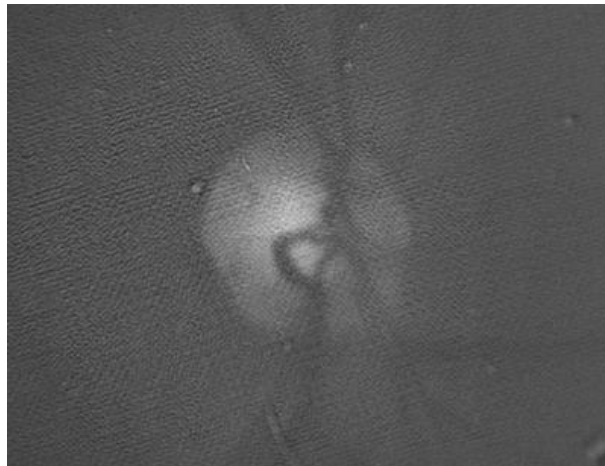


Figure. 6-11. A retinal image taken from the optic disc region of a subject's left eye, with 565 nm green LED as illumination source.

With the change of illumination wavelength, the number, locations and contents of the spatial frequency channels also changed. This is because the retardances of PGs and QWPs depend on the wavelength of incident light, while with 660 nm incident light their retardances equal to 180° and 45° , with 565 nm incident light they become 210° and 53° instead. The spatial channel locations in Fourier domain with 565 nm light are as shown in Figure. 6-12, non-conjugated channels are labeled. The expressions of spatial frequency channels in spatial domain are as illustrated in Eq. 5.

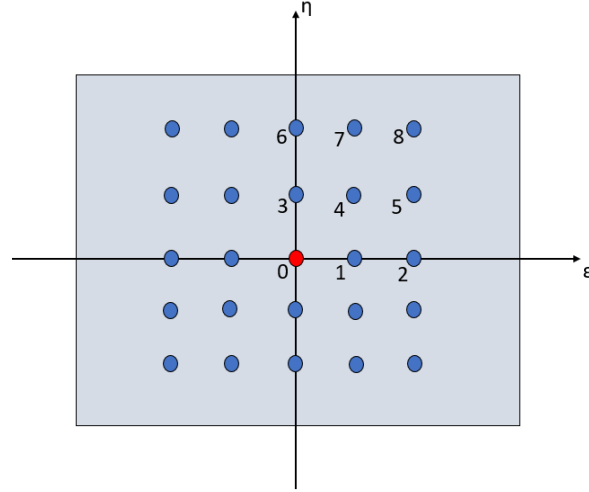


Figure. 6-12. Fourier domain spatial frequency channel distribution. ϵ and η are Fourier domain coordinates correspond to the spatial coordinates x and y , only non-conjugated channels are shown in the graph.

Comparing to the 660 nm illumination case, the number of non-conjugated channels increases from 3 to 9, the complexity of channel contents also increases.

$$\begin{cases}
 C_0 = 0.5S_0 + 0.0045S_1 + 0.048S_3 \\
 C_1 = \sin(2Ux)[0.005S_1 + 0.02S_3] + 0.048S_2 \cos(2Ux) \\
 C_2 = 0.024S_2 \sin(4Ux) + 0.0025S_1 \cos(4Ux) \\
 C_3 = \sin(2Uy)[0.51S_1 + 0.00956S_3] \\
 C_4 = 0.048S_2 \sin(2Ux + 2Uy) - \cos(2Ux + 2Uy)[0.048S_1 + 0.155S_3] \\
 C_5 = 0.1394S_1 \sin(4Ux + 2Uy) - 0.1394S_2 \cos(4Ux + 2Uy) \\
 C_6 = 0.062S_2 \sin(4Uy) + \cos(4Uy)[0.2551S_1 + 0.2788S_3] \\
 C_7 = \sin(2Ux + 4Uy)[0.1394S_1 + 0.0579S_3] + 0.1394S_3 \cos(2Ux + 4Uy) \\
 C_8 = 0.2519S_2 \sin(4Ux + 4Uy) - 0.1125S_1 \cos(4Ux + 4Uy)
 \end{cases} \quad (5)$$

Among the 9 spatial frequency channels shown above, C_0 was selected for S_0 demodulation, C_3 was selected for S_1 demodulation, C_8 was selected for S_2 demodulation, and C_7 was selected for S_3 demodulation. The influences brought by S_1 and S_2 components in C_0 are negligible since their coefficients are very small comparing to the S_0 coefficient. Figure. 6-13 depicts the reconstructed 2D MM of the macular region from a retinal data image taken with 565 nm illumination. The lack of meaningful features in the reconstruction is due to 1) the defocus in

polarization fringes and 2) the comparatively weak signal components in the frequency channels are vulnerable to errors and noises.

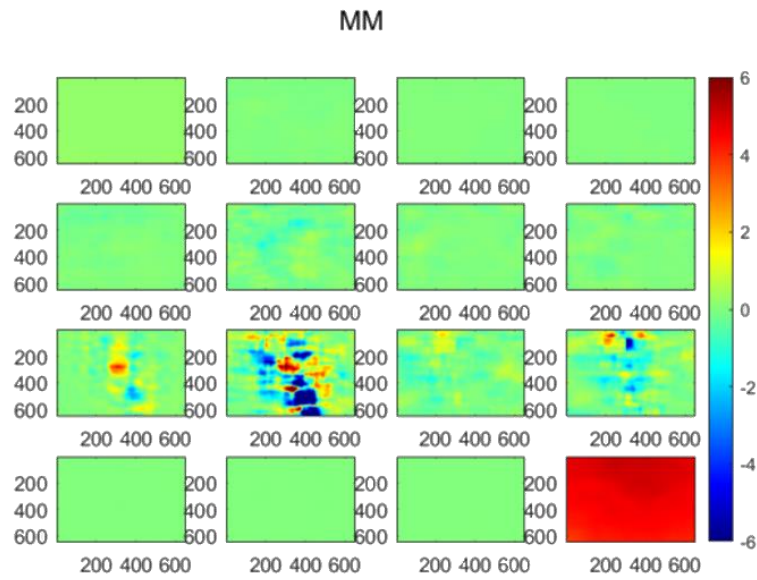


Figure. 6-13. The reconstructed 2D Mueller matrix of the macular region from a retinal data image taken with 565 nm illumination in the second clinical test.

References

- [1] Twietmeyer, K. M., Chipman, R. A., Elsner, A. E., Zhao, Y., & VanNasdale, D. (2008). Mueller matrix retinal imager with optimized polarization conditions. *Optics express*, *16*(26), 21339-21354.
- [2] Craven, J., & Kudenov, M. W. (2010). False signature reduction in channeled spectropolarimetry. *Optical Engineering*, *49*(5), 053602.

Chapter 8 Conclusion and Future Works

8.1 Conclusion

This dissertation discussed the work towards developing a snapshot retinal imaging Muller matrix (MM) polarimeter based on the channeled imaging polarimetry (CIP) technique, using spatial-spatial modulation created by polarization gratings (PGs). The achievements of this work include:

- Successfully built the first snapshot imaging MM polarimeter based on spatial-spatial modulation using PGs.
- Proposed a new system calibration/MM reconstruction approach combining reference beam technique and algebraic operations, solved the intrinsic problem exists in other MM reconstruction strategies and made accurate MM reconstruction possible.
- Successfully combined SMMP with a retinal camera design, such that the polarimeter can take snapshot polarization data from human retina.
- Explored different techniques to mitigate errors in MM reconstruction and increase reconstruction accuracy.

A new approach for system calibration and data reconstruction of the PG-based snapshot channeled retinal imaging MM polarimeter was proposed during this work. The feasibility of this approach was verified by a system simulation model created in Matlab. An optical design was created to combine the imaging snapshot MM polarimeter with an external illumination fundus camera, giving the system the ability to acquire data from human retina. The corresponding opto-mechanical design was also carried out to integrate the electronics and optics into a single functional device. Parts were purchased according to the optical design and the opto-mechanical

design, and the device was assembled in lab. A control program was coded in Labview to help the operation and data acquisition of the snapshot retinal imaging MM polarimeter device from a laptop connected to it. A user graphical user interface is provided by the control program. Lab tests with a model eye were conducted and showed promising results. Several different approaches of error reduction were proposed and tested. Clinical tests were conducted in the medical campus of USC with two subjects. 2D MMs were reconstructed for the macular region of retina. The reasons for reconstruction errors were discussed, and several methods were proposed to lessen the errors.

8.2 Suggestions for future works

To obtain retinal images with better focus in clinical tests, a proper refocus mechanism must be incorporated into the snapshot retinal imaging MM polarimeter to adapt the device to dimensional differences of eyes from different patients. This could be done by either inserting a thin zoom lens between patient's eye and the beamsplitter or adding one set of zoom lenses to each of the two optical pathways. The former approach was tried in this work; however, it was failed because the anti-reflection coatings on the zoom lenses were not good enough. Better anti-reflection coatings must be applied to the zoom lenses for this approach to work as expected. To implement the latter approach, major modifications to the optical design and opto-mechanical design must be carried out. Moreover, when taking retinal images, the two zoom lens sets have to be simultaneously adjusted to apply same amount of changes to the illumination pathway and the imaging pathway, which imposes additional requirements for the control program of the system. In terms of error reduction, a new algorithm that involves some extent of non-linear process might be able to further reduce the existing errors in current MM reconstruction. It would also be helpful to increase the robustness of the input Stokes parameters fitting model on distorted or low-contrast PSG intensity modulation frames.

APPENDICES

Appendix A – Derivation of Stokes parameters

The following derivation is summarized from D. H. Goldstein's polarized light (third edition, CRC Press, 2011). Assuming the propagation direction is z , a monochromatic transverse wave could be represented by its x and y components as

$$\begin{cases} E_x(t) = E_{0x} \cos[wt + \delta_x] \\ E_y(t) = E_{0y} \cos[wt + \delta_y] \end{cases} \quad (1)$$

where E_{0x} and E_{0y} are amplitudes in x and y directions, respectively. w represents the angular frequency, δ_x and δ_y denote phase factors [19]. Removing the wt term from Eq. 1 gives

$$\frac{E_x^2(t)}{E_{0x}^2} + \frac{E_y^2(t)}{E_{0y}^2} - \frac{2E_x(t)E_y(t)}{E_{0x}E_{0y}} \cos \delta = \sin^2 \delta, \quad (2)$$

where $\delta = \delta_x - \delta_y$. Eq. 2 represents the relationship between the two wave components at a specific time of observation. The time-dependent terms in Eq. 2 can be replaced by corresponding time-averaged terms (over one period of oscillation) to obtain the equation below

$$\frac{\langle E_x^2(t) \rangle}{E_{0x}^2} + \frac{\langle E_y^2(t) \rangle}{E_{0y}^2} - \frac{2\langle E_x(t)E_y(t) \rangle}{E_{0x}E_{0y}} \cos \delta = \sin^2 \delta, \quad (3)$$

where $\langle \dots \rangle$ represents the operation of time averaging. The expressions of the averaged values in Eq. 3 are

$$\langle E_x^2(t) \rangle = \frac{1}{2} E_{0x}^2, \quad (4)$$

$$\langle E_y^2(t) \rangle = \frac{1}{2} E_{0y}^2, \quad (5)$$

$$\langle E_x(t)E_y(t) \rangle = \frac{1}{2} E_{0x}E_{0y} \cos \delta, \quad (6)$$

thus, Eq. 3 can be re-written in the form of

$$1 - \cos^2 \delta = \sin^2 \delta, \quad (7)$$

multiplying $4E_{0x}^2E_{0y}^2$ to both sides of Eq. 7 yields

$$4E_{0x}^2E_{0y}^2 - 4E_{0x}^2E_{0y}^2 \cos^2 \delta = 4E_{0x}^2E_{0y}^2 \sin^2 \delta, \quad (8)$$

rearranging the terms in Eq. 9 gets us

$$(E_{0x}^2 + E_{0y}^2)^2 - (E_{0x}^2 - E_{0y}^2)^2 - (2E_{0x}E_{0y} \cos \delta)^2 = (2E_{0x}E_{0y} \sin \delta)^2, \quad (9)$$

the four Stokes parameters are defined as the terms inside the brackets in Eq. 9

$$S_0 = E_{0x}^2 + E_{0y}^2, \quad (10)$$

$$S_1 = E_{0x}^2 - E_{0y}^2, \quad (11)$$

$$S_2 = 2E_{0x}E_{0y} \cos \delta, \quad (12)$$

$$S_3 = 2E_{0x}E_{0y} \sin \delta. \quad (13)$$

From the above derivations, it can be seen that for fully polarized light, an intrinsic relationship among Stokes parameters is

$$S_0^2 = S_1^2 + S_2^2 + S_3^2, \quad (14)$$

for partially polarized light, this relationship becomes

$$S_0^2 > S_1^2 + S_2^2 + S_3^2. \quad (15)$$

The degree of polarization (DOP) of light is defined with Stokes parameters as

$$DOP = \frac{\sqrt{S_1^2 + S_2^2 + S_3^2}}{S_0}. \quad (16)$$

Appendix B – Matlab simulation model of calibration and Mueller matrix reconstruction

a) The main script

```
%set PG frequency and Fourier domain axes
a = 0.3;
b = 6*a;
k = 2*pi;
x = meshgrid(-5:1/20:5-1/20);
y = meshgrid(-5:1/20:5-1/20)';
[Lx,Ly] = size(x);

[Iref1,Iref2,Am] = cal_gen(0); %generate reference data for
reference beam calibration

%create Fourier domain filters for channel isolation
filterout = zeros(Lx,Ly,3);
w =18;
filtervar = zeros(Lx,Ly);
filtervar = filtervar+
(hamming_filter(101,101,w,Lx,Ly,0,1)).^(1/1);

for i = 1:200
    for j = 1:200
        if (filtervar(i,j)~=0)
            filtervar(i,j) = 1;
        end
    end
end
filterout(:,:,3) = filtervar;

filtervar = zeros(Lx,Ly);
filtervar =
filtervar+(hamming_filter(29,173,w,Lx,Ly,0,1)).^(1/1);

for i = 1:200
    for j = 1:200
        if (filtervar(i,j)~=0)
            filtervar(i,j) = 1;
        end
    end
end
filterout(:,:,1) = filtervar;

filtervar = zeros(Lx,Ly);
filtervar =
filtervar+(hamming_filter(29,101,w,Lx,Ly,0,1)).^(1/1);
```

```

for i = 1:200
    for j = 1:200
        if (filtervar(i,j)~=0)
            filtervar(i,j) = 1;
        end
    end
end
filterout(:,:,2) = filtervar;
filter = filterout;

ref0 =
ifft2(ifftshift(fftshift(fft2(Iref1)).*squeeze(filter(:,:,3))));
ref1 =
ifft2(ifftshift(fftshift(fft2(Iref1)).*squeeze(filter(:,:,1))));
ref1 = ref1./ref0; %normalize reference to S0 component
ref2 =
ifft2(ifftshift(fftshift(fft2(Iref2)).*squeeze(filter(:,:,2))));
ref2 = ref2./ref0;

%prepare sample data for PSA calibration
theta = 0:10:180;
imgdataLP = zeros(200,200,length(theta));
C1L = imgdataLP;
C2L = imgdataLP;
C1_0L = imgdataLP;
S0_L = imgdataLP;
S1_L = imgdataLP;
S2_L = imgdataLP;
S3_L = imgdataLP;

%linear polarization set
for n=1:length(theta)
    [q1,q2] = cal_gen(theta(n));
    %channel 1 (linear)
    sample1 =
ifft2(ifftshift(fftshift(fft2(q1)).*squeeze(filter(:,:,1))));
    sample1 = sample1./ref1;
    C1L(:,:,n) = sample1;
    %channel 2 (circular)
    sample1 =
ifft2(ifftshift(fftshift(fft2(q1)).*squeeze(filter(:,:,2))));
    sample1 = sample1./ref2;
    C2L(:,:,n) = sample1;
    %channel 0 (magnitude)
    sample1 =
ifft2(ifftshift(fftshift(fft2(q1)).*squeeze(filter(:,:,3))));

```

```

C1_0L(:, :, n) = abs(sample1);

S0_L(:, :, n) = abs(C1_0L(:, :, n));
S1_L(:, :, n) = real(C1L(:, :, n));
S2_L(:, :, n) = -imag(C1L(:, :, n));
S3_L(:, :, n) = real(C2L(:, :, n));
end

imgdataQWP = zeros(200, 200, length(theta));
C1C = imgdataQWP;
C2C = imgdataQWP;
C2_0C = imgdataQWP;
S0_C = imgdataQWP;
S1_C = imgdataQWP;
S2_C = imgdataQWP;
S3_C = imgdataQWP;

ref0 =
ifft2(ifftshift(fftshift(fft2(Iref2)).*squeeze(filter(:, :, 3))));
ref2 =
ifft2(ifftshift(fftshift(fft2(Iref2)).*squeeze(filter(:, :, 2))));
ref2 = ref2./ref0; %normalize reference to S0 component

%circular polarization set
for n=1:length(theta)
    [q1, q2] = cal_gen(theta(n));
    %channel 1 (linear)
    sample1 =
ifft2(ifftshift(fftshift(fft2(q2)).*squeeze(filter(:, :, 1))));
    sample1 = sample1./ref1;
    C1C(:, :, n) = sample1;
    %channel 2 (circular)
    sample1 =
ifft2(ifftshift(fftshift(fft2(q2)).*squeeze(filter(:, :, 2))));
    sample1 = sample1./ref2;
    C2C(:, :, n) = sample1;
    %channel 0 (magnitude)
    sample1 =
ifft2(ifftshift(fftshift(fft2(q2)).*squeeze(filter(:, :, 3))));
    C2_0C(:, :, n) = abs(sample1);

    S0_C(:, :, n) = abs(C2_0C(:, :, n));
    S1_C(:, :, n) = real(C1C(:, :, n));
    S2_C(:, :, n) = -imag(C1C(:, :, n));
    S3_C(:, :, n) = real(C2C(:, :, n));
end

```

```

Sreal = zeros(2*length(theta),4);
Smeas = Sreal;
W = zeros(Lx,Ly,4,4);

%precalculate the 'real' Stokes parameters for PSA calibration
indx = 0;
for gg=1:length(theta)
    indx = indx+1;
    Mv(indx, :, :) = lp(theta(gg));
end
for gg=1:length(theta)
    indx = indx+1;
    Mv(indx, :, :) = qwp(45)*lp(theta(gg));
end

%calculate correction matrix W for each pixel, it will be used
to map the response of PSA to an 'ideal' channeled Stokes
polarimeter
for n=1:Lx
    n
    for m=1:Ly
        indx = 0;
        for gg=1:length(theta)
            indx = indx+1;
            Sreal(indx, :) =
(squeeze(Mv(indx, :, :)) * [2*S0_L(n,m,gg); 0; 0; 0])';
            Smeas(indx, :) =
[S0_L(n,m,gg); S1_L(n,m,gg); S2_L(n,m,gg); S3_L(n,m,gg)]';
        end

        for gg=1:length(theta)
            indx = indx+1;
            Sreal(indx, :) =
(squeeze(Mv(indx, :, :)) * [2*S0_C(n,m,gg); 0; 0; 0])';
            Smeas(indx, :) =
[S0_C(n,m,gg); S1_C(n,m,gg); S2_C(n,m,gg); S3_C(n,m,gg)]';
        end

        Sm = Smeas';
        Sr = Sreal';
        A = pinv(Sm);
        W(n,m, :, :) = Sr*A;
    end
end

%%

```

```

%construct empty polarimeter data
Iemp = zeros(200,200,4);

for n=1:Lx
    for m=1:Ly
        S =
gen_retarder(k*a*180/pi*y(n,m),180)*gen_retarder(45,90)*gen_reta
rder(k*a*x(n,m)*180/pi,180)*lp(0)*[1;0;0;0];
        Semp = squeeze(Am(n,m,:,:))*eye(4,4)*S;
        Iemp(n,m,1) = Semp(1);
        Iemp(n,m,2) = Semp(2);
        Iemp(n,m,3) = Semp(3);
        Iemp(n,m,4) = Semp(4);
    end
end

Iemp = Iemp(:,:,1);

%channel 1 (linear)
sample1 =
ifft2(ifftshift(fftshift(fft2(Iemp(:,:,1))).*squeeze(filter(:,:
1)))));
sample1 = sample1./ref1;
C1E = sample1;
%channel 2 (circular)
sample1 =
ifft2(ifftshift(fftshift(fft2(Iemp(:,:,1))).*squeeze(filter(:,:
2)))));
sample1 = sample1./ref2;
C2E = sample1;
%channel 0 (magnitude)
sample1 =
ifft2(ifftshift(fftshift(fft2(Iemp(:,:,1))).*squeeze(filter(:,:
3)))));
C1_0E = abs(sample1);

S0_E = abs(C1_0E);
S1_E = real(C1E);
S2_E = -imag(C1E);
S3_E = real(C2E);

%Reconstructing Mueller Matrix
S_Empty = zeros(Lx,Ly,4);
S_Empty_b = zeros(Lx,Ly,4);
S_Empty_o = zeros(Lx,Ly,4);
for n=1:Lx %1:Lx

```

```

n
for m=1:Ly% %1:Ly
    Wt = squeeze(W(n,m, :, :));
    S_Empty(n,m, :) =
Wt*[S0_E(n,m);S1_E(n,m);S2_E(n,m);S3_E(n,m)];
    S_Empty_b(n,m, :) =
[S0_E(n,m);S1_E(n,m);S2_E(n,m);S3_E(n,m)];
end
end

%Sample data generaton
Isamp = zeros(200,200,4);
Mtest = zeros(200,200,4,4);

%create a Mueller matrix sampe, a low spatial frequency has been
added
for n = 1:Lx
    for m = 1:Ly
Mtest(n,m, :, :) = eye(4,4);
    end
end

for n = 51:150
    for m = 85:115
Mtest(n,m, :, :) = gen_retarder(25,180);
    end
end

for n = 85:115
    for m = 51:150
Mtest(n,m, :, :) = gen_retarder(25,180);
    end
end

for n=1:Lx
    for m=1:Ly
        S =
gen_retarder(k*a*180/pi*y(n,m),180)*gen_retarder(45,90)*gen_reta
rder(k*a*x(n,m)*180/pi,180)*lp(0)*[1;0;0;0];
        Ssamp = squeeze(Am(n,m, :, :))*squeeze(Mtest(n,m, :, :))*S;
        Isamp(n,m,1) = Ssamp(1);
        Isamp(n,m,2) = Ssamp(2);
        Isamp(n,m,3) = Ssamp(3);
        Isamp(n,m,4) = Ssamp(4);
    end
end
Isamp = Isamp(:, :, 1);

```

```

%channel 1 (linear)
sample1 =
ifft2(ifftshift(fftshift(fft2(Isamp)).*squeeze(filter(:,:,1))));
sample1 = sample1./ref1;
C1S = sample1;
%channel 2 (circular)
sample1 =
ifft2(ifftshift(fftshift(fft2(Isamp)).*squeeze(filter(:,:,2))));
sample1 = sample1./ref2;
C2S = sample1;
%channel 0 (magnitude)
sample1 =
ifft2(ifftshift(fftshift(fft2(Isamp)).*squeeze(filter(:,:,3))));
C1_0S = abs(sample1);

S0_S = abs(C1_0S);
S1_S = real(C1S);
S2_S = -imag(C1S);
S3_S = real(C2S);

%correct calibration parameters
S_Sample = zeros(Lx,Ly,4);
S_Sample_b = zeros(Lx,Ly,4);
for n=1:Lx %1:Lx
    n
    for m=1:Ly% %1:Ly
        Wt = squeeze(W(n,m,:,:));
        S_Sample(n,m,:) =
Wt*[S0_S(n,m);S1_S(n,m);S2_S(n,m);S3_S(n,m)];
        S_Sample_b(n,m,:) =
[S0_S(n,m);S1_S(n,m);S2_S(n,m);S3_S(n,m)];
    end
end

%%
%calculate Mueller matrix

w2 = 17; %width of the window over which to calculate the
Mueller matrix elements
abserror = 0;
Mout = zeros(Lx-w2+1,Ly-w2+1,4,4);

for n=1:Lx-16
    n
    for m=1:Ly-16
        xpix = meshgrid(n:n+w2-1);

```

```

xpix = reshape(xpix,[1,w2^2]);
ypix = meshgrid(m:m+w2-1)';
ypix = reshape(ypix,[1,w2^2]);
ind = sub2ind([Lx,Ly],xpix,ypix);

%solve for first row of sample Mueller matrix. Extract
the S0
%component.
Sv = squeeze(S_Sample(:,:,1));
S0mat_out = squeeze(Sv(ind));
Sv = squeeze(S_Sample(:,:,2));
S1mat_out = squeeze(Sv(ind));
Sv = squeeze(S_Sample(:,:,3));
S2mat_out = squeeze(Sv(ind));
Sv = squeeze(S_Sample(:,:,4));
S3mat_out = squeeze(Sv(ind));

Sv = squeeze(S_Empty(:,:,1));
S0mat_in = squeeze(Sv(ind))';
Sv = squeeze(S_Empty(:,:,2));
S1mat_in = squeeze(Sv(ind))';
Sv = squeeze(S_Empty(:,:,3));
S2mat_in = squeeze(Sv(ind))';
Sv = squeeze(S_Empty(:,:,4));
S3mat_in = squeeze(Sv(ind))';

%create measurement matrix
Ws = [S0mat_in,S1mat_in,S2mat_in,S3mat_in];

M1 = pinv(Ws)*S0mat_out';
M2 = pinv(Ws)*S1mat_out';
M3 = pinv(Ws)*S2mat_out';
M4 = pinv(Ws)*S3mat_out';
M = [M1';M2';M3';M4'];
Mout(n,m,,:) = M;
%M = M./M1(1)
abserror = abserror+sum(sum(abs(squeeze(Mtest(n,m,,:))-
M))); %evaluate the error in Mueller matrix reconstruction

end
end
aae = abserror/467856;

t = 0;
figure(2)
for n = 1:4
for m = 1:4

```

```

t = t+1;
subplot(4,4,t);
imagesc(squeeze(Mout(:, :, n, m)));
caxis([-1 1])
colormap(jet(256))
end
end
suptitle('Reconstructed Mueller matrices');
h = colorbar;
set(h, 'Position', [.9214 .107 .0301 .750]);

```

b) Sub-functions

```

function [result1,result2,result3] = cal_gen(theta)
%To generate calibration sample data fot the SMMP simulator
k = 2*pi;
a = 0.3;
b = 6*a;
ref1s = zeros(200,200,4);
ref2s = zeros(200,200,4);
x = meshgrid(-5:1/20:5-1/20);
y = meshgrid(-5:1/20:5-1/20)';
[Lx,Ly] = size(x);
Am = zeros(Lx,Ly,4,4);

for n=1:Lx
    for m=1:Ly
        A =
lp(0)*gen_retarder(k*b*(y(n,m))*180/pi,180)*gen_retarder(45,90)*
gen_retarder(k*b*(x(n,m))*180/pi,180);
        Am(n,m, :, :) = A;
        Sref1 = A*lp(theta)*[1;0;0;0];
        Sref2 = A*qwp(45)*lp(theta)*[1;0;0;0];
        ref1s(n,m,1) = Sref1(1);
        ref1s(n,m,2) = Sref1(2);
        ref1s(n,m,3) = Sref1(3);
        ref1s(n,m,4) = Sref1(4);
        ref2s(n,m,1) = Sref2(1);
        ref2s(n,m,2) = Sref2(2);
        ref2s(n,m,3) = Sref2(3);
        ref2s(n,m,4) = Sref2(4);
    end
end

Iref1 = ref1s(:, :, 1);
Iref2 = ref2s(:, :, 1);

```

```

result1 = Iref1;
result2 = Iref2;
result3 = Am;

function [result1,result2] = cal_gen_s(theta,Am)

ref1s = zeros(200,200,4);
ref2s = zeros(200,200,4);
x = meshgrid(-5:1/20:5-1/20);
[Lx,Ly] = size(x);

for n=1:Lx
    for m=1:Ly
        Sref1 = squeeze(Am(n,m,:,:))*lp(theta)*[1;0;0;0];
        Sref2 = squeeze(Am(n,m,:,:))*qwp(45)*lp(theta)*[1;0;0;0];
        ref1s(n,m,1) = Sref1(1);
        ref1s(n,m,2) = Sref1(2);
        ref1s(n,m,3) = Sref1(3);
        ref1s(n,m,4) = Sref1(4);
        ref2s(n,m,1) = Sref2(1);
        ref2s(n,m,2) = Sref2(2);
        ref2s(n,m,3) = Sref2(3);
        ref2s(n,m,4) = Sref2(4);
    end
end

Iref1 = ref1s(:,:,1);
Iref2 = ref2s(:,:,1);
result1 = Iref1;
result2 = Iref2;

```

Appendix C – Matlab code used to generate correction matrices from calibration data

```
path = 'C:\Users\user1\Documents\Matlab\Matlab
Simulator\calibrationsamplefolder\';

% Select the ROI, and always center the data frame at a same
point
mask = zeros(2048,2048);
rc = 1024;
cc = 1024;

for m = 1:2048;
    for n = 1:2048;
        if sqrt((n-rc)^2+(m-cc)^2) <= 1000;
            mask(n,m) = 1;
        end
    end
end

r = rc-375:rc+374;
c = rc-375:rc+374;

REF1 = double(imread([path,'lp0','.tiff']));
REF1 = REF1.*mask;
REF1 = REF1(r,c);
DF = double(imread([path,'df','.tiff']));
DF = DF.*mask;
DF = DF(r,c);
REF2 = double(imread([path,'lp0q45','.tiff']));
REF2 = REF2.*mask;
REF2 = REF2(r,c);
FLT = double(imread([path,'flat','.tiff']));
FLT = FLT.*mask;
FLT = FLT(r,c);

filter1 = zeros(750,750);
filter2 = zeros(750,750);
filter3 = zeros(750,750);

filter1 =
filter1+(hamming_filter(376,376,20,750,750,0,1)).^(1/1);
filter2 =
filter2+(hamming_filter(275,478,20,750,750,0,1)).^(1/1);
filter3 =
filter3+(hamming_filter(274,376,20,750,750,0,1)).^(1/1);
```

```

C0_r1 = ifft2(ifftshift(fftshift(fft2((REF1-
DF)./FLT)).*filter1));
C1_r1 = ifft2(ifftshift(fftshift(fft2((REF1-
DF)./FLT)).*filter2));
C2_r1 = ifft2(ifftshift(fftshift(fft2((REF1-
DF)./FLT)).*filter3));

C0_r2 = ifft2(ifftshift(fftshift(fft2((REF2-
DF)./FLT)).*filter1));
C1_r2 = ifft2(ifftshift(fftshift(fft2((REF2-
DF)./FLT)).*filter2));
C2_r2 = ifft2(ifftshift(fftshift(fft2((REF2-
DF)./FLT)).*filter3));

% PSA calibration

Smeas = zeros(750,750,38,4);
Snom = zeros(750,750,38,4);
We2c = zeros(750,750,4,4);

for n = 1:19
    a = sprintf('%d', (n-1)*10);
    sam = double(imread([path, 'lp', a, '.tiff']));
    sam = sam(r,c);
    sam = abs(sam);%-scattercal1);
    C0_s = ifft2(ifftshift(fftshift(fft2((sam-
DF)./FLT)).*filter1));
    C1_s = ifft2(ifftshift(fftshift(fft2((sam-
DF)./FLT)).*filter2));
    C2_s = ifft2(ifftshift(fftshift(fft2((sam-
DF)./FLT)).*filter3));
    s0 = abs(C0_s)./abs(C0_s);
    s1 = real((C0_r1./C0_s).*(C1_s./C1_r1));
    s2 = imag((C0_r1./C0_s).*(C1_s./C1_r1));
    s3 = real((C0_r2./C0_s).*(C2_s./C2_r2));
    Smeas(:, :, n, 1) = s0;
    Smeas(:, :, n, 2) = s1;
    Smeas(:, :, n, 3) = s2;
    Smeas(:, :, n, 4) = s3;
end
%
for n = 1:19
    a = sprintf('%d', (n-1)*10);
    sam = double(imread([path, 'lp', a, 'q45.tiff']));
    sam = sam(r,c);
    sam = abs(sam);%-scattercal2);

```

```

    C0_s = ifft2(ifftshift(fftshift(fft2((sam-
DF) ./FLT)).*filter1));
    C1_s = ifft2(ifftshift(fftshift(fft2((sam-
DF) ./FLT)).*filter2));
    C2_s = ifft2(ifftshift(fftshift(fft2((sam-
DF) ./FLT)).*filter3));
    s0 = abs(C0_s) ./ abs(C0_s);
    s1 = real((C0_r1 ./ C0_s) .* (C1_s ./ C1_r1));
    s2 = imag((C0_r1 ./ C0_s) .* (C1_s ./ C1_r1));
    s3 = real((C0_r2 ./ C0_s) .* (C2_s ./ C2_r2));
    Smeas(:, :, n+19, 1) = s0;
    Smeas(:, :, n+19, 2) = s1;
    Smeas(:, :, n+19, 3) = s2;
    Smeas(:, :, n+19, 4) = s3;
end

for n = 1:19;
    tmp2 = 2*gen_retarder(45,90)*lp((n-1)*10)*[1;0;0;0];
    tmp1 = 2*lp((n-1)*10)*[1;0;0;0];
    Snom(:, :, n, 1) = tmp1(1);
    Snom(:, :, n, 2) = tmp1(2);
    Snom(:, :, n, 3) = tmp1(3);
    Snom(:, :, n, 4) = tmp1(4);
    Snom(:, :, n+19, 1) = tmp2(1);
    Snom(:, :, n+19, 2) = tmp2(2);
    Snom(:, :, n+19, 3) = tmp2(3);
    Snom(:, :, n+19, 4) = tmp2(4);
end

for i = 1:750;
    for j = 1:750;
        A = pinv(squeeze(Snom(i, j, 1:38, :)));
        Sm0 = squeeze(Smeas(i, j, 1:38, 1));
        Sm1 = squeeze(Smeas(i, j, 1:38, 2));
        Sm2 = squeeze(Smeas(i, j, 1:38, 3));
        Sm3 = squeeze(Smeas(i, j, 1:38, 4));
        W1 = (A*Sm0)';
        W2 = (A*Sm1)';
        W3 = (A*Sm2)';
        W4 = (A*Sm3)';
        We2c(i, j, :, :) = [W1;W2;W3;W4];
    end
end

% Evaluate the calibration result
Sself = zeros(38,4);

```

```

pnum = 201;
for n = 1:38;
    Sself(n,:) = pinv(squeeze(mean(mean((We2c(pnum-
5:pnum+5,pnum-5:pnum+5,:,:)))) * squeeze(mean(mean((Smeas(pnum-
5:pnum+5,pnum-5:pnum+5,n,:))))) );
end
figure(1)
plot(1:38,squeeze(mean(mean((Snom(pnum-5:pnum+5,pnum-
5:pnum+5,:,1))))),1:38,Sself(:,1),1:38,squeeze(mean(mean((Snom(p
num-5:pnum+5,pnum-
5:pnum+5,:,2))))),1:38,Sself(:,2),1:38,squeeze(mean(mean((Snom(p
num-5:pnum+5,pnum-
5:pnum+5,:,3))))),1:38,Sself(:,3),1:38,squeeze(mean(mean((Snom(p
num-5:pnum+5,pnum-5:pnum+5,:,4))))),1:38,Sself(:,4));
legend('nominal S0','corrected S0','nominal S1','corrected
S1','nominal S2','corrected S2','nominal S3','corrected S3');

```